Nanostructure Control and Photochemistry in Inorganic Nano-sheet Materials

March, 2015

FUJIMURA, Takuya

Preface

The studies presented in this thesis were carried out under the guidance of Professor Shinsuke Takagi at Department of Applied Chemistry, Graduate Course of Urban Environmental Sciences, Tokyo Metropolitan University.

Takuya FUJIMURA

Department of Applied Chemistry

Graduate Course of Urban Environmental Sciences

Tokyo Metropolitan University

1-1 Minami-ohsawa, Hachiohji

Tokyo 192-0364, JAPAN

Contents

Chapter 1

General Introduction

1.1. Photosynthesis[1-4]

Energy issue is one of the big problems which human beings have to solve. Lots of countries depend on the fossil fuels as main energy source, however fossil fuels are limited resources, thus the development of the alternative energy resources is crucial important question. To solve this problem, solar energy, geothermal energy, wind power energy, tidal energy and other alternative energy are receiving a lot of attention as new energy sources. Especially, solar energy has attracted great attention as a new clean energy resource, and several types of the system, such as solar cells, have been developed and have attracted great research interest in several decades. However, one of the weak points of the solar energy cannot be stored, and energy conversion systems in which sunlight energy is transferred to storable energies are eagerly anticipated.

The photosynthesis in the plant is one of the great processes to utilize the sun light energy as an energy resource. The reaction of photosynthesis is as follows.

$$6\,H_2O + 6\,CO_2 \rightarrow 6\,O_2 + \left(CH_2O\right)_6$$

The carbohydrates synthesized by photosynthesis reaction are important energy sources to creatures, which are not only the plants but also animals. It should be noted that the

solar energy, which will not be able to stored, is converted to the chemical energy, which has chemical stability and can be stored. This energy conversion system would be expected as a model for effective utilization of the solar energy to solve the energy resources problem. A general outline of photosynthesis is (i) A light-harvesting complexes in a thylakoid membrane absorb the sunlight. (ii) The harvested excitation energy is transferred to a reaction center by an energy transfer reaction. (iii) The excitation energy is converted to electrochemical energy by a charge separation reaction in the reaction center. (iv) NADPH and ATP are synthesized by the result of proton transfer coupled with electron transportations. (v) NADPH and ATP induce the synthesis of carbohydrate from CO_2 and H_2O. However, the detail mechanism of photosynthesis abundantly complicated, many researchers have investigated the mechanism of each step of photosynthesis by each original approaches to reveal the detail mechanism of photosynthesis.

1.2. Functionality and structure of the light harvesting system and reaction center[5-12,115]

As described in 1.1 in chapter 1, lots of researchers have investigated to reveal the mechanism of the photosynthesis. Especially the initial process of the photosynthesis has attracted great research interests because of the uniqe photo-functionality. Sunlight energy is absorbed in the light harvesting system at initial process of photosynthesis, and the excitation energy is transported to reaction center via energy transfer reaction. The light harvesting complexes consist of the core-antenna and peripheral antenna. The

core antenna was constructed around the reaction center, and peripheral antenna inhibits around this reaction center – core antenna complex. The peripheral antenna has crucial roles to adapt successfully to the environment changes, such as the strength of the light. These light-harvesting systems consist of chlorophylls, bacteriochlorophylls, and carotenoids which have a large molar extinction coefficient. Recently, the structure of the light harvesting complexes has been investigated by X-ray and microscopy analysis, and it is revealed that assembled dyes compose the light harvesting system. The image of the light harvesting system in *Rps. acidophyla* bacteria was shown in Figure 1.

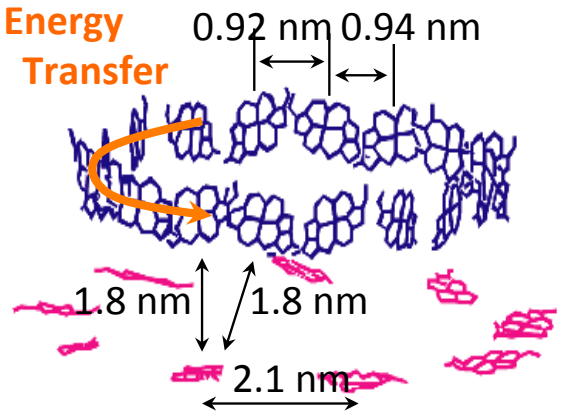

Figure 1. Light harvesting system in *Rps. acidophyla* bacteria[7]

To realize the functionality as the light harvesting system, not only the appropriate functional dyes, but also this beautiful assembled structure composed of functional dyes are necessary.

On the other hand, electron transfer reaction, which is thought to be the essential for the light reaction of photosynthesis, proceeds in the reaction center. This process is extremely important from the point of view of the energy conversion, and there are lots

of researches regarding to the reaction center of the photosynthesis. The structure of the reaction center has been also investigated with X-ray or other techniques, and the dynamics of electron transfer reaction in the reaction center has been investigated with the laser flash photolysis and time resolved electron spin resonance. The structural image of the reaction center is shown in Figure 2.

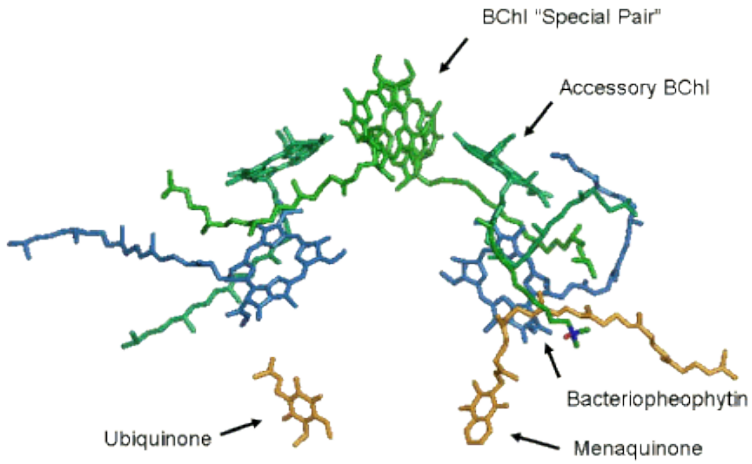

Figure 2. Image of the reaction center[115]

The photoinduced electron transfer reaction has researched as one of the fundamental photoreaction for a long time. Photoinduced electron transfer is an excited state electron transfer process by which excited electron is transferred from donor to acceptor. Due to this reaction, the radical ion pair (donor cation radical and acceptor anion radical) is generated, and it is called charge separation state. Generally, charge separation state is promptly decreased via back electron transfer or charge recombination, which is the electron transfer reaction from acceptor anion radical to donor cation radical, thus life

time of the charge separation state is not long. However, long-lived charge separation state is achieved in the reaction center by suppression of the charge recombination of radical ion pair. The electron transfer reaction in the reaction center is the successive reaction, that is (i) excitation of the special pair which would be dimer of chlorophyll-*a*,(ii) photoinduced electron transfer reaction to bacteriopheophytin, (iii) electron transfer reaction from bacteriopheophytin to quinone-a, (iv) electron transfer reaction from quinone-a to quinone-b. The time scale of the each electron transfer reaction in the reaction center is summarized in Figure 3.

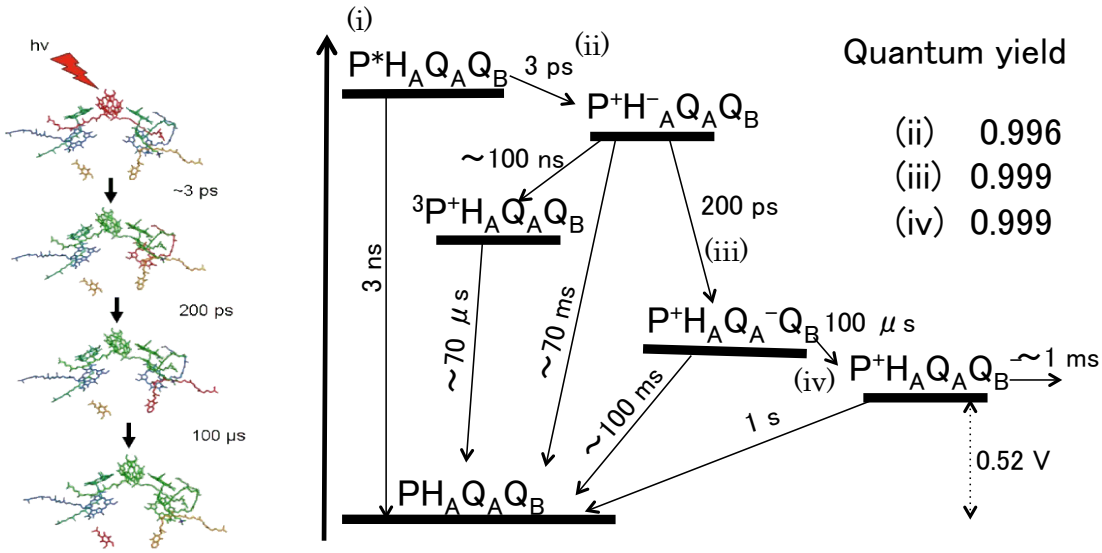

Figure 3. Energydiagram of the electron transfer reaction in the reaction center

As summarized in Figure 3, the stepwise electron transfer reactions proceed and the charge recombination reactions are suppressed in every process. One of the important factors to suppress the charge recombination is the apposite reorganization energy,

which is required energy for the reorganization of the solvent around the ion and reorganization of the molecule structures. In addition, the stepwised charge transportation is also crucial important point to achieve the long-lived charge separation state, and assembly of the molecules would be also important to achieve this stepwise electron transfer reaction as described in later.

1.3. Dependency of the inter distance and relative orientation of the molecules on photochemical reactions[13-26]

Energy transfer and electron transfer reaction are two of the most important interaction between excited molecules and other grand state molecule. The paradigm of the energy transfer and electron transfer reaction is shown in Scheme 1.

$$A^* + B \rightarrow A + B^* \qquad (a)$$
$$A^* + B \rightarrow A^{+\bullet} + B^{-\bullet} \qquad (b)$$

Scheme 1. Paradigm of the energy transfer reaction (a) and electron transfer reaction (b)

where * indicates electrically excited state, A and B indicates donor and acceptor in each reaction, respectively. The energy transfer reaction can be categorized into three types by their mechanism. In this section, the energy transfer reaction by the dipole-dipole interaction is mainly described. The energy transfer reaction by the dipole-dipole interaction is known as fluorescence resonance energy transfer (generally called FRET) or Förster-type energy transfer. This dipole-dipole interaction occurs

through oscillating electrical field, and it should be noted that FRET does not involve the overlap of the orbital. The theoretical energy transfer rate constant for Förster-type is expressed in following equation 1.

$$k_{ET} = \frac{9000 \ln 10 \kappa^2 \phi_D}{128 \pi^5 n^4 N \tau R^6} \int f_D(\nu) \varepsilon_A(\nu) \frac{d\nu}{\nu^4} \qquad \text{(eq. 1)}$$

where φ_D is the fluorescence quantum yield of the donor molecules, n is reflective index of the medium, N is Avogadro's number, is the orientation factor, τ_D is the excited life-time of donor in the absence of acceptor, R is the inter molecular distance between energy donor and acceptor (center to center), and the integral part represents the spectral overlap between absorption spectrum of energy acceptor and fluorescence spectrum of energy donor, respectively. On the other hand, electron transfer reaction whose paradigm is showed in scheme 1-(b) requires the orbital overlap. The inter molecular distance dependency of the electron transfer reaction has been investigated for a long time, the theory of the electron transfer has been developed by Murcus, Libby, Rehm, Weller and other huge number of researchers. It has revealed the dependency of the electron transfer reaction on inter distance and relative orientation of the molecules between electron donor and acceptor as shown in following equation 2.

$$k_{el} = k_{el}^0 \exp\left[-\beta(d - d_0)\right] \qquad \text{(eq. 2)}$$

where k_{el} indicates electron transfer rate constant, β is the orbital parameter which is in inverse proportion to overlap integration of the orbital of electron donor and acceptor, d is the inter molecular distance between electron donor and acceptor, d_0 is the van der Waals distance. Considering these dependencies of the energy transfer and electron transfer reaction on the inter distance and relative orientation between donor and acceptor molecules, control of these parameter is thought to be the crucial point to control these reaction and to realize the excellent photo-functionalities such as light harvesting system and reaction center.

1.4. **Assemblies of the organic molecules and their photo-functionality**[27-52]

As described in above section, assemble structures of photo-functional dyes show the unique photochemical or photophysical proterties such as light harvesting system and reaction center in natural photosynthesis. Inspired these researches, the assembly of the organic molecules has been investigated in several decades, and photo-functionalities of the assembled functional dyes have been demonstrated in the several system. One of the central systems to assemble the functional dyes is the covalent linked system where functional dyes are linked via covalent bond. The functional dyes are linked via covalent bond in this system, thus inter-molecular distances and relative orientation between energy donor and acceptor were strongly immobilized. The energy transfer or/and electron transfer reaction have been investigated between covalent linked a donor molecule and an acceptor molecule in several decades. These crucial works have developed the theories of these reactions and achieved the efficiently energy transfer

reaction and long-lived charge separation state. In the context of these great works, the energy / electron transfer reaction has been investigated between several donors and acceptors in recent years. Gust et al. investigated an antenna property of molecule shown in Figure 4, and they revealed the pH dependency of the energy transfer behavior this dye.

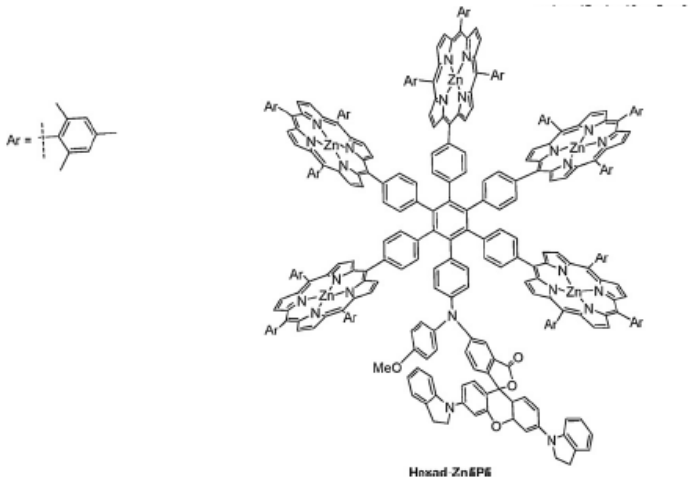

Figure 4. Structure of the antenna molecule synthesized and investigated by Gust *et al.*[32]

The molecule featured five porphyrin antenna moieties and a pH-sensitive dye. The energy transfer behavior was significantly depends on the pH values. Okada and co-workers synthesized a huge antenna molecule, as it is called dendrimer, as shown in Figure 5.

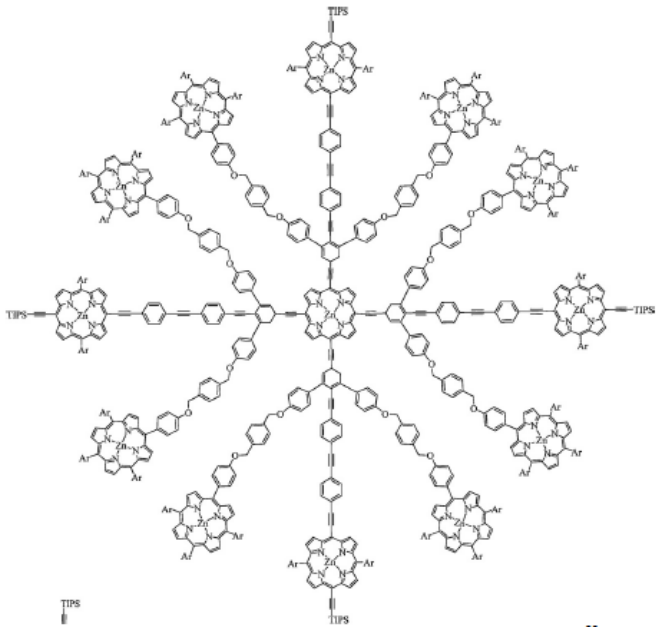

Figure 5. Dendrimer type antenna molecule reported by Okada *et al.*[35]

The energy transfer reaction took place from peripheral porphyrin molecules to the central porphyrin molecule judging from time resolved fluorescence spectroscopy. These researches constitute a new and important step to achieve the artificial light harvesting system. However, the synthesis and purification of the molecules are generally complicated, and these complications are bottlenecks for this covalent bonded system. On the other hand, supra molecules system would be another central system to construct the assembly of the functional dyes. It is supposed that dye aggregation, whose theory was established by Kasha *et al.*, in solution is the pioneer works for construction of the dye assembly in solution. This supra molecules assembly is thought to be the flagship to construct the dyes assembly which has superior photo-functionality such as artificial light harvesting system. For example, Kobuke and co-workers have reported the ring shaped supra molecules system similar to the light harvesting system

composed of the Zinc porphyrin derivatives.

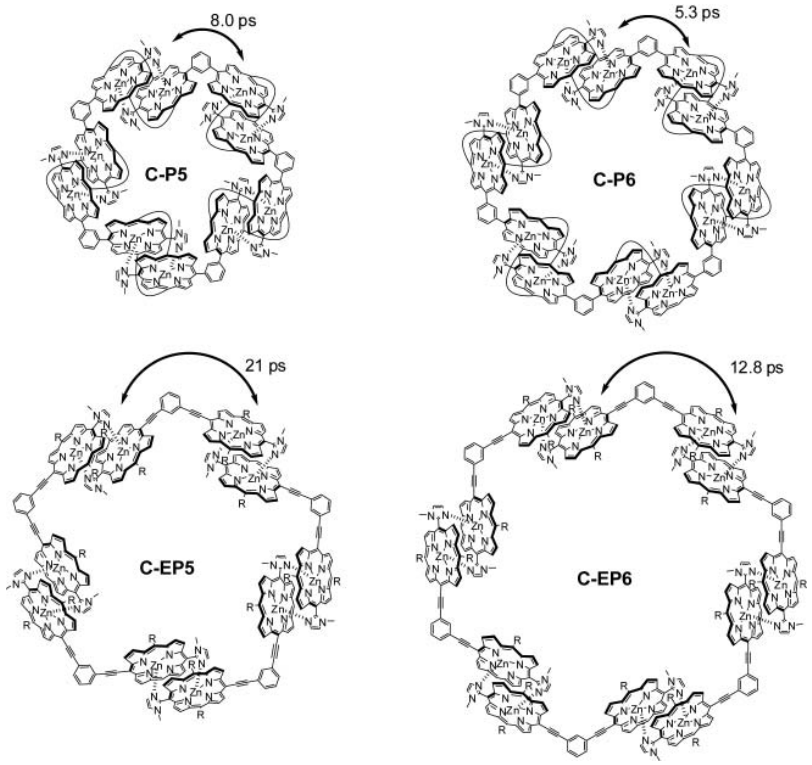

Figure 6. Supramolecular porphyrin macro-rings reported by Kobuke *et al.*[44]

Tamiaki *et al.* reported the supramolecular chlorin assembly as artificial lightharvesting device (Figure 7). An efficient energy transfer between porphyrins took place in the dye assembly.

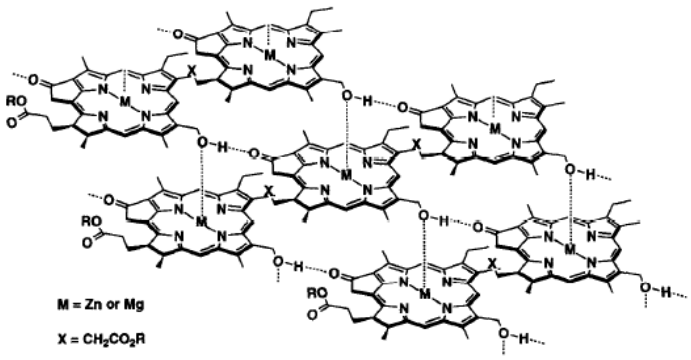

Figure 7. The assembly strucuture of chlorins investigated by Tamiaki and co-workers[31]

The constructions of the supramolecular assembly in the solid state and their photo-functionalities have been demonstrated. Hupp and co-workers have reported the energy transfer and energy migration proceed in the ordered metal organic frameworks system. The structural image and photograph of obtained crystal is shown in Figure 8.

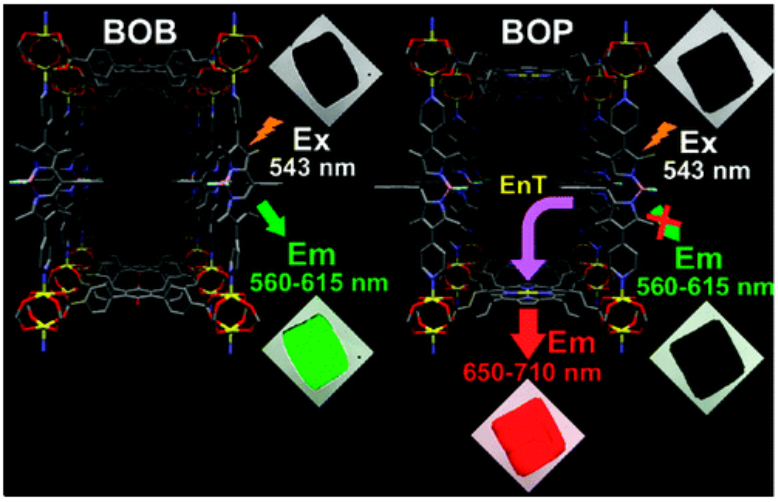

Figure 8. Structural image and photograph of the metal organic frameworks reported by Hupp and co-workers[48]

The excitation energies were migrated between energy donor (bodipy), which show the green fluorescence, and energy transfer took place between bodipy and energy acceptor molecule (porphyrin), which shows the red fluorescence. Kuhn, Moebius and co-workers focus attention on self-assembled monolayer dyes obtained by Langmuir--Blodgett (LB) technique. They have investigated the electron and energy transfer reaction between J-aggregate (head to tail type aggregate) of amphiphilic cyanines in LB film. These crucial works have verified the dependency of the energy transfer reaction on distance. Whitten and co-workers reported the "super quenching", that is the quenching of the large number of donor molecules by the small number of quencher molecules, in the J-aggregate type assembly system. These crucial works, in which the properties of Frenkel exciton was deftly utilized, have much greater hope for construction of the artificial light harvesting system, because the essence of this investigation, that is the concentration of light energy absorbed by donor molecules to the small number of acceptor molecules, is resemble to the light harvesting system.

1.5. Gold nano particles[53-82]

The above section explains the assembly structure of organic molecules and functionality of them, but the assembly structure of inorganic nano-particles is another interesting topic investigated in recently years. It has been revealed that the nanometer order inorganic nano particles show the interesting optical, electrical and magnetical properties which are different from the properties of bulk materials in several decades. Especially, gold nano particle has been gathering the attention since Haruta and

co-workers reported the catalysis activity of the gold nano particles deposited on the supporting materials surfaces. In addition to this pioneer works, the synthesis of the gold nano cluster stabilized by protective reagent reported by Schumid and Brust *et al.* would be the breakthrough for the investigation of gold nano clusters. Recently, there are huge number of the reports of gold nano cluster and their properties. Schmid defined the cluster as the nano particles which was exactly defined in chemical composition and structure. On the other hand, assembly of the gold nano clusters also has investigated with the development of the synthesis technique of the gold nano clusters. Teranishi and co-workers demonstrate the excellent assembly of gold nano cluster at the air-liquid interface by π-π interaction of the ligand as shown in Figure 9.

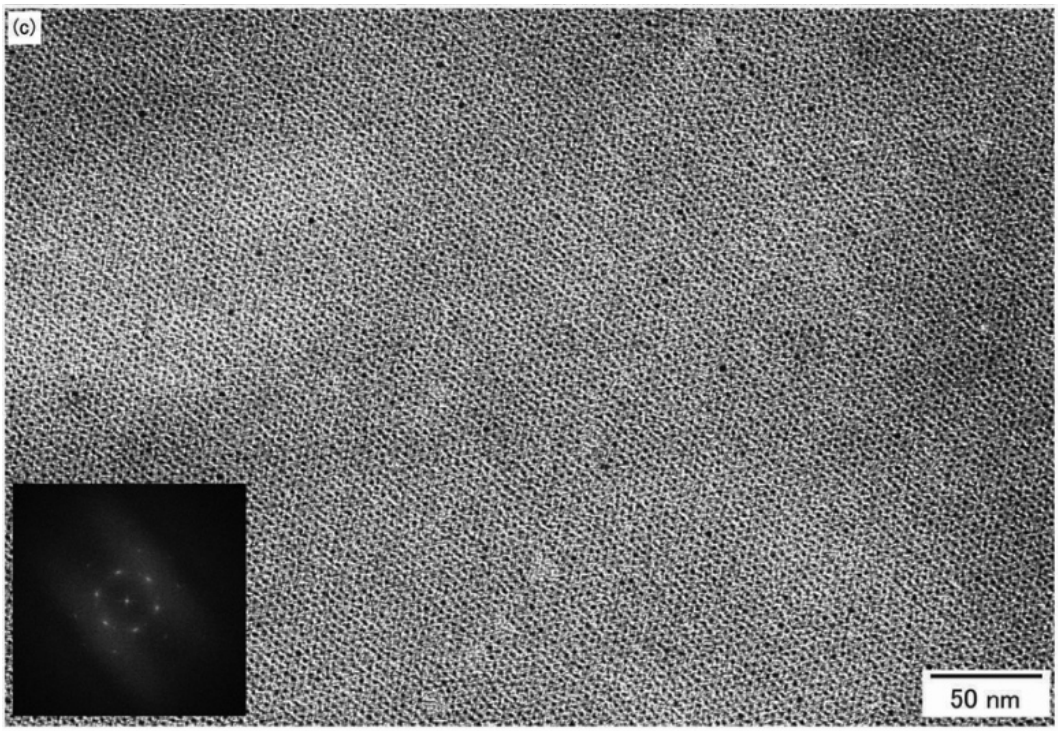

Figure 9. The gold nano cluster assembly reported by Teranishi *et al.*

(Inset is the fast Fourier transform spots)[70]

The well ordered gold nano clusters attracted much attention for their potential in single-electron-tunneling devices. However, the protective ligand which requires to stabilize and to assemble the gold nano cluster affect the properties of gold nano clusters. Teranishi and co-workers demonstrated that, for ~2 nm alkanethiol-protected Au nanoparticles, the tunneling resistance of the alkanethiol layer changes from 8.5 GΩ (1-octanethiol) to 500 MΩ (1-hexanethiol), implying that the shorter ligand is desirable for a drastic reduction of the tunneling resistance. Considering this demonstration, the utilization of strong protecting reagents, such as thiol derivatives, is not favored for the some further applications.

1.6. Host materials as a reaction field[83-100]

Various host materials, such as micelle, clathrate, mesoporous materials, zeolites and nano-sheet materials have been investigated in several decades, and the guest organic molecules in the nano-spaces in these host materials shows interesting photo-physical and photochemical behaviors which are different from photochemical or photochemical behaviors in solution. Especially, layered material is one of the interesting host materials because of the unique nano spaces supplied by the nano-sheets. We focused on the clay minerals, which is one of the well-known inorganic layered materials, as the pho-chemical reaction fields. Typical clay layer consists of two sheets of tetrahedral layer and an octahedral layer as shown in Figure 10.

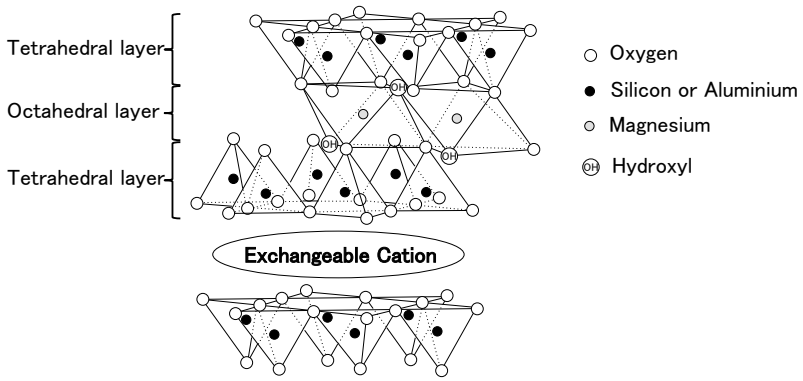

Figure 10. The structure of saponite clay mineral

The nano-sheet of the clay minerals is two dimensionally expanded with 10-1000 nm (diameter), and the thickness of the neno-sheets is 0.97 nm. The surfaces of the clay minerals have negatively charge by the isomorphous-replacement of element in the layer. Owing to the charges, the interlayer of the clay minerals can swelled, and each nano-sheets can be exfoliated each other in some conditions. This swelling and exfoliation ability depends on the exchangeable cation and the type of the clay minerals. Some researchers revealed dependency of the interlayer distance on the relative humidity and counter cation. Clay minerals are classified by the their structure, chemical formulation and the charge exchangeable capacity. A general classification of clay minerals is shown in Table 1.

Table 1. Classification of the clay minerals[85]

Clay	Ideal composition $M_{int}(M_{oct})(M_{tetra})O_1(OH)_m \cdot nH_2O$[a]	Layer type	Schematic structure[b]
1:1			
Kaolinite group (charge density ~ 0 per unit)			
Kaolinite	$(Al_2)(Si_2)O_5(OH_4)$	Dioctahedral	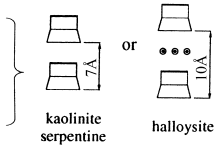
Halloysite	$(Al_2)(Si_2)O_5(OH_4)\cdot 2H_2O$	Dioctahedral	
Serpentine group (charge density ~ 0 per unit)			
Serpentine	$(Mg_6)(Si_4)O_{10}(OH)_8$	Trioctahedral	
2:1			
Pylophyllite group (charge density ~ 0 per unit)			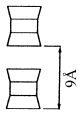
Pyrophyllite	$(Al_2)(Si_4)O_{10}(OH)_2$	Dioctahedral	
Talc	$(Mg_3)(Si_4)O_{10}(OH)_2$	Trioctahedral	
Smectite group (charge density: x ~ 0.2–0.6 per unit)			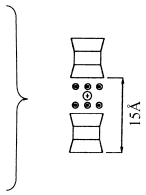
Montmorillonite	$M_x(Al_{2-x}Mg_x)(Si_4)O_{10}(OH)_2\cdot nH_2O$	Dioctahedral	
Beidellite	$M_x(Al_2)(Si_{4-x}Al_x)O_{10}(OH)_2\cdot nH_2O$	Dioctahedral	
Nontronite	$M_x(Fe_2^{3+})(Si_{4-x}Al_x)O_{10}(OH)_2\cdot nH_2O$	Dioctahedral	
Saponite	$M_x(Mg_3)(Si_{4-x}Al_x)O_{10}(OH)_2\cdot nH_2O$	Trioctahedral	
Hectorite	$M_x(Mg_{3-x}Li_x)(Si_4)O_{10}(OH)_2\cdot nH_2O$	Trioctahedral	
Vermiculite group (charge density: x ~ 0.6–0.9 per unit)			
Dioctahedral vermiculite	$M_x(Al_{2-y}Fe_4^{3+})(Si_{4-x}Al_x)O_{10}(OH)_2\cdot nH_2O$	Dioctahedral	
Trioctahedral vermiculite	$M_x(Mg_3)(Si_{4-x}Al_x)O_{10}(OH)_2\cdot nH_2O$	Trioctahedral	
Mica group (charge density: x ~ 0.6–1 per unit)			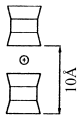
Mica (muscovite)	$K(Al_2)(Si_3Al)O_{10}(OH)_2$	Dioctahedral	
Illite	$K_x(Al_2)(Si_{4-x}Al_x)O_{10}(OH)_2$	Dioctahedral	
Biotite	$K[(Mg, Fe^{2+})(Fe^{3+}, Al, Ti)](Si, Al)_4O_{10}(OH)_2$	Trioctahedral	
Chlorite group			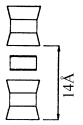
Cookeite	$[LiAl_2(OH)_6][(Al_2)(Si_3Al)O_{10}(OH)_2]$	Dioctahedral	
Clinochlore	$[Mg_2Al\ (OH)_6][(Mg_3)(Si_3Al)O_{10}(OH)_2]$	Trioctahedral	
Chamosite	$[Fe_2Al\ (OH)_6][(Mg_3)(Si_3Al)O_{10}(OH)_2]$	Trioctahedral	
Channel type			
Sepiolite	$M^{2+}_{(x+y+2z)/2}(Mg_{8-y-z}M_y^{3+}\square_z)$ $(Si_{12-x}M_x^{3+})O_{30}(OH)_4(OH_2)_4\cdot 8H_2O$		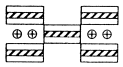
Palygorskite	$M^{2+}_{(x-y+2z)/2}(Mg_{5-y-z}M_y^{3+}\square_z)$ $(Si_{8-x}M_x^{3+})O_{20}(OH)_2(OH_2)_4\cdot 4H_2O$		

[a] M_{int}: intercalated metal cations; M_{oct}: cations occupying octahedral position; M_{tetra}: cations occupying tetrahedral position.
[b] ▱: tetrahedral sheet; ▭: octahedral sheet; ▬: OH surface; ⊙: H_2O; ⊕: interlayer cation.

Lots of the clay minerals has been reported several production area. Also clay minerals can be synthesized via hydrothermal reaction, and some researchers reported the novel mild condition synthesis method of the clay minerals. The chemical structure and composition of synthetic clay minerals is changeable by the synthetic procedure and the precursors. Bujdak *et al.* has been reported a unique technique to control the charge

density of Montmorillonite, which is one of the typical clay minerals. The details of the clay minerals (structure, composition and so on) is characterized by NMR, X-ray diffraction, elemental analysis, electron microscopy, scanning probe microscopy, and other techniques. The clay minerals have been attracted attention as a host materials and reaction fields same as other layered materials. One of the interesting properties of the layered materials is the interlayer space between the stacked nano-sheets. As described above, this interlayer space is changeable by their medium and guest materials. For example, it has been revealed that the intercalation of the cationic surfactant induces the expanding of the interlayer spaces. It has been researched not only these intercalation reactions of the surfactant but also the intercalation reaction of the guest dyes and the photochemical / photo-physical properties of these hybrid materials. In addition, the clay nano-sheets can be exfoliated and well dispersed in some of the solvents. Synthetic saponite is exfoliated and dispersed in water, and this exfoliated clay nano-sheets supply the two-dimensional flat interface. These exfoliated or stacked clay nano-sheets performs as the host materials for cationic dyes which adsorbs on clay surfaces via electrostatic interaction, and some of the these guest dyes on clay minerals shows the unique photo-physical or photochemical properties which is different from the properties in solution.

1.7. Assembly of the dyes on the clay surfaces[101-114]

The adsorption behavior and photo-physical properties of cationic dyes on the surfaces / interlayer spaces of exfoliated clay have been investigated in several decades. The cationic dyes can adsorb on the clay surfaces via electrostatic interaction and hydrophobic interaction in aqueous media. The researches demonstrated by Takagi and co-workers have revealed the adsorption behaviors of the multivalent cationic dyes on saponite clay surfaces. In their works, they demonstrate the formation of the unique hybrid materials composed of multivalent cationic dyes and saponite clay. The chemical composition of the saponite clay is expressed as $[(Si_{7.20}Al_{0.80})(Mg_{5.97}Al_{0.03})O_{20}(OH)_4]^{-0.77}(Na_{0.77})^{+0.77}$. The saponite clay is one of the trioctahedral smectite, and their diameter and thickness is ca. 20 nm and 0.97 nm, respectively. The replacement of Al^{3+} with Si^{4+} in tetrahedoral layer produces the anionic charges on the surfaces of clay nano-sheets, and counter cation of these anionic sites (generally Na^{+}) are exchangeable other cation. The average inter anionic distance is calculated as 1.2 nm from the cation exchange capacity of the synthetic saponite (1.00×10^{-3} eq g^{-1}) and their theoretical surface area (7.5×10^{2} m^2) on the basis of hexagonal array. This saponite clay is characterized as (i) transparency in the visible region because of not including the transition metal and weak Rayleigh / Mie scatter, (ii) cation exchangeable ability, (iii) flat and wide surfaces area, (iv) exfoliation or stack ability (depending on their medium). Takagi and co-workers have demonstrated the formation of the unique complex composed from multivalent cationic dyes and saponite clay, and they have investigated photochemical and photo-physical properties of the adsorbed

dyes on the saponite clay surfaces. Kerry, Takagi and Kawamata and other researchers have reported that the absorption spectra for adsorbed cationic porphyrin molecules (tetrakis(1-methylpyridinium-4-yl) porphyrin, abbreviated as TMPyP) on clay / intercalated in clay nano-sheets shows the red shift as shown in Figure 11.

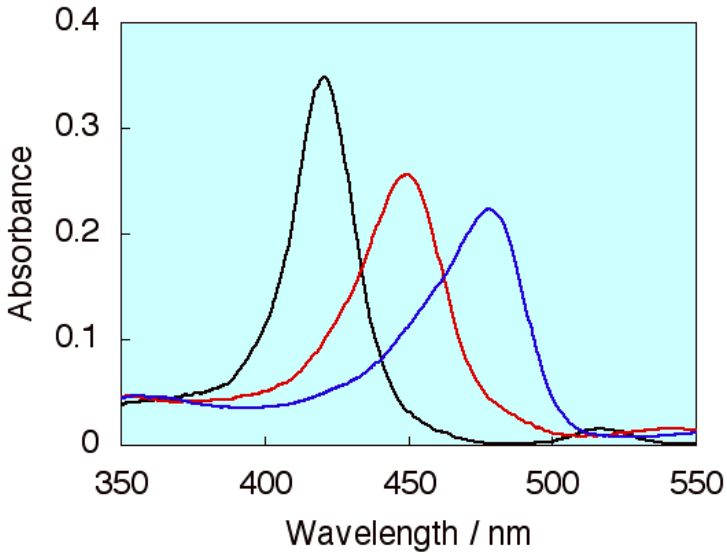

Figure 11. Absorption spectra of TMPyP (black line) in water, (red line) adsorbed on the clay surfaces, (blue line) intercalated in clay nano-sheets[116]

These spectral shifts of porphyrin molecules are ascribed to the coplanarization of the porphyrin ring and meso substituted pyridinium ring. The adsorbed/non-adsorbed porphyrin can be realized from this absorption spectral change. The absorption spectra of the TMPyP at various loading level and concentration−absorbance plot (Lambert-Beer like plot) was shown in Figure 12.

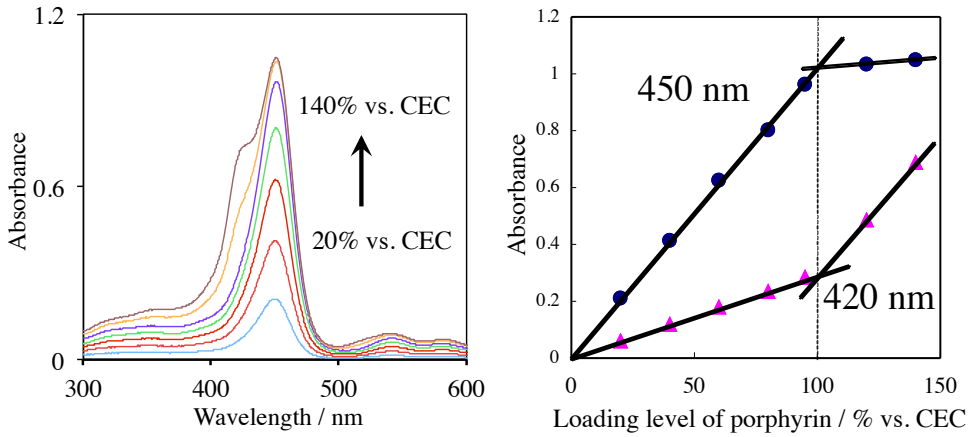

Figure 12. Left: Absorption spectra for TMPyP on the clay surface at various CEC conditions. Right: Absorbance concentration plot for p-TMPyP at 450 nm and 420 nm.

The shapes of absorption spectra was not changed up to 100% cation exchange capacity (CEC) of the saponite, and the plot linearity also kept up to 100% CEC of the saponite. The non-adsorbed TMPyP was observed over 100% versus CEC as shown in both of absorption spectra and Lambert-Beer like plot. These results indicate that TMPyP molecules adsorbed on saponite surfaces without aggregation till 100% versus CEC, and it also indicated that the TMPyP adsorb on the saponite surfaces with high density even at high dye loadings although the dyes adsorbed on solid surfaces tend to aggregation. The schematic representation for the TMPyP/clay complex is shown in Figure 13.

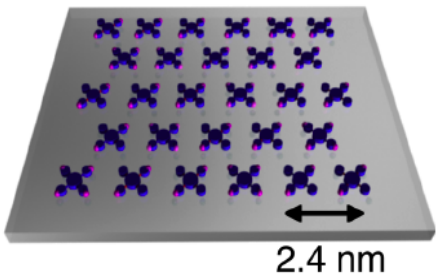

Figure 13. The schematic representation for TMPyP/clay complex. The average intermolecular distance under 100% CEC condition is 2.4 nm on the basis of a hexagonal array.

Takagi and co-workers have investigated to reveal the mechanism of this unique adsorption behavior and the formation of the dyes assembly on clay surfaces by the systematic experiments using several types of porphyrin derivatives and several aniconic charge density saponite clay. It was revealed that the 100% CEC adsorption without aggregation is observed only for limited porphyrins having limited molecular structures via those investigations. They indicates the crucial point for this unique adsorption behavior of the multivalent cationic dyes on saponite clay surfaces is the matching of the inter charge distances of the clay minerals and of the multivalent cationic dyes, and this effect was named as “Size-Matching Effect”. The saturated absorption amount dependency on the range difference between inter cationic distance of porphyrin molecules and inter anionic distance on the saponite clay was summarized in Figure 14.

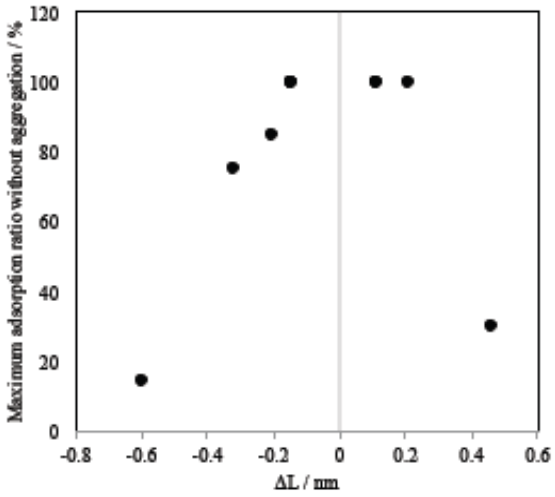

Figure 14. (a) The dependency of saturated absorption amount on the range difference between between inter cationic distance of porphyrin molecules and inter anionic distance on the saponite clay (**Δ**L).

The ΔL was calculated by following equation.

$$\Delta L = L_{clay} - L_{dye} \text{ (eq. 3)}$$

where L_{clay} indicates the inter anionic charge distance on saponite and L_{dye} indicates the inter cationic charge distance in porphyrin molecules, respectively. In the case of tetra cationic porphyrins-clay complexes, the average center-to-center intermolecular distance is calculated to be 2.4 nm at 100% CEC condition on the basis of hexagonal array. . Recently further investigation by Takagi and co-workers have suggested that this average intermolecular distance would be changeable by the host synthetic saponite whose charge density is controlled. This controlled assembly of porphyrin molecules on

the clay surfaces is most interesting from the viewpoint of photochemical reactions, since the some of the photochemical reactions depend on the intermolecular distance and relative orientation of the molecules. Also it should be noted that the aggregation behavior of the dyes was completely suppressed in this complex. The aggregation of the dyes should be suppressed because the aggregation induces the decreasing of the excited singlet lifetime of the dyes and complicated spectral changes.

One of the advantages to construct the non-aggregated assembly of the porphyrin molecules on the clay surfaces is the simplified technique to construct the dye assembly

This novel technique to assemble the dyes on the clay surfaces is simplified compared to other self-assembly techniques, and it can be treated in water, which is the versatile and clean solvent. Furthermore, external force, such as surface tension utilized in Langmuir−Blodgett film is not necessary in this technique. Another advantage of this self−assembly technique is the flexibility. As described above, the essence for the formation of assemble structure is the matching of the inter-charge distances on the host and guest materials is the crucial point, thus it is possible to utilize the wide variety of the multivalent cationic dyes. Furthermore, the intermolecular distance can be adjusted by host saponite clay minerals.

1.8. Purpose of this thesis

As described in the general introduction, we have investigated the self-assembly of the cationic dyes on the clay surfaces. Inspired these previous works, the author examines the construction of the novel nano-structure materials composed of the inorganic

layered materials, then the functionalities of the materials was examined in this thesis. This thesis consists of the following three parts.

(i) Construction of the gold nano particles assembly on the clay surfaces

In our groups' previous work, we have demonstrated the construction of porphyrin molecules assembly on the clay surfaces. However, we have never investigated the construction of the inorganic nano particles assembly on the clay surfaces. In this section, we examined the construction of assembly of gold nano particles, which have unique behaviors inorganic nano particles, along with porphyrin molecules. The ideal image of the objective structure is shown in Figure 15.

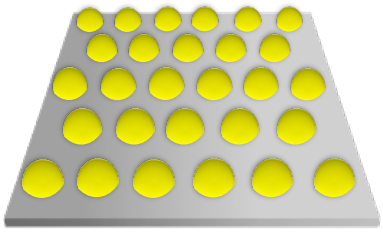

Figure 15. Ideal and objective structure of gold nano particles assembly on the clay surfaces

(ii) Construction of a accumulated structure of porphyrin/clay complex and the photo-functionality of the porphyrin molecules

In our previous work, we have investigated the two dimensional assembly of the dyes on the clay surfaces. In this works, we examined the construction of the

three-dimensional structure based on the two-dimensional porphyrin assembly. Specifically, the porphyrin/clay complexes were accumulated on the substrate, and the aimed three-dimensional structure is alternately accumulated structure composed of porphyrin monolayer and clay layer. Also the photo-functionality of the porphyrin molecules sandwiched by clay nano-sheets was investigated. The ideal image of the objective structure is shown in Figure 16.

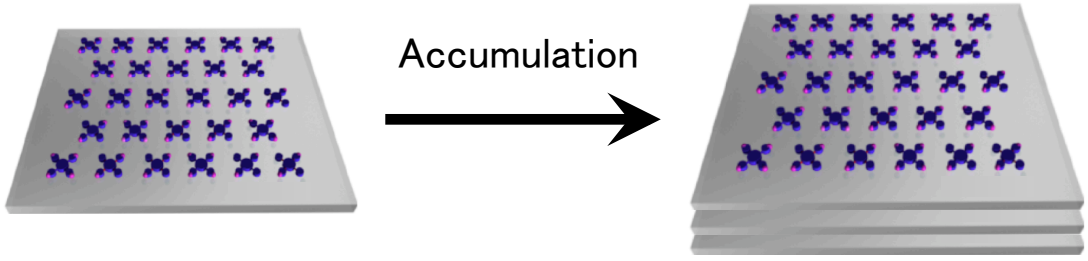

Figure 16. The ideal structure of alternately accumulated structure composed of porphyrin molecules and clay minerals

(iii) Construction of the three component dyes' assembly on clay surfaces and the photochemical reaction flow control utilizing the molecular container

In this work, the non-aggregated assembly structure composed of three kinds of dyes was constructed on the clay surfaces. The image of the this system is shown in Figure 17.

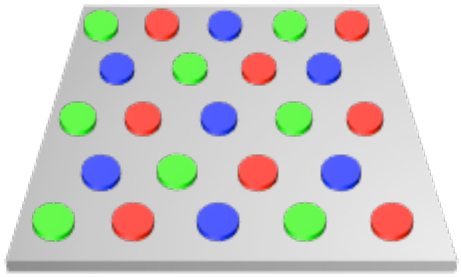

Figure 17. Image of the system in (iii)

We demonstrated an energy transfer reaction and subsequent electron transfer reaction, which is photochemical reaction flow control in energy donor, energy acceptor (as well as electron donor) and electron acceptor assembly on inorganic surfaces. To suppress the side reaction and to control the reaction flow, the cationic capsule molecules, which is container-like clathrate compound, was utilized.

The investigation of (i), (ii) and (iii) were described in Chapter 2-4, Chapter 5-6 and Chapter 7, respectively. Author examines the several approaches to construct the above novel nano-structure materials composed of the inorganic layered materials and to investigate their functionalities.

1.9. References

1. Barber, J.; Andersson, B. *Nature* 1994, *370*, 31.

2. Inoue, H.; Funyu, S.; Shimada, Y.; Takagi, S. *Pure and Appl. Chem.* 2005, *77*.

3. Glazer, A. N. *Annu. Rev. Biochem.* 1983, *52*, 125.

4. Voet, D.; Voet, J. G. Biochemistry, Wiley, New York, 1995.

5. Hu, X.; Schulten, K. *Physics Today* 1997, *50*, 28.

6. McDermott, G.; Prince, S. M.; Freer, A. A.; Hawthornthwaite-Lawless, A. M.; Papiz, M. Z.; Cogdell, R. J.; Isaacs, N. W. *Nature* 1995, *374*, 517.

7. Hu, X.; Ritz, T.; Damjanović, A.; Schulten, K. *J. Physical Chem. B* 1997, *101*, 3854.

8. Leslie Dutton, P.; Leigh, J. S.; Seibert, M. *Biochem. and Biophys. Res. Commun.* 1972, *46*, 406.

9. Deisenhofer, J.; Epp, O.; Miki, K.; Huber, R.; Michel, H. *Nature* 1985, *318*, 618.

10. Michel, H.; Deisenhofer, J. *Biochemistry* 1988, *27*, 1.

11. Stowell, M. H. *Science* 1997, *276*, 812.

12. Kuglstatter, A.; Ermler, U.; Michel, H.; Baciou, L.; Fritzsch, G. *Biochemistry* 2001, *40*, 4253.

13. Libby, W. F. *J. Phys. Chem.* 1952, *56*, 863.

14. Marcus, R. A. *Annu. Rev. Phys. Chem.* 1964, *15*, 155.

15. Marcus, R. A.; Sutin, N. *Biochimica et Biophysica Acta (BBA) - Reviews on Bioenergetics* 1985, *811*, 265.

16. Closs, G. L.; Miller, J. R. *Science* 1988, *240*, 440.

17. Fleming, G. R.; Wolynes, P. G. *Physics Today* 1990, *43*, 36.

18. Barbara, P. F.; Walker, G. C.; Smith, T. P. *Science* 1992, *256*, 975.

19. Barbara, P. F.; Meyer, T. J.; Ratner, M. A. *J. Phys. Chem.* 1996, *100*, 13148.

20. Albinsson, B.; Martensson, J. *J. Photochem. Photobiol. C: Photochem. Rev.* 2008, *9*, 138.

21. Förster, T. *Annalen der Physik* 1948, *437*, 55.

22. Dexter, D. L. *J. Chem. Phys.* 1953, *21*, 836.

23. Förster, T. *Discuss. Faraday Soc.* 1959, *27*, 7.

24. Kasha, M. *Rad. Res.* 1962, *20*, 53.

25. Turro, N. J. *Modern Molecular Photochemistry*; University Science Books, Mill Valley, CA 1991.

26. Kavarnos, G. J. *Fundamental of photoinduced electron transfer*; VCH Publishers, 1993

27. Tamiaki, H. *Coord. Chem. Rev.* 1996, *148*, 183.

28. Panda, M. K.; Ladomenou, K.; Coutsolelos, A. G. *Coord. Chem. Rev.* 2012, *256*, 2601.

29. Maeda, C.; Kim, P.; Cho, S.; Park, J. K.; Lim, J. M.; Kim, D.; Vura-Weis, J.; Wasielewski, M. R.; Shinokubo, H.; Osuka, A. *Chemistry* 2010, *16*, 5052.

30. Kuramochi, Y.; Satake, A.; Sandanayaka, A. S.; Araki, Y.; Ito, O.; Kobuke, Y. *Inorg. Chem.* 2011, *50*, 10249.

31. Prokhorenko, V. I.; Holzwarth, A. R.; Müller, M. G.; Schaffner, K.; Miyatake, T.; Tamiaki, H. *J. Phys. Chem. B* 2002, *106*, 5761.

32. Terazono, Y.; Kodis, G.; Bhushan, K.; Zaks, J.; Madden, C.; Moore, A. L.; Moore,

T. A.; Fleming, G. R.; Gust, D. *J. Am. Chem. Soc.* 2011, *133*, 2916.

33. Liu, J. Y.; El-Khouly, M. E.; Fukuzumi, S.; Ng, D. K. *Chemistry* 2011, *17*, 1605.

34. Fukuzumi, S.; Saito, K.; Ohkubo, K.; Khoury, T.; Kashiwagi, Y.; Absalom, M. A.; Gadde, S.; D'Souza, F.; Araki, Y.; Ito, O.; Crossley, M. J. *Chem. Commun.* 2011, *47*, 7980.

35. Uetomo, A.; Kozaki, M.; Suzuki, S.; Yamanaka, K.; Ito, O.; Okada, K. *J. Am. Chem. Soc.* 2011, *133*, 13276.

36. Liddell, P. A.; Kodis, G.; Moore, A. L.; Moore, T. A.; Gust, D. *J. Am. Chem. Soc.* 2002, *124*, 7668.

37. Nakano, A.; Yamazaki, T.; Nishimura, Y.; Yamazaki, I.; Osuka, A. *Chem. A Eur. J.* 2000, *6*, 3254.

38. Guldi, D. M. *J. Phys. Chem. B* 2005, *109*, 11432.

39. Balaban, T. S. *Acc. Chem. Res.* 2005, *38*, 612.

40. Satake, A.; Tanaka, H.; Hajjaj, F.; Kawai, T.; Kobuke, Y. *Chem. Commun.* 2006, 2542.

41. Miyatake, T.; Tamiaki, H.; Holzwarth, A. R.; Schaffner, K. *Photochem. Photobiol.* 1999, *69*, 448.

42. Casey, J. P.; Bachilo, S. M.; Weisman, R. B. *J. Mater. Chem.* 2008, *18*, 1510.

43. Kaschak, D. M.; Lean, J. T.; Waraksa, C. C.; Saupe, G. B.; Usami, H.; Mallouk, T. E. *J. Am. Chem. Soc.* 1999, *121*, 3435.

44. Takahashi, R.; Kobuke, Y. *J. Am. Chem. Soc.* 2003, *125*, 2372.

45. Fujii, K.; Iyi, N.; Hashizume, H.; Shimomura, S.; Ando, T. *Chem. Mater.* 2009, *21*,

1179.

46. Kuroda, T.; Fujii, K.; Sakoda, K. *J. Phys. Chem. C* 2010, *114*, 983.

47. Schanze, K. S.; Silverman, E. E.; Zhao, X. *J. Phys. Chem. B* 2005, *109*, 18451.

48. Kelley, R. F.; Lee, S. J.; Wilson, T. M.; Nakamura, Y.; Tiede, D. M.; Osuka, A.; Hupp, J. T.; Wasielewski, M. R. *J. Am. Chem. Soc.* 2008, *130*, 4277.

49. Yoo, H.; Yang, J.; Nakamura, Y.; Aratani, N.; Osuka, A.; Kim, D. *J. Am. Chem. Soc.* 2009, *131*, 1488.

50. Miller, M. A.; Lammi, R. K.; Prathapan, S.; Holten, D.; Lindsey, J. S. *J. Org. Chem.* 2000, *65*, 6634.

51. Gilat, S. L.; Adronov, A.; Fréchet, J. M. J. *Angew. Chem. Inter. Ed.* 1999, *38*, 1422.

52. Choi, M.-S.; Aida, T.; Yamazaki, T.; Yamazaki, I. *Chem. A Eur. J.* 2002, *8*, 2667.

53. Haruta, M.; Yamada, N.; Kobayashi, T.; Iijima, S. *J. Catal.* 1989, *115*, 301.

54. Collings, B. A.; Athanassenas, K.; Lacombe, D.; Rayner, D. M.; Hackett, P. A. *J. Chem. Phys.* 1994, *101*, 3506.

55. Andres, R. P.; Bielefeld, J. D.; Henderson, J. I.; Janes, D. B.; Kolagunta, V. R.; Kubiak, C. P.; Mahoney, W. J.; Osifchin, R. G. *Science* 1996, *273*, 1690.

56. Feldheim, D. L.; Keating, C. D. *Chem. Soc. Rev.* 1998, *27*, 1.

57. Hostetler, M. J.; Wingate, J. E.; Zhong, C. J.; Harris, J. E.; Vachet, R. W.; Clark, M. R.; Londono, J. D.; Green, S. J.; Stokes, J. J.; Wignall, G. D.; Glish, G. L.; Porter, M. D.; Evans, N. D.; Murray, R. W. *Langmuir* 1998, *14*, 17.

58. Aiken, J. D.; Finke, R. G. *J. Molecular Cataly. a-Chem.* 1999, *145*, 1.

59. Shah, P. S.; Holmes, J. D.; Doty, R. C.; Johnston, K. P.; Korgel, B. A. *J. Am. Chem.*

Soc. 2000, *122*, 4245.

60. Jamet, M.; Wernsdorfer, W.; Thirion, C.; Mailly, D.; Dupuis, V.; Mélinon, P.; Pérez, A. *Phys. Rev. Lett.* 2001, *86*, 4676.

61. Beverly, K. C.; Sampaio, J. F.; Heath, J. R. *J. Phys. Chem. B* 2002, *106*, 2131.

62. Kanehara, M.; Oumi, Y.; Sano, T.; Teranishi, T. *J. Am. Chem. Soc.* 2003, *125*, 8708.

63. Sohn, B. H.; Choi, J. M.; Yoo, S. I.; Yun, S. H.; Zin, W. C.; Jung, J. C.; Kanehara, M.; Hirata, T.; Teranishi, T. *J. Am. Chem. Soc.* 2003, *125*, 6368.

64. Daniel, M. C.; Astruc, D. *Chemical Reviews* 2004, *104*, 293.

65. Wilcoxon, J. P.; Provencio, P. P. *J. Am. Chem. Soc.* 2004, *126*, 6402.

66. Hussain, I.; Graham, S.; Wang, Z. X.; Tan, B.; Sherrington, D. C.; Rannard, S. P.; Cooper, A. I.; Brust, M. *J. Am. Chem. Soc.* 2005, *127*, 16398.

67. Negishi, Y.; Nobusada, K.; Tsukuda, T. *J. Am. Chem. Soc.* 2005, *127*, 5261.

68. Zhang, H.; Yasutake, Y.; Shichibu, Y.; Teranishi, T.; Majima, Y. *Phys. Rev. B* 2005, *72*.

69. Azuma, Y.; Kanehara, M.; Teranishi, T.; Majima, Y. *Phys. Rev. Lett.* 2006, *96*.

70. Kanehara, M.; Kodzuka, E.; Teranishi, T. *J. Am. Chem. Soc.* 2006, *128*, 13084.

71. Nehl, C. L.; Liao, H.; Hafner, J. H. *Nano. Lett.* 2006, *6*, 683.

72. Newman, J. D. S.; Blanchard, G. J. *Langmuir* 2006, *22*, 5882.

73. Jain, P. K.; Huang, X.; El-Sayed, I. H.; El-Sayed, M. A. *Plasmonics* 2007, *2*, 107.

74. Corma, A.; Garcia, H. *Chem. Soc. Rev.* 2008, *37*, 2096.

75. Johansson, M.; Lechtken, A.; Schooss, D.; Kappes, M.; Furche, F. *Phys. Rev. A* 2008, *77*.

76. Hallett-Tapley, G. L.; Silvero, M. J. n.; González-Béjar, M. a.; Grenier, M.; Netto-Ferreira, J. C.; Scaiano, J. C. *J Phys. Chem. C* 2011, *115*, 10784.

77. Kamei, Y.; Shichibu, Y.; Konishi, K. *Angew. Chem.* 2011, *50*, 7442.

78. Scaiano, J. C.; Netto-Ferreira, J. C.; Alarcon, E.; Billone, P.; Alejo, C. J. B.; Crites, C.-O. L.; Decan, M.; Fasciani, C.; González-Béjar, M.; Hallett-Tapley, G.; Grenier, M.; McGilvray, K. L.; Pacioni, N. L.; Pardoe, A.; René-Boisneuf, L.; Schwartz-Narbonne, R.; Silvero, M. J.; Stamplecoskie, K. G.; Wee, T.-L. *Pure Appl. Chem.* 2011, *83*.

79. Teranishi, T.; Sakamoto, M. *J. Phys. Chem. Lett.* 2013, *4*, 2867.

80. Ueno, K.; Misawa, H. *NPG Asia Materials* 2013, *5*, e61.

81. Haruta, M. *Gold Nanotechnology:Fundamentals and Applications,* CMC Publisher**, 2009**

82. Ohya, Y.; Miyoshi, N.; Hashizume, M; Tamaki, T.; i Uehara, T.; Shingubara, S.; Kuzuya, A. *Small*, **2012**, *8*, 2335

83. Smith, J. V. *Chem. Rev.* 1988, *88*, 149.

84. Kresge, C. T.; Leonowicz, M. E.; Roth, W. J.; Vartuli, J. C.; Beck, J. S. *Nature* 1992, *359*, 710.

85. Shichi, T.; Takagi, K. *J. Photochem. Photobiol. C: Photochem. Rev.* 2000, *1*, 113.

86. Thomas, J. K. *Chem. Rev.* 1993, *93*, 301.

87. Ogawa, M.; Kuroda, K. *Chem. Rev.* 1995, *95*, 399.

88. Bujdák, J.; Komadel, P. *J. Phys. Chem. B* 1997, *101*, 9065.

89. Lopezarbeloa, F.; Martinezmartinez, V.; Arbeloa, T.; Lopezarbeloa, I. *J. Photochem. Photobiol. C: Photochem. Rev.* 2007, *8*, 85.

90. Lu, L.; Jones, R. M.; McBranch, D.; Whitten, D. *Langmuir* 2002, *18*, 7706.

91. Brindley, G. W. *Clay Minerals* 1965, *6*, 91.

92. Suquet, H.; Calle, C. D. L.; Pezerat, H. *Clays and Clay Minerals* 1975, *23*, 1.

93. Ravina, I.; Low, P. F. *Clays and Clay Minerals* 1977, *25*, 201.

94. Suquet, H.; Pezerat, H. *Clays and Clay Minerals* 1987, *35*, 353.

95. Kloprogge, J. T. *J. Porous Mater.* 1998, *5*, 5.

96. Kloprogge, J. T.; Komarneni, S.; Amonette, J. E. *Clays and Clay Minerals* 1999, *47*, 529.

97. Bujdák, J. *Appl. Clay Sci.* 2006, *34*, 58.

98. Karmous, M. S.; Ben Rhaiem, H.; Robert, J. L.; Lanson, B.; Ben Haj Amara, A. *Appl. Clay Sci.* 2009, *46*, 43.

99. Zhang, D.; Zhou, C.-H.; Lin, C.-X.; Tong, D.-S.; Yu, W.-H. *Appl. Clay Sci.* 2010, *50*, 1.

100. Okada, T.; Ide, Y.; Ogawa, M. *Chemistry, an Asian journal* 2012, *7*, 1980.

101. Takagi, S.; Eguchi, M.; Tryk, D.; Inoue, H. *J. Photochem. Photobiol. C: Photochem. Rev.* 2006, *7*, 104.

102. Takagi, S.; Shimada, T.; Eguchi, M.; Yui, T.; Yoshida, H.; Tryk, D. A.; Inoue, H. *Langmuir* 2002, *18*, 2265.

103. Takagi, S.; Tryk, D. A.; Inoue, H. *J. Phys. Chem. B* 2002, *106*, 5455.

104. Eguchi, M.; Takagi, S.; Inoue, H. *Chem. Lett.* 2006, *35*, 14.

105. Shiragami, T.; Mori, Y.; Matsumoto, J.; Takagi, S.; Inoue, H.; Yasuda, M. *Colloid Surface A* 2006, *284*, 284.

106. Takagi, S.; Eguchi, M.; Tryk, D. A.; Inoue, H. *Langmuir* 2006, *22*, 1406.

107. Eguchi, M.; Tachibana, H.; Takagi, S.; Inoue, H. *Res. Chem. Intermediat.* 2007, *33*, 191.

108. Takagi, S.; Eguchi, M.; Shimada, T.; Hamatani, S.; Inoue, H. *Res. Chem. Intermediat.* 2007, *33*, 177.

109. Kawamata, J.; Suzuki, Y.; Tenma, Y. *Philosophical Magazine* 2010, *90*, 2519.

110. Ishida, Y.; Shimada, T.; Masui, D.; Tachibana, H.; Inoue, H.; Takagi, S. *J. Am. Chem. Soc.* 2011, *133*, 14280.

111. Takagi, S.; Aratake, Y.; Konno, S.; Masui, D.; Shimada, T.; Tachibana, H.; Inoue, H. *Microporous Mesoporous Mater.* 2011, *141*, 38.

112. Hagiwara, S.; Ishida, Y.; Masui, D.; Shimada, T.; Takagi, S. *Tetrahed. Lett.* 2012, *53*, 5800.

113. Ishida, Y.; Masui, D.; Shimada, T.; Tachibana, H.; Inoue, H.; Takagi, S. *J. Phys. Chem. C* 2012, *116*, 7879.

114. Takagi, S.; Shimada, T.; Ishida, Y.; Fujimura, T.; Masui, D.; Tachibana, H.; Eguchi, M.; Inoue, H. *Langmuir* 2013, *29*, 2108.

115. Deisenhofer, J.; Epp. O.; Sinning, I; Michel, H. *J. Mol. Biol.* **1995**, *246*, 429-457

116. Takagi, S.; Shimada, T.; Yui, T.; Inoue, H. *Chem. Lett.* **2001,** *30,* 128-129.

Chapter 2

Generation of the Monodispersed Gold Nano Particles on the Clay Surfaces with Deposition Reduction Method

2.1. Introduction

For constructing assembled structure of organic dyes, we have been focusing on using synthetic clay (saponite) as novel host materials for functional dyes.[1-5] We reported that multivalent cationic dyes adsorb and assembled on saponite without aggregation. The formation of these novel un-aggregated dye assemblies on the clay surfaces is attributed to size matching of the distance between cationic site of the dyes and anionic site on the clay surfaces. We called this unique technique as Size matching effect or inter-charge distance matching effect as described in chapter 1. However, we have never tried to construct the assembly of inorganic nano particles, although we have tried constructing the molecular assembly of cationic organic dyes on the clay surfaces. In this chapter, we examined to construct the assemble structure of gold nano particles as an inorganic NPs on the clay surfaces. Since Haruta *et al*. reported the catalytic activity of NPs, a lot of methods have been studied for generating gold NPs on the supporting materials.[9-14] Deposition reduction (DR) method is one of the methods to deposit gold NPs on the supporting material surfaces.[15, 16] Although small size gold NPs (< 5 nm) can be obtained by this method, it is still difficult to control their homogeneity and suppress the aggregation of gold NPs perfectly. To realize the assembly of the gold NPs, the

suppression of aggregation and size control of the gold NPs is important. Protective reagents have been used for suppressing the aggregation of gold NPs.[17, 18] For example, by using thiol derivatives as a protective reagent, well arranged gold nano clusters without aggregation have been reported.[19-21] However, the use of protecting reagents is not favored for the application to catalytic reactions, since the gold surface was covered with protective reagents. Considering this point, gold NPs should better to be deposited on the supporting materials surfaces for immobilization of gold NPs. Thus, developing the technique to prepare the uniform gold NPs without protective reagents is important. Clay minerals are one of the attractive supporting materials for gold NPs, due to their flatness of the surface and the large surface area (c.a. 760 m^2 g^{-1}).[22-24] However, few reports on the preparation of gold NPs on the clay surface have been reported.[25-28] Especially, Montmorillonite is one of the interesting clay minerals as a supporting materials for the gold NPs. Montmorillonite should have alternately cationic charge and anionic charge as shown Figure 1.

Figure 1. Charge distribution image of Montmorillonite clay surface.

We expected that this alternately charge is effective to suppress aggregation, because that cationic gold precursor will adsorb with anionic site on the clay surface but didn't with cationic site. Thus this electric repulsion between cationic gold precursor and cationic site on the clay surface may suppress the excess growth of gold NPs. In the

present work, we examined the formation of the non-aggregated small gold NPs without any protecting reagent on the clay surface. Then Conventional mixing and mixing with stopped-flow mixer was adopted for sample preparation to reveal the influence of the homogeneity at the sample preparation.[29, 30]

2.2. Experimental Section

Materials

Montmorillonite clay (Kunipia P, $(Na_{0.67})^{+0.67}$ $[Si_{8.00}(Al_{3.33}Mg_{0.67})O_{20}$ $(OH)_4$ $]^{-0.67}$) that is one of the typical clay, was purchased from Kunimine Industries. The structural image is shown in Figure 2.

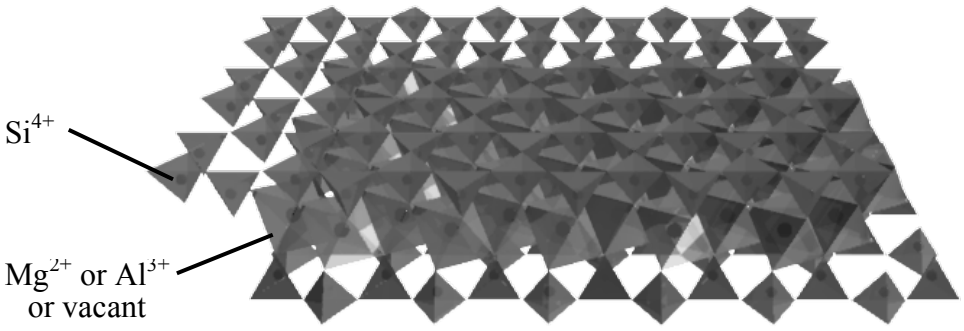

Figure 2. The structural image of clay: two silicon- and aluminum-centered tetrahedral layers and magnesium octahedral layer.

Since they possess regularly arranged anionic charges on its surface, cationic gold precursor could absorb on the clay surface. Gold precursor ($[Au(en)_2]Cl_3$, *en* =

ethylenediamine) was synthesized according to the literatures.[14, 31] 1 mL of anhydrous ethylenediamine (KANTO Chemical, > 99.0%) was added to diethyl ether (5 mL, KANTO Chemical, > 99.5%). The solution was added to diethyl ether (10 mL) containing hydrogen tetrachloroaurate(III) tetrahydrate ($HAu(III)Cl_4 \cdot 4H_2O$, 0.8 g, KANTO Chemical, > 99.0%). Yellow solid was precipitated and collected by a filtration (PTFE membrane filter, φ = 1.0 μm). Then, the obtained solid was dissolved in 2 mL water. By the repeated re-precipitation of the yellow solid with EtOH (15 mL, KANTO Chemical, > 99.5%), finally, the white solid was obtained. (yield = 33.0%) The purity was checked by TLC (Al_2O_3, saturated KNO_3 aq : H_2O : CH_3CN = 1 : 1 : 2) and 1 H-NMR (s, CH_2, 3.2 ppm in D_2O). NMR spectrum was obtained by JEOL EX-270 (270 MHz).

Deposition of Gold NPs on the Montmorillonite Surfaces

Gold NPs were prepared on the clay surface as follows. The sample preparation procedure is shown in Figure 3.

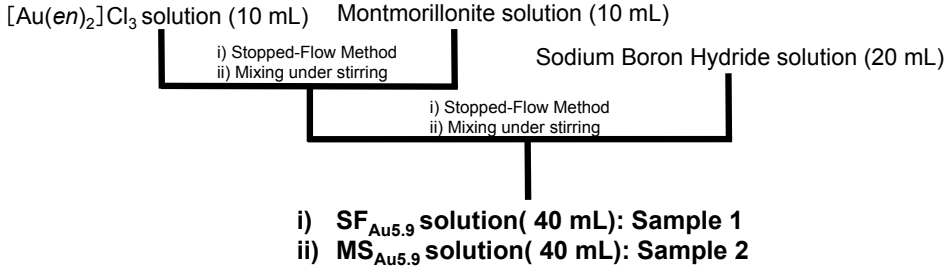

Figure 3. Flowchart of gold NPs preparation.

Montmorillonite aqueous solution (10 mL, 4.45 × 10^{-3} g L^{-1}) and gold precursor aqueous solution ($[Au(en)_2]Cl_3$, 10 mL, 1.3 × 10^{-6} M) were mixed by a stopped-flow mixer (Applied physics, RX.2000). The theoretical amount of gold precursor is 5.9 wt% corresponding to 100% vs. CEC (cation exchange capacity) of the clay. After 10 minutes standing, the solution and $NaBH_4$ aqueous solution (KANTO Chemical, > 92%, 6.7 × 10^{-5} M, 20 mL) were mixed with the stopped-flow mixer. By the reduction of gold precursor with $NaBH_4$, gold NPs (abbreviated as $SF_{Au5.9}$) would generate on the clay surface. The reference sample (abbreviated as $MS_{Au5.9}$) was obtained by using typical magnetic stirrer instead of stopped-flow mixer.

Sample Preparation for TEM Observation

The obtained solution (5.0 μL) was casted on the TEM grid (High Resolution Carbon Support Membrane, Okenshoji Co., Ltd.). The obtained grid was dried under vacuum, and then, was spattered with carbon for 4 sec. × 3 times (JEC-560, JEOL, at 4 A).

Preparation of the Gold NPs/Montmorillonite Thin Films

Gold NPs/Montmorillonite films were prepared to measure the absorption spectra of $MS_{Au5.9}$ and $SF_{Au5.9}$. The preparation method of the thin films was as follows. 100 mL of the dispersion of $MS_{Au5.9}$ and $SF_{Au5.9}$ was filtered through a PTFE membrane filter (pore size = 0.1 μm). The transparent thin film was obtained by transferring the residue

upon the glass substrate. The $MS_{Au5.9}$ and $SF_{Au5.9}$ thin films were dried up under vacuum over night.

Analysis

UV-Vis. absorption spectra were obtained on Shimadzu UV-3150. TEM samples were observed with TEM (JEM-2000FX, JEOL, at 200 kV). TG/DTA measurements were carried out with a Shimadzu DTG-60H analyzer to determine the water content of Montmorillonite.

2.3. Result and Discussion

Effect of the mixing method to deposit the gold nano particles on Montmorillonite surfaces

Typical TEM images and the size distribution of gold NPs of $SF_{Au5.9}$ and $MS_{Au5.9}$ were shown in Figure 4-i), ii). By analyzing eight TEM images, the size distribution of gold NPs of gold NPs of $SF_{Au5.9}$ and $MS_{Au5.9}$ was obtained as shown in Figure 4-iii), iv).

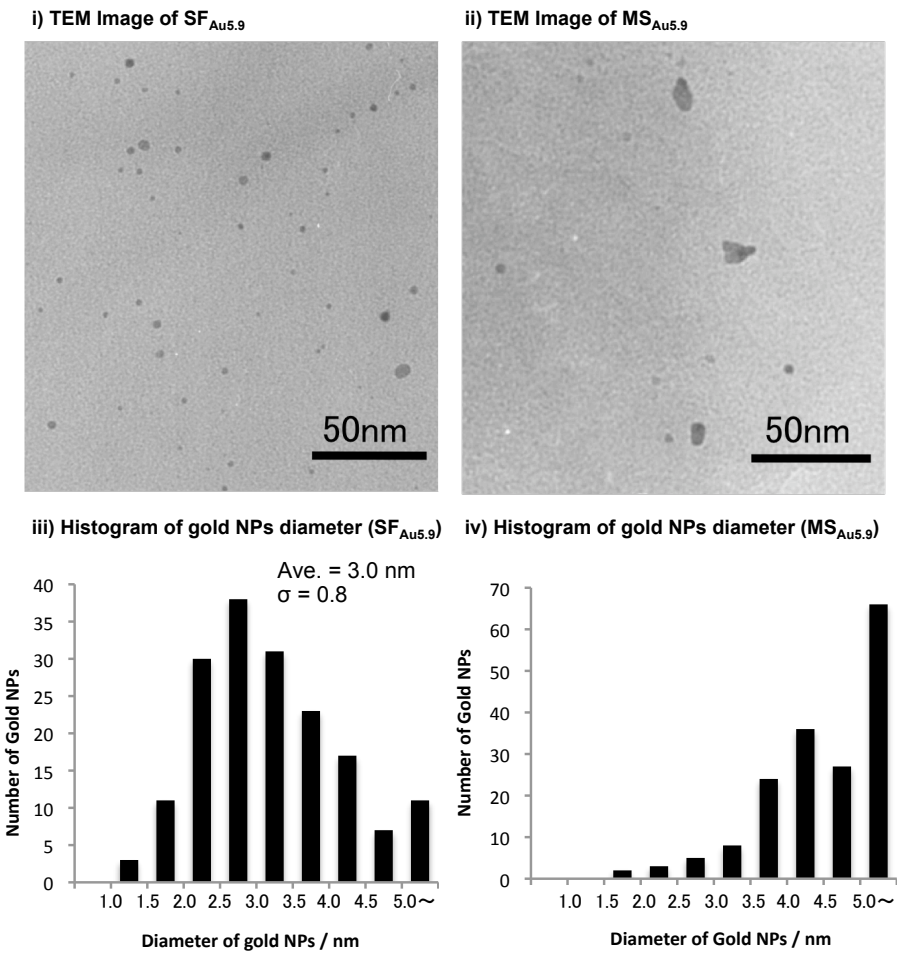

Figure 4. i) TEM image of gold NPs on the clay surface ($SF_{Au5.9}$), ii) TEM image of gold NPs on the clay surface ($MS_{Au5.9}$), iii) histogram for the size of gold NPs of $SF_{Au5.9}$, iv) histogram for the size of gold NPs of $MS_{Au5.9}$.

In the case of $SF_{Au5.9}$ (Figure 4-i), the particle size was apparently small and the shape of the gold NPs looked circle, compared to $MS_{Au5.9}$. On the other hand, the generated gold NPs aggregated and formed large particles in the case of $MS_{Au5.9}$ (Figure 4-ii). It is apparent that the sample preparation procedure strongly affected the gold NPs formation. The photographs of the gold NPs/Montmorillonite thin films were shown in Figure 5.

i) ii)

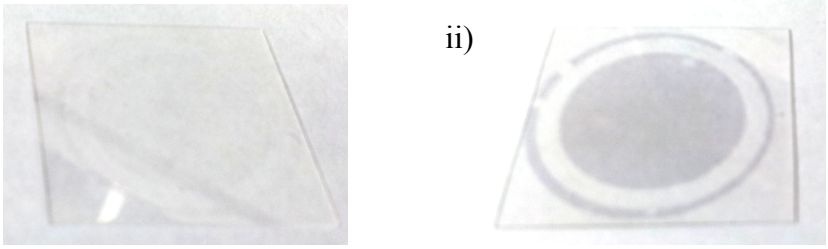

Figure 5. Photographs of gold NPs/Montmorillonite thin films

i) composed of $SF_{Au5.9}$, ii) composed of $MS_{Au5.9}$.

As can be seen in Figure 5, the obtained films were semi-transparent in the visible region, and this transparency is enough to measure the absorption spectra. In addition, the color of the film composed of $MS_{Au5.9}$ (Figure 5-ii) is bruise blue, which is the typical color of the gold NPs. The absorption spectra of these semi-transparent films are shown in Figure 6. It is known that a plasmon band at 550−600 nm should be observed for the gold NPs, when the particle size is larger than c.a. 5 nm.[32-34] In UV-vis. absorption spectrum, the absorption was not observed at 550−600 nm for $SF_{Au5.9}$ sample. On the other hand, in the case of $MS_{Au5.9}$ sample, the absorption was clearly observed at 550−600 nm. The ratio of particle whose diameter is larger than 5 nm is around 6% for $SF_{Au5.9}$. Some of them are the conjugated particles and are not sphere shape. Since the ratio is rather small and the peak shape would be broad, the absorption around 500−700 nm due to its plasmon band was not detected for $SF_{Au5.9}$ in Figure 6.

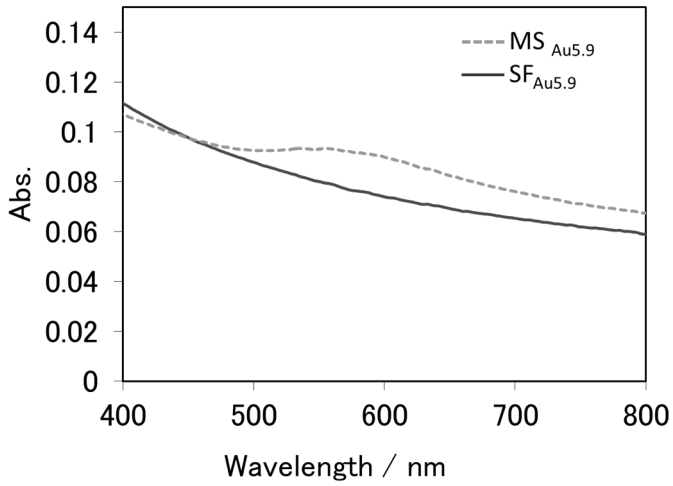

Figure 6. Absorption spectra of the film prepared with $SF_{Au5.9}$ (solid line) and $MS_{Au5.9}$ (broken line)

These observations proof that few large particles (> 5 nm) formed in the case of $SF_{Au5.9}$. The number of gold atom included in the obtained clay - gold NPs hybrids was calculated from TEM images for $SF_{Au5.9}$ and $MS_{Au5.9}$. Eight TEM images (300 nm × 300 nm) observed at different positions were used for reducing the deviation of observation area. The surface area of the clay and volume of gold NPs deposited on the clay surfaces were calculated from the eight TEM images. We estimated the gold atom number under the followings assumptions. i) When the shape of gold NP looks circle in TEM image, the actual shape is hemisphere. ii) When the shape of gold NP looks ellipsoid, the short axis length of the particle is the particle's height. iii) The crystal architecture of gold NP is face-centered cubic lattice. In the case of $SF_{Au5.9}$, the total atom number of gold was estimated to be 3.37×10^{-19} mol and the total surface area of clay was 8.88×10^{5} nm^2 , in the eight TEM images. Calculating from the loading

amount of clay for the complex preparation, the total surface area of clay in the whole system is 3.38×10^{16} nm^2 (760 $m^2\ g^{-1}$ $\times$ 4.45×10^{-3} $g\ L^{-1}$ $\times$ 10 mL). Thus, the total atom number of generated gold in the whole system is estimated to be 1.28×10^{-8} mol (3.38×10^{16} /(8.88×10^{5}) $\times$ 3.37×10^{-19}) for $SF_{Au5.9}$. The actual loading amount of gold precursor is 1.3×10^{-8} mol (1.3×10^{-6} M $\times$ 10 mL) in the present condition. Like this, the observed number of gold atom for $SF_{Au5.9}$ (1.28×10^{-8} mol) is almost equivalent to the actual loading one (1.3×10^{-8} mol). This indicates that the gold NPs generate uniformly in the case of $SF_{Au5.9}$. In a similar way, the total atom number of generated gold in the whole system is calculated to be 8.03×10^{-9} mol for $MS_{Au5.9}$. This indicates that the deviation of gold NPs generation is relatively large in the case of $SF_{Au5.9}$.

The effect of stopped flow mixer as a mixing method should be discussed. In the case of mixing by the use of stopped flow mixer (SF), two components can be mixed within msec. order. On the other hand, a few sec. is necessary for MS. This indicates that the uniform mixing condition can be achieved more rapidly in the case of SF, compared to MS. In other words, the uneven condition continues for long time and would lead to the generation of large size Au particles for MS. In particular, many Au seed particles would produce on the particular clay sheet, and there is few Au seed particle on the other clay sheet, in the case of MS. It leads to high density generation of Au seed particle on the particular clay sheet and would enhance the probability of aggregation of the particles on the clay surface. Although the relationship between the particle generation rate and mixing procedure rate is important, a rapid and uniform mixing

method such as SF would be better for the uniform generation of Au particles in general.

Effect of the concentration of gold precursor to deposit the gold nano particles on the Montmorillonite surfaces

The effect of gold precursor concentration on the NPs generation behavior was examined. The concentration of gold precursor was increased to 10.3 wt% (175% vs. CEC). The observed TEM images for $SF_{Au10.3}$ and $MS_{Au10.3}$ are shown in Figure 7. As shown in Figure 7, in the case of $SF_{Au10.3}$, we succeeded to deposit small gold NPs on the clay surfaces with high density even when the concentration of gold precursor was increased. The average diameter retains enough small for $SF_{Au10.3}$, as can be seen in Figure 7-iii). On the other hand, the gold NPs prepared by magnetic stirrer mixing ($MS_{Au10.3}$) grew much larger than that prepared by $SF_{Au10.3}$.

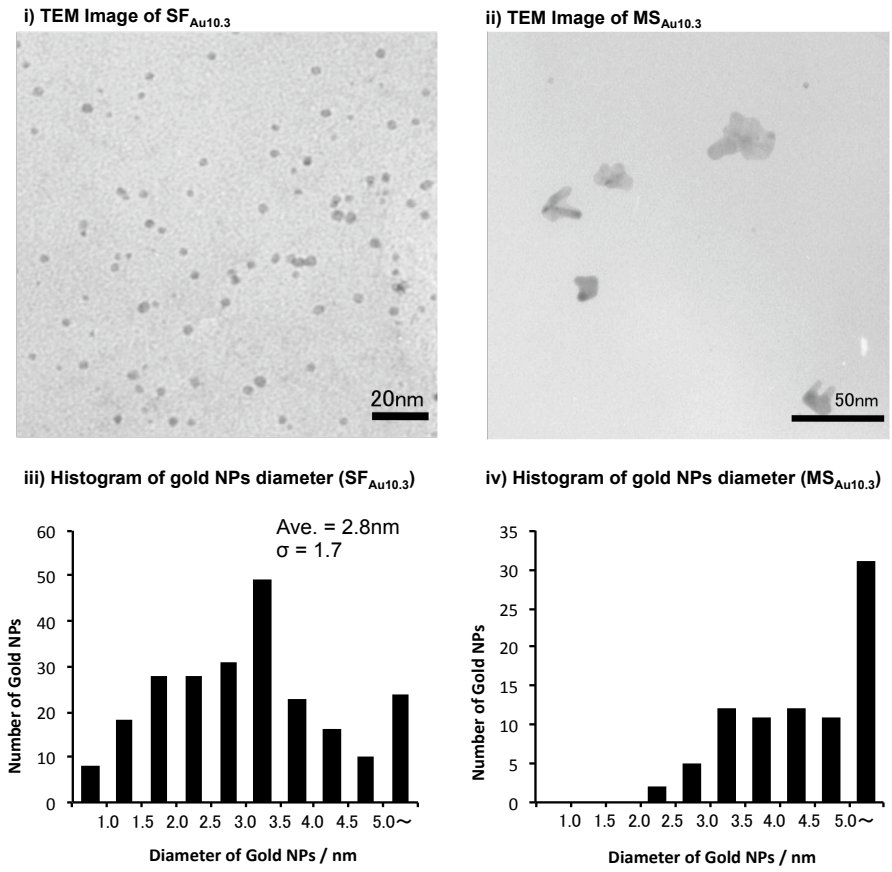

Figure 7. i) TEM image of gold NPs on the clay surface ($SF_{Au10.3}$), ii) TEM image of gold NPs on the clay surface ($MS_{Au10.3}$), iii) histogram for the size of gold NPs of $SF_{Au10.3}$, iv) histogram for the size of gold NPs of $MS_{Au10.3}$.

Stability of the gold nano particles deposited on the Montmorillonite surfaces

To discuss the stability of the gold nano particles deposited on Montmorillonite surfaces, the dispersion of $SF_{5.9}$ was heated at 90℃ between 9 hours. The dispersion was casted on TEM grid, and dried under vacuum condition over night. The TEM image of the gold nano particles which was heated till 90℃ during 9 hours was shown in Figure 8.

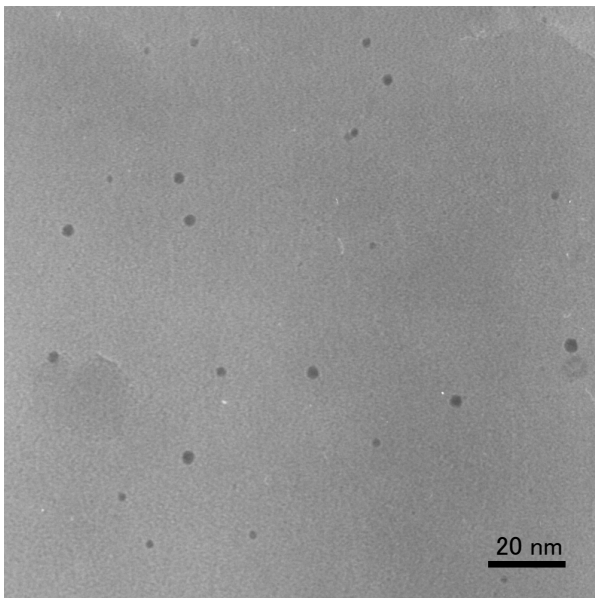

Figure 8. TEM image of $SF_{5.9}$ heated at 90℃ between 9 hours.

The gold nano particles on Montmorillonite surfaces were still kept their particle size. It suggested that deposited gold nano particles on the Montmorillonite surfaces was stable until 90℃. It indicated that these deposited gold nano particles on Montmorillonite surfaces may possible to function as the catalysis. However, it was difficult to deposit the gold nano particles on the Montmorillonite surfaces with high density without aggregation of gold nano particles. In $SF_{10.3}$, small amount of aggregated gold nano particles was observed. Furthermore, the standard deviation of gold nano particles' diameter in $SF_{10.3}$ was larger than the standard deviation of $SF_{5.9}$. It indicated that the size control of the gold nano particles was difficult when the loading level of the gold precursor was increased. In fact, when the concentration of gold precursor was increased more than 500 wt% (175% vs. CEC), we observed strong plasmon band, and large gold nano particles were observed in TEM observation. Thus

we consider that we have to develop the new strategy to deposit the gold nano particles on Montmorillonite surfaces with high density without aggregation toward the construction of the gold nano particles assembly on the Montmorillonite surfaces.

2.4. Conclusion

The gold NPs formation was successfully achieved on the clay surface. We succeeded to generate uniformly dispersed small gold NPs without aggregation on the clay surface by the use of stopped flow mixer, although gold NPs prepared by the typical mixing method using magnetic stirrer were aggregated. The uniform formation of the particle was confirmed by the analysis of TEM images. Even when the amount of gold was increased, the uniform dispersion of gold NPs was almost kept. It should be noted that any protecting reagent was not used in the present system.

2.5. References

1. Bujdák, J. Effect of the layer charge of clay minerals on optical properties of organic dyes. A review. *Appl. Clay Sci.* **2006,** *34*, 58-73.

2. Shichi, T.; Takagi, K. Clay minerals as photochemical reaction fields. *Journal of Photochemistry and Photobiology C: Photochem. Rev.* **2000,** *1*, 113-130.

3. Ishida, Y.; Kulasekharan, R.; Shimada, T.; Takagi, S.; Ramamurthy, V. Efficient singlet-singlet energy transfer in a novel host-guest assembly composed of an organic cavitand, aromatic molecules, and a clay nanosheet. *Langmuir* **2013,** *29*, 1748-53.

4. Eguchi, M.; Takagi, S.; Tachibana, H.; Inoue, H. The 'size matching rule' in di-, tri-, and tetra-cationic charged porphyrin/synthetic clay complexes: effect of the inter-charge distance and the number of charged sites. *J. Phys. Chem. Solids* **2004,** *65*, 403-407.

5. Takagi, S.; Tryk, D. A.; Inoue, H. Photochemical energy transfer of cationic porphyrin complexes on clay surface. *J. Phys. Chem. B* **2002,** *106*, 5455-5460.

6. Hagiwara, S.; Ishida, Y.; Masui, D.; Shimada, T.; Takagi, S. Unique photochemical behavior of novel tetracationic pyrene derivative on the clay surface. *Tetrahedron Lett.* **2012,** *53*, 5800-5802.

7. Takagi, S.; Shimada, T.; Ishida, Y.; Fujimura, T.; Masui, D.; Tachibana, H.; Eguchi, M.; Inoue, H. Size-matching effect on inorganic nanosheets: control of distance, alignment, and orientation of molecular adsorption as a bottom-up methodology for nanomaterials. *Langmuir* **2013,** *29*, 2108-19.

8. Egawa, T.; Watanabe, H.; Fujimura, T.; Ishida, Y.; Yamato, M.; Masui, D.; Shimada, T.; Tachibana, H.; Yoshida, H.; Inoue, H.; Takagi, S. Novel methodology to control the

adsorption structure of cationic porphyrins on the clay surface using the "size-matching rule". *Langmuir* **2011,** *27*, 10722-10729.

9. Haruta, M.; Yamada, N.; Kobayashi, T.; Iijima, S. Gold catalysts prepared by coprecipitation for low-temperature oxidation of hydrogen and of carbon monoxide. *J. Catal*. **1989**, *115,* 301-309.

10. Pina, D.C.; Falleta, E.; PRATI, L.; Rossi, M. Selective oxidation using gold. *Chem. Soc. Rev.* **2008**, *37*, 2077-2095.

11. Corma, A.; Garcia, H. Supported gold nanoparticles as catalysts for organic reactions. *Chem. Soc. Rev*. **2008**, *37*, 2096-2126.

12. Ishida, T.; Nagaoka, M.; Akita, T.; Haruta, M. Deposition of Gold Clusters on Porous Coordination Polymers by Solid Grinding and Their Catalytic Activity in Aerobic Oxidation of Alcohols. *Chem. A Eur. J.* **2008**, *14*, 8456-8460.

13. Turner, M.; Golovko, B.V.; Vaughan, P.H.O.; Abdulkin, P.; Berenguer-Murcia, A.; Tikhov, S.M.; Johnson, F.G.B.; Lambert, M.R. Selective oxidation with dioxygen by gold nanoparticle catalysts derived from 55-atom clusters. *Nature* **2008**, *454*, 981-983.

14. Ishida, T.; Kuroda, K.; Kinoshita, N.; Minagawa, W.; Haruta, M. Direct deposition of gold nanoparticles onto polymer beads and glucose oxidation with H_2O_2. *J. Colloid Interface Sci.* **2008**, *323*, 105-111.

15. Ishida, T.; Kinoshita, N.; Okatu, H.; Akita, T.; Takei, T.; Haruta, M. Influence of the Support and the Size of Gold Clusters on Catalytic Activity for Glucose Oxidation. *Angrew. Chem. Int. Ed.* **2008**, *47*, 9265-9268.

16. Sham, K.T.; Coulthard, I.; Lorimer, W.J.; Hiraya, A.; Watanabe, M. Reductive

Deposition of Cu on Porous Silicon from Aqueous Solutions: An X-ray Absorption Study at the Cu L3,2 Edge. *Chem. Mat*. **1994**, *6*, 2085-2091.

17. Levi-Kalisman, Y.; Jadzinsky, D.P.; Kalisman, N.; Tsunoyama, H.; Tsukuda, T.; Bushnell, A.D.; Kornberg, D.R. Synthesis and Characterization of Au_{102}(p-MBA)$_{44}$ Nanoparticles. *J. Am. Chem. Soc.* **2011**, *133*, 2976-2982.

18. Schmid, G. Large clusters and colloids. Metals in the embryonic state. *Chem. Rev.* **1992**, *92*, 1709-1727.

19. Shon, B.-H.; Choi, J.M.; Yoo, I.S.; Yun, S.H.; Zin, W.C.; Jung, C.J.; Kanehara, M.; Hirata, T.; Teranishi, T. Directed Self-Assembly of Two Kinds of Nanoparticles Utilizing Monolayer Films of Diblock Copolymer Micelles. *J. Am. Chem. Soc.* **2003**, *125*, 6368-6369.

20. Wilcoxon, P.J.; Provencio, P.P. Heterogeneous Growth of Metal Clusters from Solutions of Seed Nanoparticles. *J. Am. Chem. Soc.* **2004**, *126*, 6402-6408.

21. Shah, S.P.; Holmes, D.J.; Doty, C.R.; Johnston, P.K.; Korgel, A.B. Steric Stabilization of Nanocrystals in Supercritical CO_2 Using Fluorinated Ligands. *J. Am. Chem. Soc.,* **2000**, *122*, 4245-4246.

22. Ishida, Y.; Shimada, T.; Masui, D.; Tachibana, H.; Inoue, H.; Takagi, S. Efficient Excited Energy Transfer Reaction in Clay/Porphyrin Complex toward an Artificial Light-Harvesting System. *J. Am. Chem. Soc.* **2011**, *133*, 14280-14286.

23. Takagi, S.; Shimada, T.; Eguchi, M.; Yui, T.; Yoshida, H.; Tryk, A.D.; Inoue, H. High-Density Adsorption of Cationic Porphyrins on Clay Layer Surfaces without Aggregation: The Size-Matching Effect. *Langmuir* **2002**, *18*, 2265-2272.

24. Pentrák, M.; Czímerová, A.; Madejová, J.; Komadel, P. Changes in layer charge of clay minerals upon acid treatment as obtained from their interactions with methylene blue. *Appl. Clay Sci.* **2012**, *55*, 100-107.

25. Zhu, L.; Letaief, S.; Liu, Y.; Gervais, F.; Detellier, C. Clay mineral-supported gold nanoparticles. *Appl. Clay Sci.* **2009**, *43*, 439-446.

26. Suraja, P.V.; Binitha, N.N.; Yaakob, Z.; Silija, P.P. Preparation and Characterization of Nano Gold Supported over Montmorillonite Clays. *IOP Conf. Ser.: Mat. Sci. Eng.* **2011**, *17*, 012019/1-012019/4.

27. Belova, V.; Andreeva, D.V.; Mohwald, H.; Shchukin, D.G. Ultrasonic Intercalation of Gold Nanoparticles into a Clay Matrix in the Presence of Surface-Active Materials. Part II: Negative Sodium Dodecylsulfate and Positive Cetyltrimethylammonium Bromide. *J. Phys. Chem. C* **2009**, *113*, 6751-6760.

28. Patel, H.A.; Bajaj, H.C.; Jasra, R.V. Synthesis of Highly Dispersed Gold and Silver Nanoparticles Anchored on Surfactant Intercalated Montmorillonite. *J. Nanosci. Nanotech.* **2009**, *9*, 5946-5952.

29. Chen, Y.; Erickson, H.P. Conformational Changes of FtsZ Reported by Tryptophan Mutants. *Biochem.* **2011**, *50*, 4675-4684.

30. Sonchal, P.; Bhagwat, S.S. Droplet Exchange Kinetics in Microemulsions. *J. Disp. Sci. Tech.,* **2011**, *32,* 1404-1407.

31. Block, P.B.; Bailar, Jr.C.J. The Reaction of Gold(III) with Some Bidentate Coordinating Groups. *J. Am. Chem. Soc.* **1951**, *73*, 4722-4725.

32. Sönnichsen, C.; Geier, S.; Hecker, E.N.; Plessen, Von G.; Feldmann, J.; Ditlbacher,

H.; Lamprecht, B.; Krenn, R.J.; Aussenegg, R.F.; Chan, Z.-H.V.; Spatz, P.J.; Möller, M. Spectroscopy of single metallic nanoparticles using total internal reflection microscopy. *Appl. Phys. Lett.,* **2000**, *77*, 2949-2951.

33. Itoh, T.; Asahi, T.; Masuhara, H. Femtosecond light scattering spectroscopy of single gold nanoparticles. *Appl. Phys. Lett.,* **2001**, *79*, 1667-1669.

34. Hostetler, M. J.; Wingate, J. E.; Zhong, C.-J.; Harris, J. E.; Vachet, R. W.; Clark, M. R.; Londono, J. D.; Green, S. J.; Stokes, J. J.; Wignall, G. D.; Glish, G. L.; Porter, M. D.; Evans, N. D.; Murray, R. W. Alkanethiolate Gold Cluster Molecules with Core Diameters from 1.5 to 5.2 nm: Core and Monolayer Properties as a Function of Core Size. *Langmuir* **1998**, *14*, 17-30.

Chapter 3

Generation of Small and Non-Aggregated Gold Nano-Particles on the Clay Surface Modified with Porphyrin Molecules

3.1. Introduction

In chapter 2, we demonstrate the deposition of gold nano particles (NPs) on Montmorillonite (MNT) surfaces with chemical reaction toward arranging of gold NPs on MNT surfaces. Then it suggested that stopped flow mixing method is effective to deposit the dispersed gold NPs on the MNT surfaces. However, small amount of the gold NPs were aggregated, and the aggregated gold nano particles were increased when loading level of the gold precursor was increased. Thus it is difficult to arrange the gold NPs on the MNT surfaces by the method which was used in chapter 2, thus we have to develop a new strategy for the arrangement of the gold nano-particles on MNT surfaces. Some researchers have demonstrated the deposition at the surfaces of functionalized supporting materials.[1-6] As described in general introduction, we have investigated that porphyrin molecules were adsorbed on the clay surfaces with high density without aggregation even at high dye loadings.[7-12] We expected that this complex would be suitable as the supporting material of the gold nano particles, because the surfaces of exfoliated clay nano-sheets were modified with regularly arranged porphyrin molecules. Porphyrin molecule adsorbed on the clay surfaces would suppress the aggregation of the gold nano particles, because of the steric effect of porphyrin as shown Figure 1.

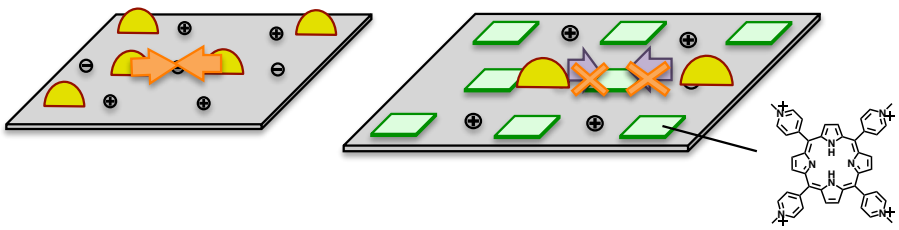

Figure 1. Image of the suppression of the aggregation of gold nano particles by the steric effect of porphyrin molecules on MNT surfaces

In this study, the deposition of small and uniform gold nano cluster was examined by using clay minerals as supporting material where the surface was modified with regularly arranged porphyrin molecules. The stopped flow mixing method was adopted for the all sample preparation.

3.2. Experimental section

Materials

Tetrakis(1-methyl-4-pyridiniumyl)porphyrin (abbreviated as TMPyP) was used as guest molecules for MNT. TMPyP was purchased from Frontier scientific. The counter ion (tosylate anion) was exchanged with chloride by use of an ion exchange column (ORGANOAMBERLITEIRA400JCL). Montmorillonite clay (Kunipia P, $(Na_{0.67})^{+0.67}$ $[Si_{8.00}(Al_{3.33}Mg_{0.67})O_{20}(OH)_4]^{-0.67}$) was purchased from Kunimine Industries. The surface area is 760 $m^2\ g^{-1}$ and the cation exchangeable capacity (CEC) is 9.0×10^{-4} eq g^{-1}. Gold precursor ($[Au(en)_2]Cl_3$, *en* = ethylenediamine) was synthesized according to the literatures[ref]. The structural image of TMPyP and MNT were shown in

Figure 2.

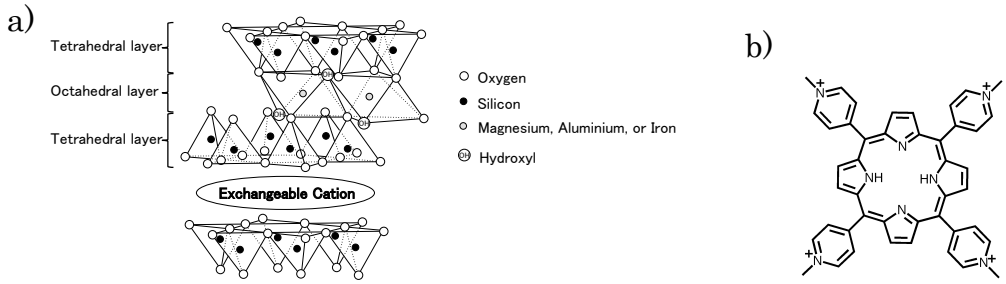

Figure 2. Structural image of (a) Montmorillonite (MNT), and

(b) tetrakis(1-methyl-4-pyridiniumyl)porphyrin (TMPyP)

Deposition of Gold NPs on MNT Surface Via Chemical Reduction Method

Gold NPs were prepared on the clay surface as follows. The mixed solution (10 mL) of the gold precursor (1.1×10^{-6} M) and TMPyP (5.0×10^{-7} M) was mixed with Montmorillonite aqueous solution (10 mL, 4.4×10^{-3} g L^{-1}) by a stopped-flow mixer (Applied physics, RX.2000). The theoretical amount of gold precursor is 5.0 wt% corresponding to 85 % versus CEC of the Montmorillonite, and the loading level of TMPyP is 50% versus CEC. Concentration of the TMPyP and gold precursor was changed to control the loading level of the TMPyP and gold precursor. Gold precursor and porphyrin molecules would adsorb on the MNT surfaces with electrostatic interaction. After 10 minutes standing, the solution and $NaBH_4$ aqueous solution (KANTO Chemical, > 92 %, 5.7×10^{-5} M, 20 mL) were mixed with a stopped-flow mixer. By the reduction of gold precursor with $NaBH_4$, gold NPs (abbreviated as $SF_{Au5.9}$) would generate on the clay surfaces.

TEM Observation of Gold NPs Deposited on MNT Surfaces

For an observation of transmission electron microscopy (TEM), the obtained dispersion was casted on the TEM grid (High Resolution Carbon Support Membrane, Okenshoji Co., Ltd.). The grid was dried under vacuum over night, then it was spattered with carbon for 4 sec × 3 times (JEC-560, JEOL, at 4 A). These samples were observed with a TEM (JEM-2000FX, JEOL, at 200kV).

3.3. Results and discussion

Generation of the gold nano particles on the MNT surface modified with co-adsorbed TMPyP

The obtained TEM image was shown in Figure 3-(a), and the histogram of the gold nano particles diameter was shown in Figure 3-(b).

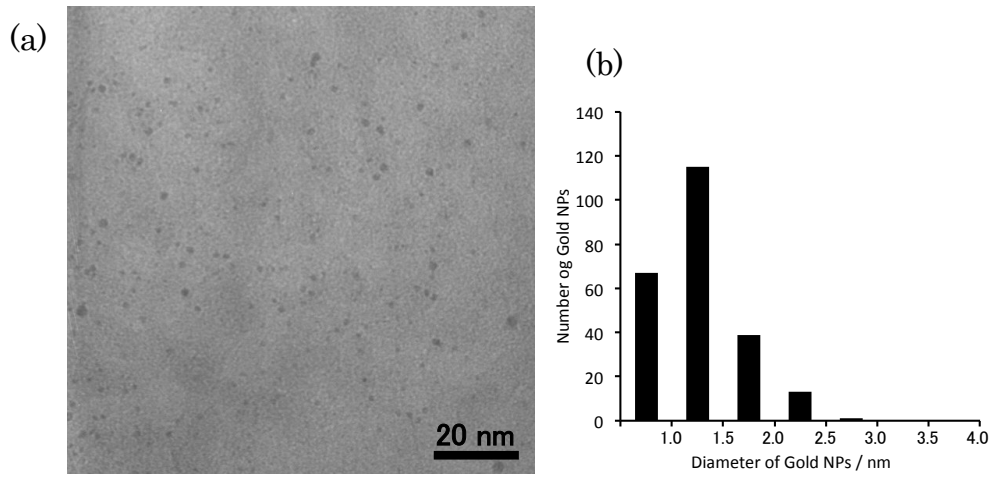

Figure 3. (a) TEM image of the gold nano particles on the MNT surfaces, (b) histogram of the gold nano particles' diameter

As shown in Figure 3-(a) small gold nano particles on the MNT surfaces were observed These gold nano particles were clearly small compared to the gold nano particles generated on the MNT surfaces without modification by porphyrin molecules, which was shown in chapter 2. The average diameter of the gold nano particles on MNT surfaces modified with TMPyP was 1.3 nm, and standard deviation is 0.4 nm. On the other hand, average diameter of gold nano particles deposited on MNT surfaces without TMPyP was 3.0 nm, and standard deviation was 0.8 nm. It indicates that gold nano particles deposited on the MNT surfaces modified with TMPyP was smaller and the particle size of them were arranged compared to the gold nano particles deposited on the MNT without TMPyP judging from the average diameter of the gold NPs and the standard deviation of them. In addition, the aggregated gold nano particles were not observed on MNT modified with TMPyP. It suggested that aggregation of the gold nano particles may be suppressed by the TMPyP adsorbed on the MNT surfaces.

Effect of the loading level of TMPyP on MNT surfaces

To examine the effect of the adsorption density of TMPyP, loading level of TMPyP was changed to 100% versus cation exchange capacity of MNT. The TEM image of the gold nano particles on MNT surfaces modified with TMPyP, which the loading level of TMPyP was changed from 0% to 100% versus cation exchange capacity was shown in Figure 4.

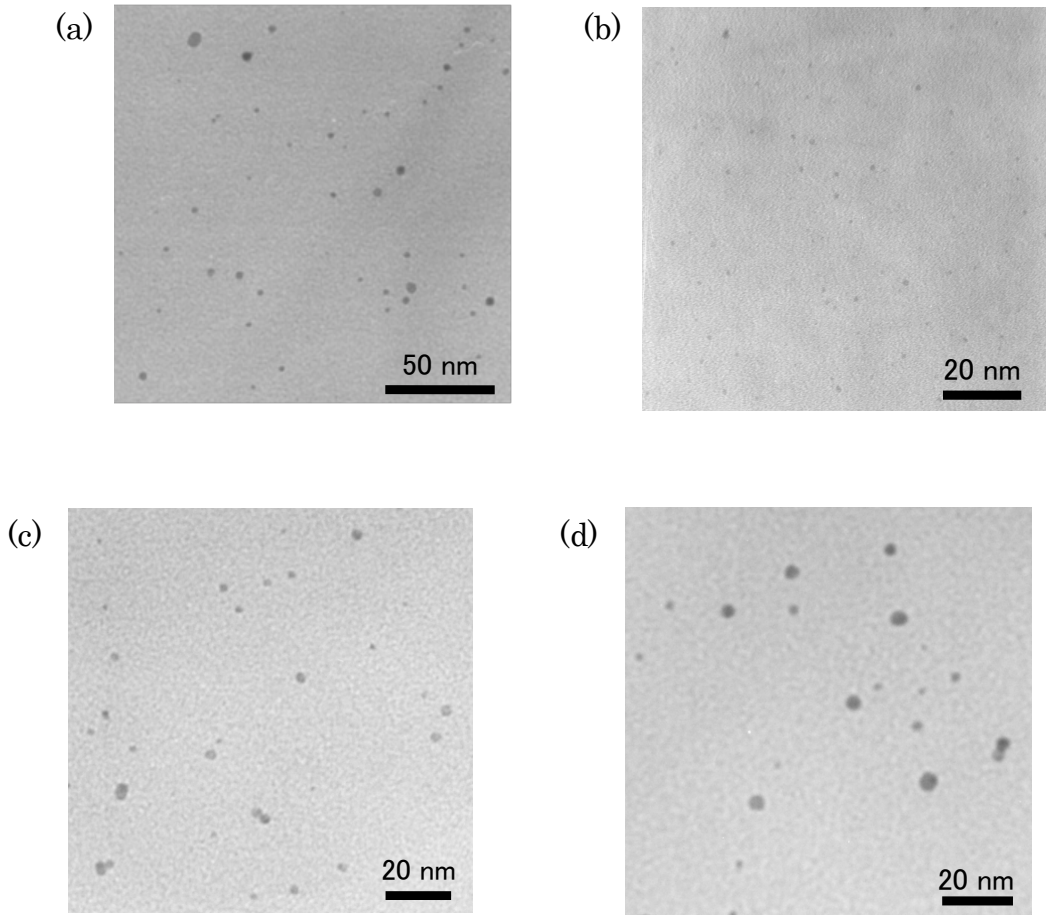

Figure 4. TEM image of gold nano particles deposited on MNT surfaces modified with TMPyP (a) loading level of TMPyP was set at 0% versus CEC, (b) loading level of TMPyP was set at 50% versus CEC, (c) loading level of TMPyP was set at 75% versus CEC, (d) loading level of TMPyP was set at 100% versus CEC

The loading level of TMPyP was set at 0, 50, 75, 100% versus CEC of the MNT in Figure 4-(a), (b), (c) and (d), respectively, and loading level of the gold precursor was unified as 100% versus CEC of MNT. As shown in Figure 4-(a) and (b), the particle size of the gold nano particles was smaller in presence of the TMPyP compared to absence of TMPyP. However, as shown in Figure 4-(c) and (d), the particle size was

large compared to Figure 4-(b). Especially in Figure 4-(d), the particle size was larger compared to Figure 4-(b) and (c), and theaggregated gold nano particles were observed during TEM observation. Considering the surface area of MNT and TMPyP, when the loading level of TMPyP was set at 50, 75, 100% versus CEC, the covered surface area of MNT by TMPyP corresponds to 13%, 19%, 25%, respectively. Thus there is enough surfaces area, that was not covered by TMPyP, to deposit gold nano particles. However, the generated gold nano particles were large and aggregated. By this chemical deposition method, the gold precursor was adsorbed on the supporting materials, and reductant was reduced the gold precursor and gold nano particle would be generated on the supporting materials surfaces. Considering this expected mechanism, adsorption of the gold precursor would be important because if there is gold precursor in solution, gold precursor will be reduced in solution. This reduced gold precursor in solution would form the gold nano particles proceed the excess grown up of gold nano particles deposited on the supporting materials' surfaces, and it will avoid the uniform generation of gold nano particles on the supporting materials surfaces. In the case of Figure 4-(c) and (d), 75% or 100% the adsorption site of the gold precursor was occupied with TMPyP. Thus gold nano particles deposited on the MNT surfaces was grown up with the excess Au(0), which was reduced in water.

Thermal Stability of gold nano particles deposited on the MNT surfaces modified with TMPyP

To examine the thermal stability of the gold nano particles deposited on MNT surfaces modified with TMPyP, the dispersion of MNT where the gold nano particles was deposited was heated at 90℃ between 9 hours. If TMPyP adsorbed on MNT surfaces was modified the surfaces, the aggregation of the gold nano particles would be suppressed. The obtained gold nano particles were shown in Figure 5.

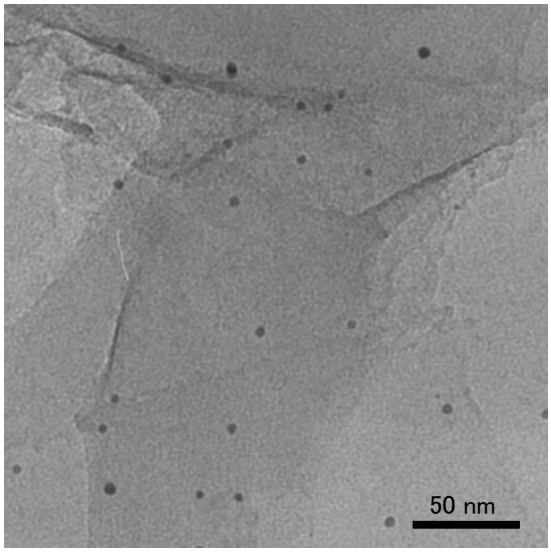

Figure 5. TEM image of gold nano particles heated at 90℃ between 9 hours in presence of TMPyP.

The observed gold nano particles were large, and small gold nano particles were disappeared although gold NPs deposited on MNT without TMPyP was stable as shown in chapter 2. It suggested that small gold nano particles were aggregated each other, and

it came to large gold nano particles. The melting point of the solids depends on the particle size, and melting point of the nano particles is lower than bulk materials.[18] It indicated that gold nano particles were melted and aggregated each other. However, melting point of the gold nano particles whose diameter is 1.5 nm was calculated as 277℃ with molecular dynamics calculation.[19] Gold nano particles on MNT surfaces were aggregated in spite of the absence/presence of TMPyP. It would be suggested that TMPyP adsorbed on MNT surfaces was moved with increasing of the temperature, they couldn't suppress the aggregation of the gold nano particles. In fact, the structures of the molecules adsorbed on the clay surfaces have been changed by temperature. It indicated that molecules adsorbed on clay surfaces can move, thus aggregation of the nano particles cannot be suppressed. In addition, the surfaces of the clay does not have unsaturated bond. It expected that interaction between gold nano particles and clay surfaces is week, and gold nano particles couldn't be immobilized strongly on clay surfaces. Also this week interaction between gold nano particles and MNT surfaces would be the cause of the instability against the thermal. However, these gold nano particles were stable during the TEM observations and room temperature, thus this instability makes small difference to construct the assembly structure of the gold nano particles.

Effect of the loading level of gold precursor and estimation of the appropriate gold precursor amount

As described above, small gold nano particles could be deposited on MNT surfaces modified with TMPyP. However, to construct the gold nano particles assembly with high density without aggregation, such as assembly of porphyrin molecules on the clay surfaces, large number of gold nano particle have to be generated on the MNT surfaces. Considering the ideal particle size (1.3 nm), ideal density of the gold nano particles (occupied surface area of gold nano particles (5.0 nm^2), and surface area of MNT (760 mg^{-1}), required gold precursor was ca. 2300 % versus CEC at least, thus increasing of gold precursor requires to construct the gold NPs assembly on MNT surfaces. As described in chapter 2, the large gold nano particles can be recognized from the absorption spectra, because large gold nano particles has absorption band ascribed to the plasmon.[20-22] The absorption spectra of the gold nano particles deposited with this method were shown in Figure 6, and loading level of the gold precursor was set at 100, 200, 300, 500, 1000, 3000% versus CEC. The concentration of the reducing agent was set at 20 times of gold precursor, and the loading level of the TMPyP was set at 50% versus CEC of the MNT. The differential spectra ((each spectra) – (absorption spectra of TMPyP on MNT surfaces)) were shown in Figure 7.

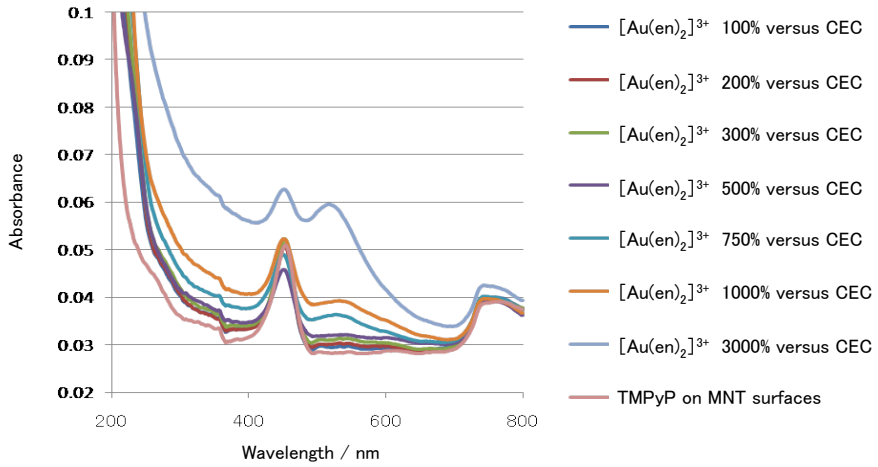

Figure 6. Absorption spectra of gold nano particles at various loading level of gold precursor

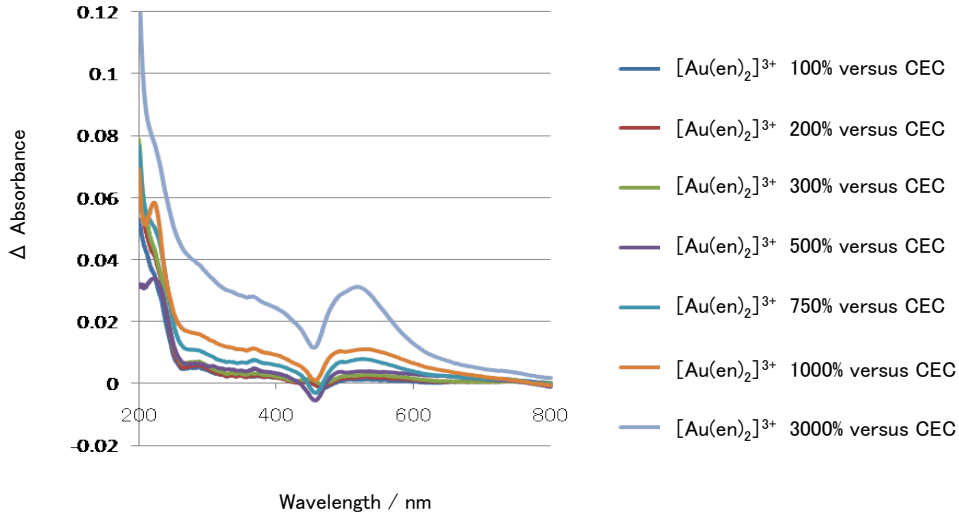

Figure 7. Differential spectra of the Figure 6.

((Each absorption spectra) – (absorption spectra of TMPyP adsorbed on MNT surfaces))

When the loading levels of the gold precursor were 100, 200, 300% versus CEC, the absorption band ascribed to plasmon was not observed. It suggested that gold nano particles whose diameter was smaller than ca. 5 nm were deposited. On the other hand,

the plasmon band were observed when loading level of the gold precursor was set at more than 500% versus CEC. The absorbance of the plasmon band was increased with increasing of the loading level of gold precursor. It indicated that gold nano particles whose diameter was larger than 5 nm were increased. The breaching of the absorption band of TMPyP on MNT surfaces (ca. 450 nm) was observed in every loading level. This breaching was also observed when reducing reagent solution was added to the dispersion of the TMPyP/MNT complex. Considering the redox potential of reducing reagent and TMPyP, electron transfer from reducing reagent to TMPyP is exergonic reaction, thus TMPyP would be reduced by the reducing reagent. The breaching of the TMPyP is noticeable when gold precursor loading level was set at high compared to the low loading level of gold precursor. It is because that the concentration of reducing reagent was high when the loading level of the gold precursor was set at high as described above. This breaching was recovered with the time. It suggested that TMPyP reduced spices was oxidized. The TEM image of the gold nano particles, when the loading level of gold precursor was set at 300% versus CEC of MNT was shown in Figure 8.

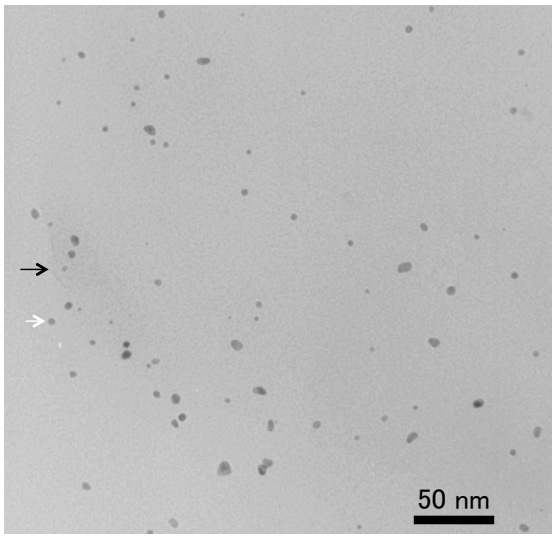

Figure 8. The deposited gold nano particles when loading level of the gold precursor was set and 300% versus CEC of MNT

Judging from absorption spectra, gold nano particles whose diameter is larger than ca. 5 nm wouldn't be observed. However, the generated gold nano particles were large and aggregated. Plasmon band depends on the shape and diameter of the NPs.[23] The obtained particle size and shape were not unified as shown in Figure 8. It would be the cause of the broadened plasmon band, and the plasmon band should be obfuscated. The edge of MNT could be observed at the point of black arrow in Figure 8, and almost gold nano particles were deposited on MNT surfaces. However, the gold nano particles, which were not deposited on MNT, were observed at the point of the white arrow in Figure 8. It suggested that the some of the gold nano particles were not generated on MNT surfaces, but generated in the water. We consider that excess gold precursor which could not adsorbed on MNT surfaces were reduced in water, and they form the gold nano particles which was not immobilized on MNT surfaces. This result indicates

that it is difficult to deposit the gold nano particles on MNT surfaces with high density without aggregation and to construct the assembly structure of gold nano particles on MNT surfaces by this method. To suppress the generation of gold nano particles in water and to deposit the small gold nano particles on MNT surfaces with high density without aggregation, following experiment was carried out. The loading level gold precursor and TMPyP was set at 100% versus CEC of MNT, and reducing reagent aqueous solution was added. After that, the MNT was corrected by centrifugation, then the precipitate was re-dispersed in water. 100% gold precursor was added to the solution, and reducing reagent aqueous solution was added. This procedure was repeated until total amount of the gold precursor came to 300% versus CEC of the MNT. TEM image of obtained gold nano particles was shown in Figure 9.

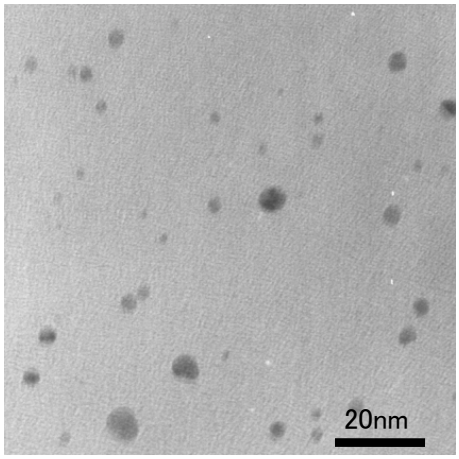

Figure 9. TEM image of the gold nano particles obtained by repetition reduction

The grown up gold nano particles were obtained. Considering the surface energy of the gold nano particles, formation of the large gold nano particle would be

thermodynamically stable compared to the formation of the lots of small gold nano particles when same number of Au atoms was used. The percentage of surface atom (surface atoms / total atoms of a nano particle ×100) of the small gold nano particles is larger than the large gold nano particles, and this superficial atom is unstable compared to the inner atom. Thus growth of the seed gold nano particles is thermodynamically favorable compared to the generation of new small gold nano particles.

3.4. Conclusion

In this chapter, gold nano particles were deposited on MNT surfaces. The surfaces of MNT were modified with cationic porphyrin to suppress the aggregation of gold nano particles. The size of generated gold nano cluster was small and uniform without aggregation. The average size of gold nano particles on the modified MNT surfaces was 1.3 nm, and standard deviation of that was 0.4 nm. The diameter of obtained gold nano particles were small compared to the gold nano particles on MNT surfaces in absence of cationic porphyrin whose average diameter and standard deviation was 3.0 and 0.8, respectively. However it is impossible to construct the assembly of gold nano particles on MNT surfaces with high density without aggregation.

3.5. References

1. Odrozek, K.; Maresz, K.; Koreniuk, A.; Prusik, K.; Mrowiec-Białoń, J. Amine-stabilized small gold nanoparticles supported on AlSBA-15 as effective catalysts for aerobic glucose oxidation. *Appl. Catal. A: General* **2014,** *475*, 203-210.

2. Rameshkumar, P.; Ramaraj, R. Gold nanoparticles deposited on amine functionalized silica sphere and its modified electrode for hydrogen peroxide sensing. *J.Appl. Electrochem.* **2013,** *43*, 1005-1010.

3. Anand, N.; Ramudu, P.; Reddy, K. H. P.; Rao, K. S. R.; Jagadeesh, B.; Babu, V. S. P.; Burri, D. R. Gold nanoparticles immobilized on lipoic acid functionalized SBA-15: Synthesis, characterization and catalytic applications. *Appl. Catal. A: General* **2013,** *454*, 119-126.

4. Boullanger, A.; Clément, S.; Mendez, V.; Daniele, S.; Thieuleux, C.; Mehdi, A. SH-functionalized cubic mesostructured silica as a support for small gold nanoparticles. *RSC Advances* **2013,** *3*, 725.

5. Wu, P.; Bai, P.; Lei, Z.; Loh, K. P.; Zhao, X. S. Gold nanoparticles supported on functionalized mesoporous silica for selective oxidation of cyclohexane. *Microporous and Mesoporous Mater.* **2011,** *141*, 222-230.

6. Ganai, A. K.; Bhardwaj, R.; Hotha, S.; Gupta, S. S.; Prasad, B. L. V. 'Clicking' molecular hooks on silica nanoparticles to immobilize catalytically important metal complexes: the case of gold catalyst immobilization. *New Journal of Chemistry* **2010,** *34*, 2662.

7. Egawa, T.; Watanabe, H.; Fujimura, T.; Ishida, Y.; Yamato, M.; Masui, D.; Shimada, T.; Tachibana, H.; Yoshida, H.; Inoue, H.; Takagi, S. Novel methodology to control the adsorption structure of cationic porphyrins on the clay surface using the "size-matching rule". *Langmuir* **2011,** *27*, 10722-9.

8. Hagiwara, S.; Ishida, Y.; Masui, D.; Shimada, T.; Takagi, S. Unique photochemical behavior of novel tetracationic pyrene derivative on the clay surface. *Tetrahedron Lett.* **2012,** *53*, 5800-5802.

9. Takagi, S.; Eguchi, M.; Tryk, D.; Inoue, H. Porphyrin photochemistry in inorganic/organic hybrid materials: Clays, layered semiconductors, nanotubes, and mesoporous materials. *Journal of Photochemistry and Photobiology C: Photochem. Rev.* **2006,** *7*, 104-126.

10. Eguchi, M.; Takagi, S.; Tachibana, H.; Inoue, H. The ‘size matching rule’ in di-, tri-, and tetra-cationic charged porphyrin/synthetic clay complexes: effect of the inter-charge distance and the number of charged sites. *J Physics Chem. Solids* **2004,** *65*, 403-407.

11. Takagi, S.; Shimada, T.; Ishida, Y.; Fujimura, T.; Masui, D.; Tachibana, H.; Eguchi, M.; Inoue, H. Size-matching effect on inorganic nanosheets: control of distance, alignment, and orientation of molecular adsorption as a bottom-up methodology for nanomaterials. *Langmuir* **2013,** *29*, 2108-19.

12. Takagi, S.; Shimada, T.; Eguchi, M.; Yui, T.; Yoshida, H.; Tryk, D. A.; Inoue, H. High-density adsorption of cationic porphyrins on clay layer surfaces without aggregation: The size-matching effect. *Langmuir* **2002,** *18*, 2265-2272.

13. Fujimura, T.; Misaki, Y.; Masui, D.; Shimada, T.; Takagi, S. Preparation of uniformly dispersed gold nano particles on the clay surface. *Clay sci.* **2012**, *16*, 121-125.

14. Ishida, T.; Kuroda, K.; Kinoshita, N.; Minagawa, W.; Haruta, M. Direct deposition of gold nanoparticles onto polymer beads and glucose oxidation with H_2O_2. *J. Colloid Interface Sci.* **2008**, *323*, 105-111.

15. Block, P.B.; Bailar, Jr.C.J. The Reaction of Gold(III) with Some Bidentate Coordinating Groups. *J. Am. Chem. Soc.* **1951**, *73*, 4722-4725.

16. Chen, Y.; Erickson, H.P. Conformational Changes of FtsZ Reported by Tryptophan Mutants. *Biochem.* **2011**, *50*, 4675-4684.

17. Sonchal, P.; Bhagwat, S.S. Droplet Exchange Kinetics in Microemulsions. *J. Disp. Sci. Tech.,* **2011**, *32,* 1404-1407.

18. Koumoto, K. Superfine Particle, Science and Application, General remarks for Science, *Che.l Soc. Jpn.,* **1985**, *48*, 47-51.

19. Cleveland, C.; Luedtke, W.; Landman, U. Melting of gold clusters. *Phys. Rev. B* **1999,** *60*, 5065-5077.

20. Sönnichsen, C.; Geier, S.; Hecker, E.N.; Plessen, Von G.; Feldmann, J.; Ditlbacher, H.; Lamprecht, B.; Krenn, R.J.; Aussenegg, R.F.; Chan, Z.-H.V.; Spatz, P.J.; Möller, M. Spectroscopy of single metallic nanoparticles using total internal reflection microscopy. *Appl. Phys. Lett.,* **2000**, *77*, 2949-2951.

21. Itoh, T.; Asahi, T.; Masuhara, H. Femtosecond light scattering spectroscopy of single gold nanoparticles. *Appl. Phys. Lett.,* **2001**, *79*, 1667-1669.

22. Hostetler, M. J.; Wingate, J. E.; Zhong, C.-J.; Harris, J. E.; Vachet, R. W.; Clark, M. R.; Londono, J. D.; Green, S. J.; Stokes, J. J.; Wignall, G. D.; Glish, G. L.; Porter, M. D.; Evans, N. D.; Murray, R. W. Alkanethiolate Gold Cluster Molecules with Core Diameters from 1.5 to 5.2 nm: Core and Monolayer Properties as a Function of Core Size. *Langmuir* **1998**, *14*, 17-30.

23. Eguchi, M.; Mitsui, D.; Wu, H. L.; Sato, R.; Teranishi, T. Simple reductant concentration-dependent shape control of polyhedral gold nanoparticles and their plasmonic properties. *Langmuir* **2012,** *28*, 9021-6.

Chapter 4

Formation of Assembled Structure of Gold Nano Clusters on the Clay Surface Utilizing Porphyrin/Clay Complex as a Template

4.1. Introduction

As can be seen in a light harvesting system in natural photosynthesis, controlling assembly structure of organic molecules is important to develop photo-functionalities.[1, 2] Organic molecule assemblies constructed without covalent bounds, such as micelles, metal-organic frameworks and other supra-molecules' assemblies, and the photo-functionalities of these assembled organic molecules have been studied in a several decades.[3-6] We have been examining artificial light harvesting systems by using porphyrin-clay complexes where porphyrin molecules are regularly arranged on the clay surface. [7, 8] Clay minerals, which is one of the aluminosilicate nano-sheets, are an attractive group of materials because of their properties, those are (1) flat surfaces at the atmic level, (2) regular negatively charged surfaces, (3) exfoliation or stack ability of individual nano-sheets depending on their medium, and (4) optical transparency in the visible region in the exfoliated state, when the particle size is small (ca. < 100 nm).[7, 9, 10] Through our previous works, we have developed novel techniques for the arrangement control of dyes assembly on the clay surface. We have successfully prepared unique clay/porphyrin complexes in which the porphyrin molecules adsorb on the clay surfaces

without aggregation even at high dye loadings. A formation of these unique hybrids was rationalized by a size-matching of inter cationic distances in the porphyrin molecules and average anionic distances on the clay surfaces. We named this effect as the "Size-matching rule" or "Inter-charge distance matching rule".

On the other hand, syntheses and self-assemblies of inorganic nano-particles (NPs) have attracted great research interests over the past decades because of their unique optical, electrical, and magnetic properties.[12-21] Especially, gold NPs have been studied actively because of their interesting behaviors such as unique catalytic activity.[22-24] Some researchers reported the synthetic approaches of very small gold NPs, which are called gold nano clusters, and the fabrication of well-ordered 2D or 3D superlattices of clusters.[25-28] These well-ordered gold clusters have been realized by using distinct protective reagents, which are typically thiol, amine derivatives or surfactants. Because these protective reagents cover the gold surfaces and influence the properties of gold clusters, the utilization of protecting reagents is not favored for the some further applications. There are some reports to synthesize gold NPs by photochemical reaction.[29-31] However, a precise control of gold NPs generation, from a view point of deposition density and aggregation control, was still a challenge to solve. We supposed that the functional dyes would be able to be used as photosensitizer to generate the gold NPs, and the structure of supramolecular assemblies of those dyes might be able to be used as template to control the structure of gold NPs assembly. In this report, our aim is to examine the porphyrin assembly structure on the clay surface

both as a template and sensitizer for generating gold NPs without distinct protective reagent.

4.2. Experimental section

Materials

Structural image of Montmorillonite clay (Kunipia P, $(Na_{0.67})^{+0.67}$ ［$Si_{8.00}(Al_{3.33}Mg_{0.67})O_{20}(OH)_4$］$^{-0.67}$, abbreviated as MNT) that is one of the typical clay minerals, was shown in Figure 1-(a). Theoretical surface area of MNT is 760 m^2 g^{-1} and the cation exchangeable capacity (CEC) of MNT is 9.0×10^{-4} eq g^{-1}. The average area per an anionic site is calculated to be 1.40 nm^2, and the average distance between anionic sites on the MNT sheets is estimated to be 1.27 nm on the basis of a hexagonal array. Tetrakis(1-methyl-4-pyridiniumyl)porphyrin (abbreviated as TMPyP) was used as guest molecules for MNT, and the structure of TMPyP was shown in Figure 1-(b). The average inter-molecular distance of porphyrin molecules on MNT surface is calculated to be 2.5 nm when the loading level of porphyrin is 100% versus cation exchange capacity (CEC) of the clay. Gold precursor ($[Au(en)_2]Cl_3$, *en* = ethylenediamine) was synthesized according to the literatures.[32] Triethylamine (abbreviated as TEA) was used just after distillation.

Deposition of Gold NPs on MNT surfaces via PTR method

3 mL aqueous dispersion containing ［Au(*en*)$_2$］Cl_3 (5.8×10^{-4} M), TEA (0.25 M), MNT (1.1×10^{-2} g L^{-1}) and TMPyP (2.0×10^{-6} M (80% versus CEC of the MNT)) was prepared to demonstrate TPR method. This transparent dispersion was degassed by N_2 bubbling over 30 minutes and was cooled to 5 ℃ in the closed quartz cell. The quartz cell was irradiated with monochromatic light (450 nm). The sample was monitored with UV-Vis absorption spectroscopy during the photochemical reaction (240 min). Quantum yield of this photochemical reaction at 120 minutes was calculated as 1.2×10^{-3} from the decrease of $[Au(en)_2]^{3+}$. Generated gold NPs were observed with transmission electron microscope (TEM).

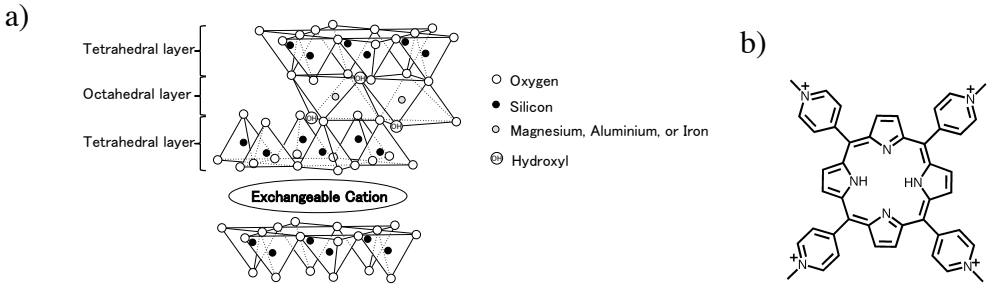

Figure 1. (a) Structural image of MNT, (b) molecular structure of TMPyP

Sample Preparation for Transmission Electron Microscope (TEM) Observation

After the photochemical reaction, the obtained dispersion was centrifuged with Himac CR-20III (8000 rpm, 30 minutes, HITACHI KOKI Co., Ltd.) and the supernatant was removed, then the precipitate was re-dispersed with 2 mL of water. This procedure

was repeated to remove excess gold precursor and TEA. Finally, the precipitate was re-dispersed with 100 μL of water, then 5 μL of the dispersion was casted on the TEM grid (High Resolution Carbon Support Membrane, Okenshoji Co., Ltd.). The obtained grid was dried under vacuum condition over night, and it was spattered with carbon for 4 seconds × 3 times (JEC-560, JEOL, at 4 A) before TEM observation.

Analysis

Deposited gold clusters on MNT surfaces were observed with TEM (JEM-2000FX, JEOL, at 200 kV) and high-angle annular dark-field scanning TEM (HAADF-STEM, JEM-3200FS, JEOL, at 300 kV). UV−vis. absorption spectra were obtained on Shimadzu UV-3150. TG/DTA measurements were carried out with a Shimadzu DTG-60H analyzer to determine the water content of materials.

4.3. Result and discussion

Deposition of the Gold NPs on MNT Surfaces via PTR Method

Expected mechanism of Photosensitized Template Reduction (PTR) method for the generation of gold NPs is as follows. The electron transfer from TEA to excited TMPyP on the clay surface affords reduced spices of TMPyP ($TMPyP_{red.}$) on the clay surface. Then, this $TMPyP_{red.}$ reduces the gold precursor ($[Au(en)_2]^{3+}$) that locates

near the $TMPyP_{red.}$. Through these mechanisms, gold clusters would be produced on the clay surface, and non-aggregated assembly structure of arranging porphyrin molecules may reflect in the assembly of deposited gold clusters. In this mechanism, TEA, TMPyP and gold precursor would act as an electron donor, a photosensitizer and an electron accepter, respectively. In the expected mechanism of PTR method, the initial step is a photo-induced electron transfer from TEA to excited TMPyP on the clay surface. A change of Gibbs free energy (ΔG_{el}) for the electron transfer reaction can be estimated by the an equation proposed by Rehm and Weller(eq 1),[33]

$$\Delta G_{el}\ (kcal\ mol^{-1}) = 23.06\left[E^0(D^+/D) - E^0(A/A^-)\right] - w_p - \Delta G_{00} \qquad \text{(eq. 1)}$$

where $E^0(D^+/D)$ is oxidation potential of TEA, $E^0(A/A^-)$ is reduction potential of TMPyP, w_p is the electrostatic work term that accounts for the effect of coulombic interaction in the products and reactants, and ΔG_{00} is excitation energy of TMPyP, respectively. Oxidation potential of TEA and reduction potential of TMPyP are +1.02 V (vs. NHE, MeCN) and -0.23 V (vs. NHE, water), respectively.[34, 35] Supposing that reduction potential of TMPyP on the clay surface is same to that in a solution, the ΔG_{el} for electron transfer from TEA to excited TMPyP is sufficiently exergonic (ΔG_{el} = -14.8 kcal mol^{-1}) , thus this reaction would proceed efficiently. Absorption spectral change of TMPyP-$[Au(en)_2]^{3+}$-MNT with TEA in aqueous solution during photo-irradiation is shown in Figure 2.

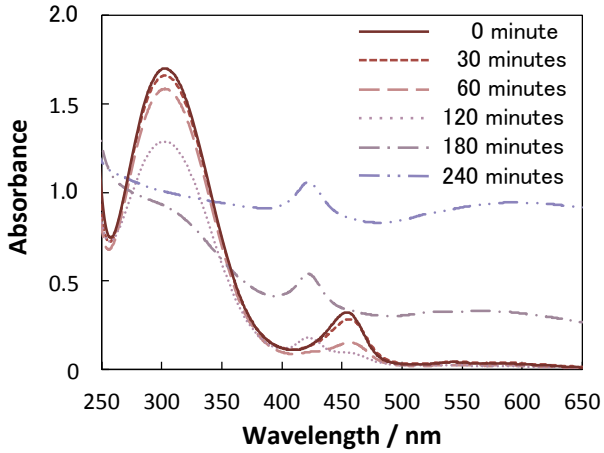

Figure 2. UV-Vis. absorption spectra during the photochemical reaction. Irradiation time = 0, 30, 60, 120, 180, 240 minutes.

The absorption maximum of TMPyP adsorbed on MNT surface shifted to longer wavelength by ca. 30 nm (424 nm → 454 nm) compared to that of TMPyP in aqueous solution without MNT. The spectral shift has been ascribed to the coplanarization of the peripheral mesosubstituted pyridinium groups and the porphyrin ring on the clay surface.[7] Absorption maximum of $[Au(en)_2]^{3+}$ was shifted to shorter wavelength (331 nm → 301 nm), and the extinction coefficient was increased compared to the $[Au(en)_2]^{3+}$ aqueous solution. The absorption spectra of $[Au(en)_2]^{3+}$ in presence/absence of TEA was shown in Figure S1. The same spectral change of the $[Au(en)_2]^{3+}$ was observed in presence of TEA. It suggested that $[Au(en)_2]^{3+}$ formed complex with TEA. Since the absorption band due to TMPyP and $[Au(en)_2]^{3+}$ separates well each other, TMPyP/MNT can be selectively excited with 450 nm light irradiation. The absorption band due to $[Au(en)_2]^{3+}$ almost disappeared at 180 minutes irradiation. It suggested that

gold precursor was reduced by irradiation of 450 nm wavelength light. On the other hand, the absorption band of TMPyP adsorbed on MNT surfaces was decreased instead of the increasing TMPyP in aqueous solution (424 nm). This indicates that TMPyP desorbed from MNT surface as photochemical reaction proceeded. As shown later, gold clusters were generated on the MNT surfaces with very high density, and adsorption site for TMPyP seems to be covered by generated gold NPs. Thus TMPyP may desorb from the MNT surface. As can be seen in the absorption spectra at 180 and 240 minutes irradiation in Figure 1, a new absorption band was observed around 500−650 nm that would corresponds to a plasmon band of gold NPs.[25] It suggests a formation of gold NPs whose diameter is larger than ca. 5 nm between photochemical reaction from 180 to 240 minutes.

TEM observation of Gold NPs deposited via PTR Method

Photochemical reaction sample obtainted with 180 minutes light irradiation was observed by TEM. High and low magnification TEM images of gold NPs prepared by PTR method are shown in Figure 3-(a) and S2, respectively.

a)

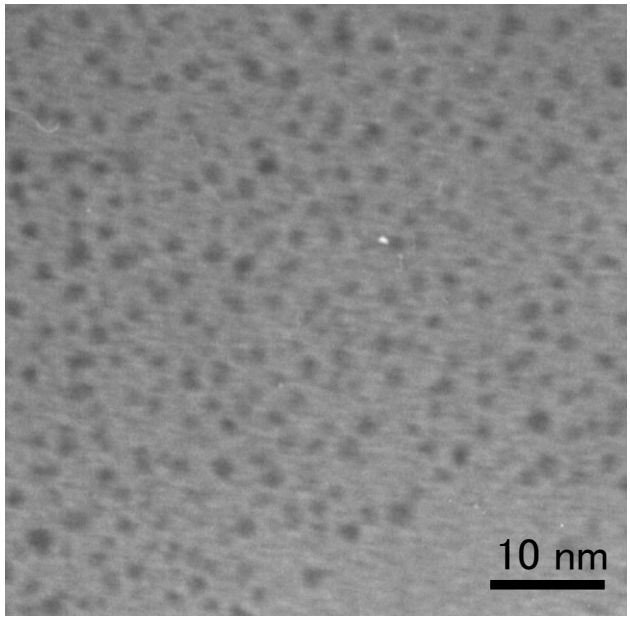

b)

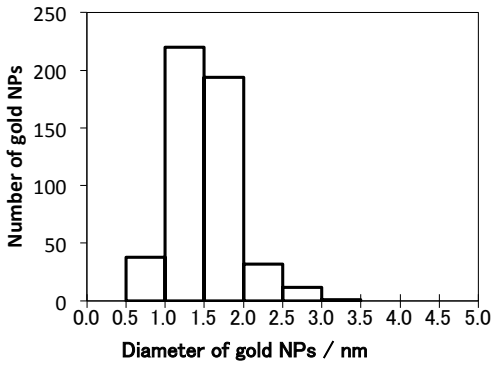

Figure 3. (a) High magnification TEM image of the generated gold clusters on the MNT surface with light irradiation (180 min.), (b) Histogram of the diameter of gold clusters on the MNT surface.

As can be seen in Figure 3-(a), high density small gold NPs (d < 3 nm) were observed on the MNT surface, and gold clusters did not aggregate each other on MNT surface. In addition, these gold clusters were stable during TEM observation when accelerating voltage of TEM was set 200 kV and 300 kV. A histogram of the diameters of the gold

NPs generated with PTR method is shown in Figure 3-(b). Four high magnification TEM images were used for preparing the histogram and the total number of counted clusters is 497. The average diameter of the gold clusters and the standard deviation (σ) were estimated to be 1.5 nm and 0.42 nm, respectively. Some reports have described the generation of the gold NPs on the clay minerals surfaces.[32, 40, 41] Comparing to this method, smaller gold clusters could be deposited with high density without aggregation by PTR method. In low magnification TEM image (Figure S2), relatively large gold particles (d > 10 nm) were observed. Since these large gold particles were also observed in the reference sample where light was not irradiated, these large gold NPs would be produced via thermal reaction. The electron transfer reaction from TEA to gold precursor is not exoergic reaction considering the redox potential of gold precursor and TEA.[34, 35, 39] As described above, TEA and gold precursor formed the complex. We suppose that redox potential of this complex should be different from the redox potential of gold precursor, thus Au^{3+} can be reduced by TEA via thermal reaction, although the reduction rate is very slow. To discuss the reaction rate difference between photochemical and thermal reaction, the changes of absorbance due to gold precursor with and without photo-irradiation were shown in Figure S2. The decreasing rate of the gold precursor in thermal reaction is much slower than that in photochemical reaction. This indicates that gold particles generation in thermal reaction can be almost negligible. In addition, the irradiation wavelength is important in the present system. In the case of UV irradiation, lots of large gold NPs (> c.a. 20 nm) generated, in

contrast to visible light irradiation (average diameter was 1.5 nm). This result also suggests that porphyrin molecules act as sensitizer to reduce Au precursor.

To confirm that gold clusters were generated with high density over a wide region, HAADF-STEM observation under low magnification was examined (Figure 4).

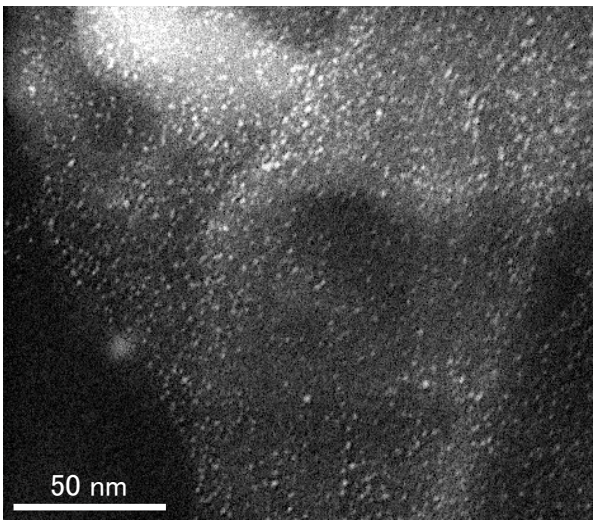

Figure 4. HAADF-STEM image of the gold clusters generated with PTR method on the MNT surfaces.

Heavy atom, such as gold atom, is brighter compared to light atoms (such as Si or Mg) in the dark field image, because the image intensity is proportional approximately to the square of the atomic number.[40, 41] As shown in Figure 4, gold NPs were observed as clear white dot in this dark field image, and gold cluster were observed over a wide region. This image proves that gold nano clusters generated on MNT surfaces with high density and uniformly over a wide area. As a reference experiment, photochemical

reaction without MNT was examined. [TMPyP], [TEA], and [Au(en)$_2$] is 6×10^{-7} M, 0.25 M, 3×10^{-4} M, respectively. In this reference experiment, expected mechanism of this reference experiment is same as PTR method. However, MNT was absent, thus non-aggregated assembled structure of porphyrin molecules were not constructed. If TEA work as protective reagent to generate the gold cluster, the gold cluster will be obtained in spite of the presence or absence of MNT. In this case, the generated gold NPs were large (> 20 nm) and aggregated (not shown). Thus, we believe that gold clusters could be generated near TMPyP molecules on MNT surface, and the arranged TMPyP on MNT surface suppressed the aggregation of gold NPs sterically. To discuss this possibility, we measured inter-particle distances of adjacent gold NPs, and the histogram is shown in Figure 5.

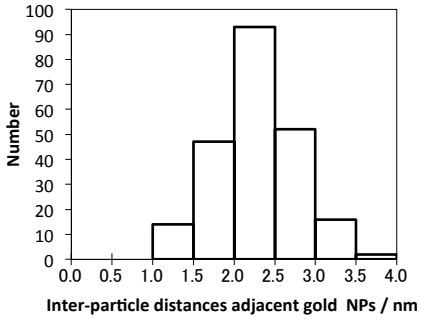

Figure 5. Histogram of inter-particle distance of the adjacent gold clusters on MNT surfaces.

Two TEM images were used for preparing the histogram and the total counted number is 224. The average inter-particle distance (center to center) and the standard deviation (σ) were estimated to be 2.3 nm and 0.5 nm, respectively. According to previously mentioned Size-Matching Effect, the inter-molecular distance between adjacent TMPyP assembled on the MNT surface without aggregation is 2.5 nm on the basis of hexagonal array. The average inter-gold NPs distance well coincides with the inter-molecular distance of porphyrin molecules on the clay surface. This result suggests this assembled structure of gold clusters might reflect the non-aggregated assembly structure of TMPyP adsorbed on the MNT surfaces.

4.4. Conclusion

In this paper, novel strategy, in which porphyrin assembly structure without aggregation on the clay surface was utilized as a template for generating gold clusters, was examined to obtain high density gold clusters assembly. The uniformly gold clusters were deposited on the MNT surfaces without aggregation, and average diameter of the gold cluster was 1.5 nm. In addition, the average inter-particle distance of the nearby gold NPs (center to center) was 2.3 nm. This inter-particle distance indicates that gold clusters generation would reflect the non-aggregated assembled structure of porphyrin molecules on the clay surface. We believe that this Photosensitized

Template Reduction (PTR) method would be useful as a new method to deposit metal NPs on the supporting materials.

4.5. References

1. Scholes, G. D.; Fleming, G. R.; Olaya-Castro, A.; van Grondelle, R. Lessons from nature about solar light harvesting. *Nature Chem.* **2011**, *3*, 763-774.

2. Keating, J.; Sankar, G.; Hyde, T. I.; Kohara, S.; Ohara, K. Elucidation of structure and nature of the PdO-Pd transformation using in situ PDF and XAS techniques. *Phys. Chem. Chem. Phys.* **2013**, *15*, 8555-8565.

3. Lee, C. Y.; Farha, O. K.; Hong, B. J.; Sarjeant, A. A.; Nguyen, S. T.; Hupp, J. T. Light-harvesting metal-organic frameworks (MOFs): efficient strut-to-strut energy transfer in bodipy and porphyrin-based MOFs. *J. Am. Chem. Soc.* **2011**, *133*, 15858-15861.

4. Takahashi, R.; Kobuke, Y. Hexameric macroring of gable-porphyrins as a light-harvesting antenna mimic. *J. Am. Chem. Soc.* **2003**, *125*, 2372-2373.

5. Sasai, R.; Itoh, T.; Ohmori, W.; Itoh, H.; Kusunoki, M. Preparation and Characterization of Rhodamine 6G/Alkyltrimethylammonium/Laponite Hybrid Solid Materials with Higher Emission Quantum Yield. *J. Phys. Chem. C* **2009**, *113*, 415-421.

6. Mandal, S.; Ghatak, C.; Govind, R. V.; Ghosh, S.; Sarkar, N. Pluronic Micellar Aggregates Loaded with Gold Nanoparticles (Au NPs) and Fluorescent Dyes: A Study of Controlled Nanometal Surface Energy Transfer. *J. Phys. Chem. C* **2012**, *116*, 5585-5597.

7. Takagi, S.; Shimada, T.; Ishida, Y.; Fujimura, T.; Masui, D.; Tachibana, H.; Eguchi, M.; Inoue, H. Size-matching effect on inorganic nanosheets: control of distance, alignment, and orientation of molecular adsorption as a bottom-up methodology for nanomaterials. *Langmuir* **2013**, *29*, 2108-2119.

8. Egawa, T.; Watanabe, H.; Fujimura, T.; Ishida, Y.; Yamato, M.; Masui, D.; Shimada, T.; Tachibana, H.; Yoshida, H.; Inoue, H.; Takagi, S. Novel methodology to control the adsorption structure of cationic porphyrins on the clay surface using the "size-matching rule". *Langmuir* **2011**, *27*, 10722-10729.

9. Eguchi, M.; Takagi, S.; Tachibana, H.; Inoue, H. The 'size matching rule' in di-, tri-, and tetra-cationic charged porphyrin/synthetic clay complexes: effect of the inter-charge distance and the number of charged sites. *J. Phys. Chem. Solids* **2004**, *65*, 403-407.

10. Shichi, T.; Takagi, K. Clay minerals as photochemical reaction fields. *J. Photochem. Photobiol. C: Photochem. Rev.* **2000**, *1*, 113-130.

11. Gates, W. P.; Komadel, P.; Madejova, J.; Bujdak, J.; Stucki, J. W.; Kirkpatrick, R. J. Electronic and structural properties of reduced-charge montmorillonites. *Appl. Clay Sci.* **2000**, *16*, 257-271.

12. Dhas, N. A.; Raj, C. P.; Gedanken, A. Preparation of luminescent silicon nanoparticles: A novel sonochemical approach. *Chem. Mater.* **1998**, *10*, 3278-3281.

13. Jamet, M.; Wernsdorfer, W.; Thirion, C.; Mailly, D.; Dupuis, V.; Mélinon, P.; Pérez, A. Magnetic Anisotropy of a Single Cobalt Nanocluster. *Phys. Rev. Lett.* **2001**, *86*, 4676-4679.

14. Aiken, J. D.; Finke, R. G. A review of modern transition-metal nanoclusters: their synthesis, characterization, and applications in catalysis. *J. Mol. Catal. Chem.* **1999**, *145*, 1-44.

15. Sakamoto, M.; Tanaka, D.; Tsunoyama, H.; Tsukuda, T.; Minagawa, Y.; Majima, Y.; Teranishi, T. Platonic hexahedron composed of six organic faces with an inscribed Au cluster. *J. Am. Chem. Soc.* **2012**, *134*, 816-9.

16. Adhikari, B.; Banerjee, A. Facile Synthesis of Water-Soluble Fluorescent Silver Nanoclusters and Hg^{II} Sensing. *Chem. Mater*. **2010**, *22*, 4364-4371.

17. Roy, S.; Paluia, G.; Banerjee, A. The as-prepared gold cluster-based fluorescent sensor for the selective detection of As^{III} ions in aqueous solution. *Nanoscale* **2012**, *4*, 2734-2740.

18. Roy, S.; Baral, A.; Banerjee, A. Tuning of Silver Cluster Emission from Blue to Red Using a Bio-Active Peptide in Water. *ACS Appl. Mater. Inter.* **2014**, *6*, 4050-4056.

19. Ghosh, A.; Hassinen, J.; Pulkkinen, P.; Tenhu, H.; Ras, H. A. R.; Pradeep, T. Simple and Efficient Separation of Atomically Precise Noble Metal Clusters. *Anal. Chem.* **2014**, *86*, 12185-12190.

20. Kelly, K. L.; Coronado, E.; Zhao, L. L.; Schatz, G. C. The optical properties of metal nanoparticles: The influence of size, shape, and dielectric environment. *J. Phys. Chem. B* **2003**, *107*, 668-677.

21. Eguchi, M.; Mitsui, D.; Wu, H. L.; Sato, R.; Teranishi, T. Simple reductant concentration-dependent shape control of polyhedral gold nanoparticles and their plasmonic properties. *Langmuir* **2012**, *28*, 9021-9026.

22. Haruta, M.; Yamada, N.; Kobayashi, T.; Iijima, S. Gold Catalysts Prepared by Coprecipitation for Low-Temperature Oxidation of Hydrogen and of Carbon-Monoxide. *J. Catal.* **1989**, *115*, 301-309.

23. Corma, A.; Garcia, H. Supported gold nanoparticles as catalysts for organic reactions. *Chem. Soc. Rev.* **2008**, *37*, 2096-2126.

24. Della Pina, C.; Falletta, E.; Prati, L.; Rossi, M. Selective oxidation using gold. *Chem. Soc. Rev.* **2008**, *37*, 2077-2095.

25. Kanehara, M.; Kodzuka, E.; Teranishi, T. Self-assembly of small gold nanoparticles through interligand interaction. *J. Am. Chem. Soc.* **2006**, *128*, 13084-13094.

26. Hussain, I.; Graham, S.; Wang, Z. X.; Tan, B.; Sherrington, D. C.; Rannard, S. P.; Cooper, A. I.; Brust, M. Size-controlled synthesis of near-monodisperse gold nanoparticles in the 1-4 nm range using polymeric stabilizers. *J. Am. Chem. Soc.* **2005**, *127*, 16398-16399.

27. Andres, R. P.; Bielefeld, J. D.; Henderson, J. I.; Janes, D. B.; Kolagunta, V. R.; Kubiak, C. P.; Mahoney, W. J.; Osifchin, R. G. Self-Assembly of a Two-Dimensional Superlattice of Molecularly Linked Metal Clusters. *Science* **1996**, *273*, 1690-1693.

28. Collier, C. P. Reversible tuning of silver quantum dot monolayers through the metal-insulator transition. *Science* 1997, 277, 1978-1981

29. Kamat, P. V. Photophysical, photochemical and photocatalytic aspects of metal nanoparticles. *J. Phys. Chem. B* **2002**, *106*, 7729-7744.

30. McTiernan, C. D.; Alarcon, E. I.; Hallett-Tapley, G. L.; Murillo-Lopez, J.; Arratia-Perez, R.; Netto-Ferreira, J. C.; Scaiano, J. C. Electron transfer from the benzophenone triplet excited state directs the photochemical synthesis of gold nanoparticles. *Photochem. Photobiol. Sci.* **2014,** *13*, 149-53.

31. Ravaine, S.; Fanucci, G. E.; Seip, C. T.; Adair, J. H.; Talham, D. R. Photochemical generation of gold nanoparticles in Langmuir-Blodgett films. *Langmuir* **1998,** *14*, 708-713.

32. Fujimura, T.; Misaki, Y.; Masui, D.; Shimada, T.; Takagi, S. Preparation of uniformly dispersed gold nano particles on the clay surface. *Clay science* **2012,** *16*, 121-125.

33. Rehm, D.; Weller, A. Kinetics of Fluorescence Quenching by Electron and H-Atom Transfer. *Isr. J. Chem.* **1970**, *8*, 259-271.

34. Kalyanasundaram, K.; Neumannspallart, M. Photophysical and Redox Properties of Water-Soluble Porphyrins in Aqueous-Media. *J. Phys. Chem.* **1982**, *86*, 5163-5169.

35. Ma, B.; Djurovich, P. I.; Thompson, M. E. Excimer and electron transfer quenching studies of a cyclometalated platinum complex. *Coord. Chem. Rev.* **2005**, *249*, 1501-1510.

36. Hostetler, M. J.; Wingate, J. E.; Zhong, C.-J.; Harris, J. E.; Vachet, R. W.; Clark, M. R.; Londono, J. D.; Green, S. J.; Stokes, J. J.; Wignall, G. D.; Glish, G. L.; Porter, M. D.; Evans, N. D.; Murray, R. W. Alkanethiolate Gold Cluster Molecules with Core Diameters from 1.5 to 5.2 nm: Core and Monolayer Properties as a Function of Core Size. *Langmuir* **1998**, *14*, 17-30.

36. Zhu, L.; Letaief, S.; Liu, Y.; Gervais, F.; Detellier, C. Clay mineral-supported gold nanoparticles. *Appl. Clay Sci.* **2009**, *43*, 439-446.

37. Mitsudome, T.; Noujima, A.; Mizugaki, T.; Jitsukawa, K.: Kaneda, K. Efficient Aerobic Oxidation of Alcohols using a Hydrotalcite-Supported Gold Nanoparticle Catalyst. *Adv. Syn. Catal.* **2009**, *351*, 1890-1896.

39. Synthesis, Structures, and Electrochemistry of Gold(III) Ethylenediamine Complexes and Interactions with Guanosine 5‘-Monophosphate, *Inorg. Chem.* **2006**, *45*, 2688-2694.

40. Watanabe, K.; Yamazaki, T.; Hashimoto, I.; Shiojiri, M. Atomic-resolution annular dark-field STEM image calculations. *Phys. Rev. B* **2001**, *64*, 115432.

41. Utsunomiya, S.; Ewing, R. C. Application of High-Angle Annular Dark Field Scanning Transmission Electron Microscopy, Scanning Transmission Electron Microscopy-Energy Dispersive X-ray Spectrometry, and Energy-Filtered Transmission Electron Microscopy to the Characterization of Nanoparticles in the Environment. *Environ. Sci. Tech.* **2003**, *37*, 786-791.

Chapter 5

Construction of Layered Structure of Porphyrin − Saponite Clay Complex

5.1. Introduction

As described in general introduction and other chapters, we have investigated the self-assembly of the multivalent cationic dye on the clay minerals surfaces.[1-5] We have reported an interesting porphyrin−clay minerals hybrid in which the porphyrin molecules densely adsorb on the exfoliated clay nano-sheets without aggregation and formation of these novel un-aggregated dye assemblies on the clay surfaces is attributed to size matching of the distance between cationic site of the dyes and anionic site on the clay surfaces.[6,7] It has been revealed that the some of the dyes adsorbed on the clay surfaces show the unique photo-physical properties which differ from the photo-physical properties in aqueous medium.[8,9] Furthermore, we reported the efficiently energy transfer reaction between two dyes which co-adsorbed on the clay surfaces.[10-13] As described above, the clay minerals can be expected as a unique host material as a photochemical reaction field. However, these investigations demonstrated on the surfaces on exfoliated clay mineral which was dispersed in aqueous medium, thus it is difficult to apply to the practical system. For further application, t he solid state reaction system such as a membrane is needed for further application of the energy transfer reaction system. In the solid state, layered materials such as clay minerals tend to be stacked, thus the techniques to intercalate the dyes into the interlayer spaces of the

host materials, then layered structure composed of guest molecules and host layered mateials should be constructed.

A wide variety of nanolayered compounds have been examined to construct functional materials including dyes.[14−19] However, it is very difficult to control adsorption behavior of dyes in the compounds. Dye molecules tend to form aggregates very easily on the solid surface.[20−25] Thus, there is few report on the high density and non-aggregation intercalation reaction of dyes into the inorganic layered materials.[26−32] In this chapter, we examined the preparation of transparent clay thin film where porphyrin molecules are densely intercalated without discernible aggregation and constructed the layered structure composed of clay mineral and guest dye molecules. This technique would be useful to develop practical systems such as artificial light harvesting systems.

5.2. Experimental Section

Materials

Sumecton SA (SSA, Kunimine) was used as a synthetic cation exchangeable clay mineral. The stoichiometric formula of SSA is $[(Si_{7.20}Al_{0.80})(Mg_{5.97}Al_{0.03})O_{20}(OH)_4]^{-0.77}(Na_{0.49}Mg_{0.14})^{+0.77}$, the surface area is 750 m^2 g^{-1}, and the cation exchangeable capacity (CEC) is 1.00 mequiv g^{-1}. The average area per an anionic site is calculated to be 1.25 nm^2, and the average distance between anionic sites on the SSA sheets is estimated to be 1.2 nm on the basis of a hexagonal array. Tetrakis(1-methyl-4-pyridiniumyl)porphyrin (TMPyP) was purchased from

Aldrich. The counterion (tosylate anion) was exchanged with chloride by use of an ion exchange column (ORGANOAMBERLITEIRA400JCL). TMPyP, in which the distance between adjacent cationic sites is calculated to be 1.1 nm (PM3 method), was used as the cationic porphyrin in this study. The glass substrate (cover glass (C024241), 24 mm × 24 mm, thickness is 0.145 ± 0.025 mm) was purchased from Matsunami Glass Ind., Ltd.

Preparation of Thin Film Composed of Only SSA

The glass substrate was sonicated with water for 30 min and then treated in sulfuric acid (Kanto Chemical, 96%) overnight at room temperature. Then, the glass substrate was washed with enough water. 2 mL of SSA dispersion (100 mg L^{-1} in water:dioxane = 4:1 (v:v)) was filtered through a PTFE membrane filter (pore size = 0.1 μm). Because few SSA was observed in the filtrate, SSA was almost filtered (ca. 99%). The transparent SSA thin film was obtained by transferring the residue upon the glass substrate.[33-35] The thin film was dried up under vacuum overnight.

Preparation of TMPyP/SSA Hybrid Film.

The SSA thin films were immersed in water:ethanol = 1:2 (v:v) solution containing TMPyP for 48 h at room temperature with constant stirring until the TMPyP absorption of the solution could no longer be detected or could no longer be changed. The concentration of the TMPyP was changed to control the loading levels. For example, 12 mL of TMPyP solution (4.17×10^{-7} and 8.33×10^{-7} M) was used to prepare the 10%

and 20% versus CEC of the TMPyP/SSA hybrid films. In every loading level, TMPyP in the solution almost disappeared after the immersion process. The CEC of the SSA film can be calculated by the amount of loaded SSA (2.0×10^{-4} g (= 0.1 g L^{-1} × 2.0 × 10^{-3} L)) and the CEC of SSA (1.00 mequiv g^{-1}). The CEC of the SSA film is calculated as 2.0×10^{-7} equiv (= 1.00 mequiv g^{-1} × 2.0 × 10−4 g). The obtained green transparent thin films were dried up under vacuum overnight.

Analysis

UV−vis. absorption spectra were obtained on Shimadzu UV-3150 and UV-2550. The fluorescence spectra were measured with JASCO FP-6600 spectrofluorometer, and excitation light was set at 485 nm. When fluorescence spectra were measured, a cut filter (50% transmittance = 590 nm, Edmund, OG590) was used. The glass plate was set at 45° against the direction of excitation light source and the detector of emission. The PL quantum yield of TMPyP/SSA thin films at various loading levels was evaluated using an absolute PL quantum yield measurement apparatus (C9920-02, Hamamatsu Photonics) at λ_{ex} = 480 nm.[36] TG/DTA measurement was carried out with a Shimadzu DTG-60H to determine the water contents of TMPyP and SSA. To measure quantum yields of TMPyP/SSA thin films at various loading levels, the films were prepared as follows. The concentration of TMPyP was constant, and the amount of SSA was changed to control the loading level of TMPyP. The concentration of TMPyP in the membrane was unified as 8.33×10^{-9} mol cm^{-2}. Other condition was the same as a previously described method. In atomic force microscopy (DFM mode) measurement,

SPI4000 and SPA300HV systems (SII Nano-Technology Inc.) were used, and DF-40 (SII Nano-Technology Inc.) was used as a cantilever. The X-ray diffraction (XRD) pattern was measured with a RINT TTRIII (Rigaku).

5.3. Result and Discussion

Absorption Spectra and Stability of TMPyP/SSA Thin Hybrid Film

A photograph of the TMPyP/SSA hybrid film is shown in Figure 1.

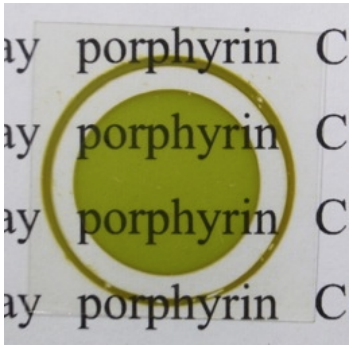

Figure 1. Photograph of transparent TMPyP/SSA hybrid thin film.

As can be seen, the transparency of the membrane is quite high to measure the absorption spectrum. The absorption spectra of the TMPyP/SSA hybrid thin film where the loading level of TMPyP was 30% versus CEC under air condition and TMPyP in solution (water:EtOH = 1:2 (v:v)) are shown in Figure 2.

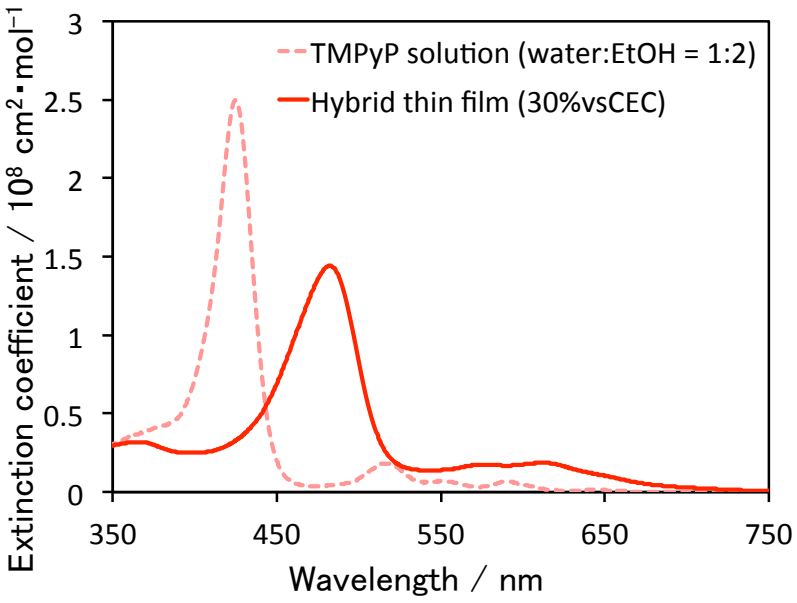

Figure 2. Absorption spectra of the TMPyP/SSA hybrid film at 30% versus CEC (solid line) and TMPyP solution in water:EtOH = 1:2 (broken line).

The λmax of TMPyP in the membrane and in solution were 483 nm ($\varepsilon = 1.44 \times 10^8$ cm^2 mol^{-1}) and 425 nm ($\varepsilon = 2.50 \times 10^8$ cm^2 mol^{-1}), respectively. The Soretband of TMPyP/SSA hybrid film was broad compared to that of TMPyP in solution. The values of spectral integral were almost the same (TMPyP/SSA film = 5.63×10^{11} cm mol^{-1} and TMPyP solution = 5.87×10^{11} cm mol^{-1}). As reported before, TMPyP adsorbs on the exfoliated SSA surface up to the loading level of 100% versus CEC of the SSA without aggregation in water. The absorption spectrum of the porphyrin adsorbed on exfoliated SSA surface shows a considerable bathochromic shift. The absorption maximum (λ_{max}) of the Soret band shifts to longer wavelength by ca. 30 nm compared to that in water without SSA. The considerable spectral change has been ascribed to the coplanarization of the peripheral mesosubstituted pyridinium groups and the porphyrin ring on the SSA

surface.[37–39] The SSA thin film is stable in air but is gradually suspended in water. Interestingly, TMPyP/SSA film was quite stable in water, contrary to SSA film. We tested the stability of TMPyP/SSA film in aqueous condition by the observation of absorbance of porphyrin in the membrane. The TMPyP/SSA film was completely stable in water for over 30 days when the loading level of TMPyP was 5% and 25%, while the SSA only film was rather unstable. 5% loading was enough to stabilize the membrane. We examined the effect of solvent composition for the intercalation process of TMPyP. When water:EtOH = 4:1 (v:v), a part of SSA film was dissolved during the intercalation process of TMPyP. On the other hand, TMPyP was not intercalated into the interlayer space effectively, when water:EtOH = 1:4 (v:v). These results indicate that the appropriate swelling of the SSA sheets is important for the effective intercalation of TMPyP and the stability of the film. The thickness of SSA only film was measured by DFM. The thickness of the film was ca. 340 nm as shown in Figure 3.

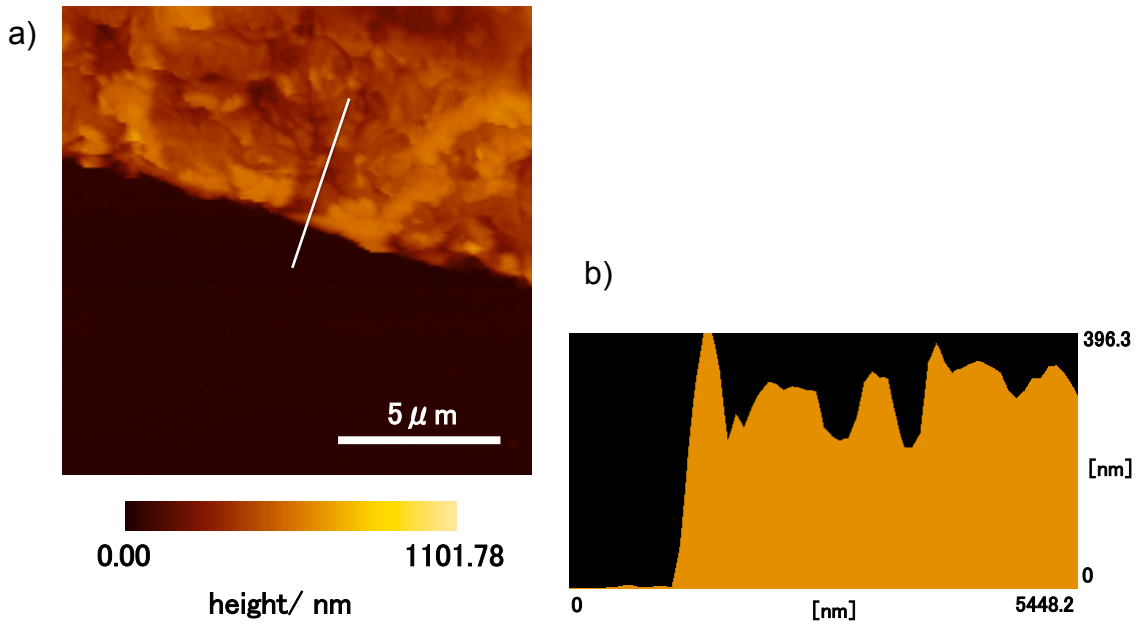

Figure 3. a) DFM image of the SSA only film, b) Cross section image of the film at the white line in a).

This observed thickness corresponds well to the calculated thickness. The theoretical thickness of the membrane is calculated as follows. The amount of loaded SSA is calculated to be 2.0×10^{-4} g by the volume (2.0×10^{-3} L) and the concentration (0.1 g L^{-1}) of SSA dispersion. Then, the number of stacked layers was calculated by the theoretical surface area of SSA (750 m^2 g^{-1}), loaded amount of SSA (2.0×10^{-4} g), and the area of the SSA film (2.4×10^{-4} m^2). The number of stacked layers is ca. 310 (= $750 \times 2.0 \times 10^{-4}$ /2/(2.4×10^{-4})). The thickness of the SSA nanosheet including interlayer space is 1.28 nm judging from XRD data. Thus, the calculated thickness of SSA film is 397 nm.

Absorption Spectra and X-ray Diff raction of TMPyP/SSA Hybrid Thin Film at Various Loading Levels

absorption spectra of TMPyP/SSA hybrid thin film at various porphyrin loading levels are shown in Figure 4a. It is turned out that the absorption spectra retain the same shapes up to the relatively high loading level (～ 35% versus CEC). The plots of absorbance at the wavelength of the Soret band (475.5 nm) against the porphyrin loading levels are shown in Figure 4b. The linearity of the plots was retained up to ca. 35% versus CEC, although the absorption spectra of the TMPyP/SSA complex obtained by the freeze− thaw cycles changed even at low porphyrin loading levels (～ 8% versus CEC).13 As can be seen in Figure 4b, the absorbance of TMPyP/SSA thin film above ca. 35% versus CEC does not increase, and the λmax of Soret band was slightly blue-shifted. These observations indicate that ca. 35% versus CEC was saturated adsorption amount, and a small amount of aggregate, such as H-type aggregate, would form above ca. 35% versus CEC. It should be mentioned that photoactivity, judging from fl uorescence quantum yield, is almost retained even at 50% loadings versus CEC as described later. Here, the loading level of 100% versus CEC means that TMPyP fulfills all anionic sites on the SSA surface. If TMPyP forms monolayer structure with the parallel orientation respect to the SSA surface, the maximum adsorption rate of TMPyP without aggregation should to be 50% versus CEC, which is called a sandwich structure, as shown in Figure 4c.

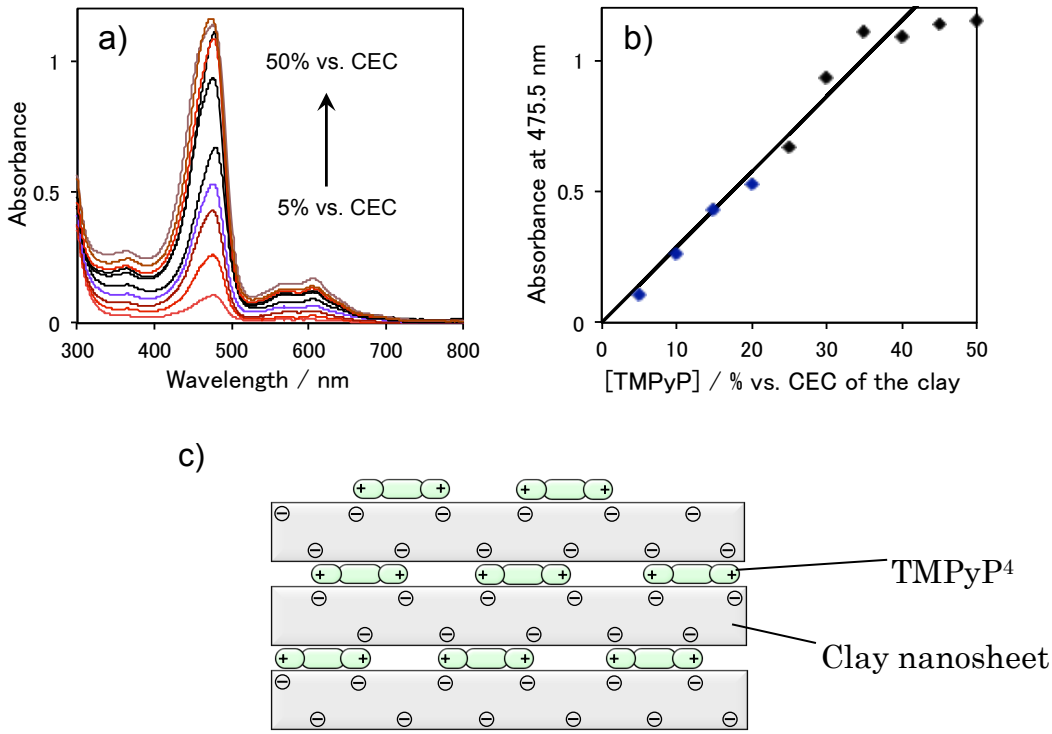

Figure 4. (a) Absorption spectra of TMPyP/SSA hybrid thin films at various loading level (5−50% versus CEC of the clay, (b) absorbance−adsorption density plot of TMPyP/SSA hybrid thin film in aqueous solution, and (c) ideal structure of TMPyP/SSA hybrid thin film at 50% versus CEC of the SSA film (side view).

In order to estimate the orientation of TMPyP in the SSA interlayer space, an X-ray diff raction (XRD) measurement was carried out under an air condition. The XRD patterns of the membrane, where the loading levels of TMPyP are 0− 50%, are shown in Figure 5.

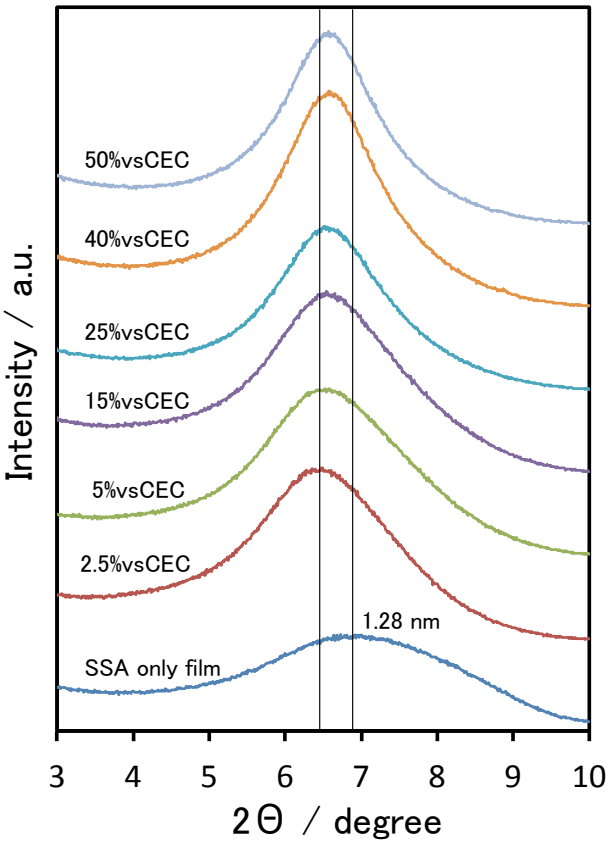

Figure 5. X-ray diffraction pattern of SSA film and TMPyP/SSA hybrid films at various loading levels of TMPyP.

The interlayer distance of SSA only film was estimated to be 0.31 nm, supposing that the thickness of SSA is 0.97 nm. It is almost identical with the interlayer distance of SSA powder, and 0.31 nm almost corresponds to the thickness of one water layer. On the other hand, interlayer distance of TMPyP/SSA hybrid fi lm at 5− 50%versus CEC was estimated to be 0.37− 0.41 nm. Considering the thickness of the porphyrin molecule (∼ 0.35 nm) and the existence of adsorbed water on the SSA surface, the orientation of the TMPyP in the SSA layers is almost parallel to the SSA sheets as

monolayer (not bilayer) at all loadings. If the adsorption amount of TMPyP had been larger than 50% versus CEC, the structure of intercalated TMPyP (shown in Figure 6) should have been bilayer.

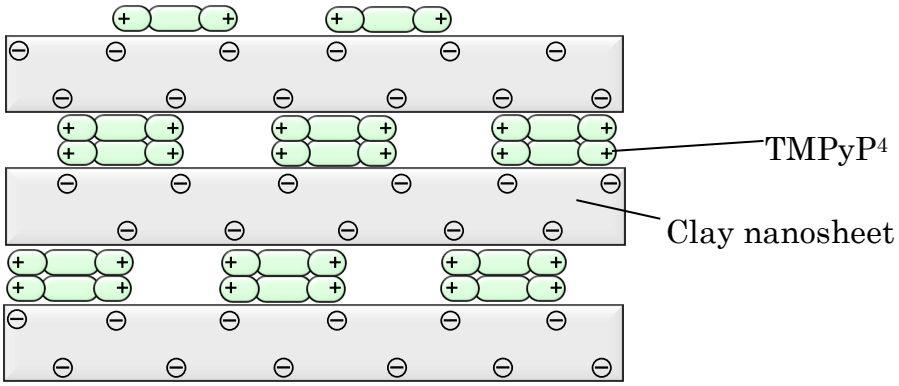

Figure 6. Ideal structure of TMPyP/SSA hybrid thin film when loading level of TMPyP is 100% versus CEC (side view). In this case, the structure of intercalated TMPyP would be bilayer.

Because the experimental results deny the existence of aggregated porphyrin, the structure of Figure 6 should be denied. The XRD pattern of TMPyP/SSA was sharp compared to SSA only fi lm. It indicates that TMPyP excludes the water from the interlayer space and reduces the modulation of interlayer distance with water. In addition, the XRD pattern of TMPyP/SSA slightly shifted to high diff raction angle, indicating the decrease of interlayer distance, when the loading level of TMPyP was increased. It might suggest that the interlayer space of TMPyP/SSA hybrid fi lm became hydrophobic with the increase of TMPyP, and thus the interlayer water was excluded

and the interlayer distance of TMPyP/SSA hybrid fi lm at high loading level of TMPyP decreased compared to that at low loading level of porphyrin. Judging from the absorption behavior and XRD measurement, it is turned out that the TMPyP/SSA hybrid thin films with the high-density intercalation of porphyrins as a monolayer can be prepared, although such high density packing without discernible aggregation is very difficult to construct in general. The effective size-matching effect[13,14] would realize the nonaggregated structure of TMPyP at high density conditions. At this condition (35% versus CEC), the average intermolecular distance is calculated to be 2.87 nm on the basis of hexagonal array. XRD profiles and absorption spectra of the films were measured under air and vacuum conditions. The films were dried at 70 ° C for 1.5 h in vacuum using a homemade hermetic cell. As a typical example, the XRD profiles and absorption spectra of the fi lm where the TMPyP loading level is 30% versus CEC in air and vacuum are shown in Figure 7.

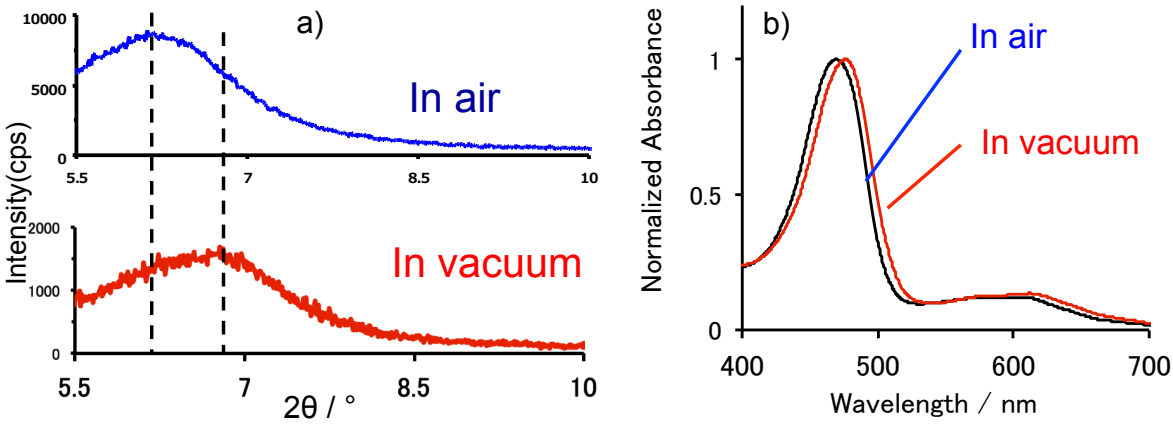

Figure 7. a) X-ray diffraction profiles and b) absorption spectra of TMPyP/SSA hybrid thin film at 30% versus CEC under air and vacuum.

The interlayer space of TMPyP/SSA hybrid film under vacuum condition decreased by ca. 0.1 nm compared to that under air condition. It is suggested that interlayer water of the SSA nanosheets decreased under vacuum, and the interlayer distance became shorter than that under air. On the other hand, the λ_{max} of the Soret band under vacuum shifted to longer wavelength by ca. 5 nm compared to that under air. These results indicate that the porphyrin molecule becomes more flat with a rotation of the pyridinium group and associate with the SSA surface stronger, under vacuum. Under vacuum condition, the absorbance− concentration plots at the Soret band showed good linearity against the porphyrin loading levels up to *ca.* 45% versus CEC, which is almost equal to the theoretical saturation density, as shown in Figure 8. In the case of saturated TMPyP/SSA film under air condition, a small amount of TMPyP would form the aggregate in the interlayer space of the SSA film. One of the major driving forces for aggregation of TMPyP would be hydrophobic interaction. In the case of vacuum condition, the amount of water in the interlayer space of the SSA film would decrease, and thus, the hydrophobic interaction would become weak.

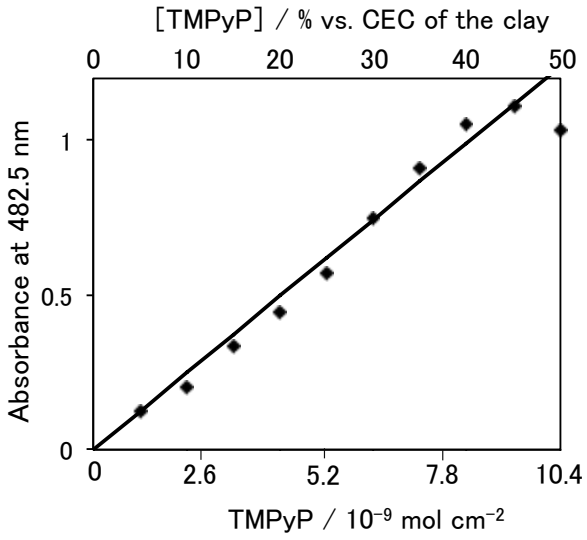

Figure 8. Absorbance−TMPyP concentration plot of TMPyP/SSA hybrid thin film under vacuum condition. **X**-axis at the bottom of the graph box is the density of TMPyP, and that at the top of the graph box is loading level of TMPyP versus CEC of the SSA film.

Therefore, TMPyP, which is intercalated in the interlayer space of the SSA fi lm, does not aggregate under vacuum conditions. The flat configuration of the porphyrin molecule in vacuum could enhance the electrostatic interaction with the SSA surface and stabilize the adsorption state through the more effective size-matching effect. In order to confi rm the orientation of TMPyP intercalated in the interlayer space of SSA fi lm, we examined the polarized visible-light-ATR (Vis-ATR) spectroscopy[40−44] of the TMPyP/SSA hybrid fi lm on the quartz waveguide. The dichroic absorption spectra measured by the waveguide system are shown in Figure 9.

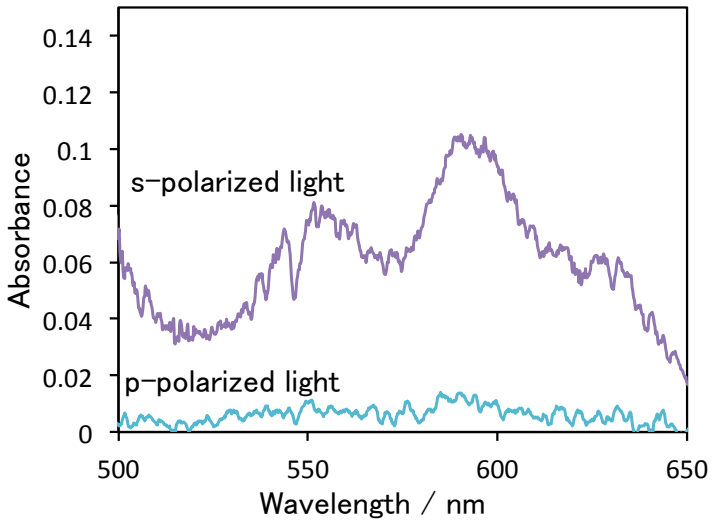

Figure 9. Polarized Vis-ATR spectra of intercalated TMPyP in SSA film on the waveguide quartz glass.

The absorbance of Q-band with s-polarized light was much larger than that with p-polarized light. From the s/p ratio, the orientation angle of porphyrin plane was calculated to be lower than 6° with respect to the quartz surface. Thus, the intercalated TMPyP was almost parallel with respect to the quartz surface. This indicates that SSA layer is almost parallel with respect to the quartz substrate because the orientation of intercalated TMPyP should be almost parallel with respect to the SSA surface judging from XRD pattern. These results strongly support the structure of TMPyP/SSA hybrid films shown in Figure 4c.

Fluorescence Behavior of TMPyP/SSA Hybrid Film

To discuss the photoactivity of TMPyP intercalated in SSA film, the fluorescence spectra and fl uorescence quantum yield of TMPyP/SSA hybrid thin films at various loading levels were measured. The fluorescence spectra of TMPyP/SSA film at various loading levels are shown in Figure 10.

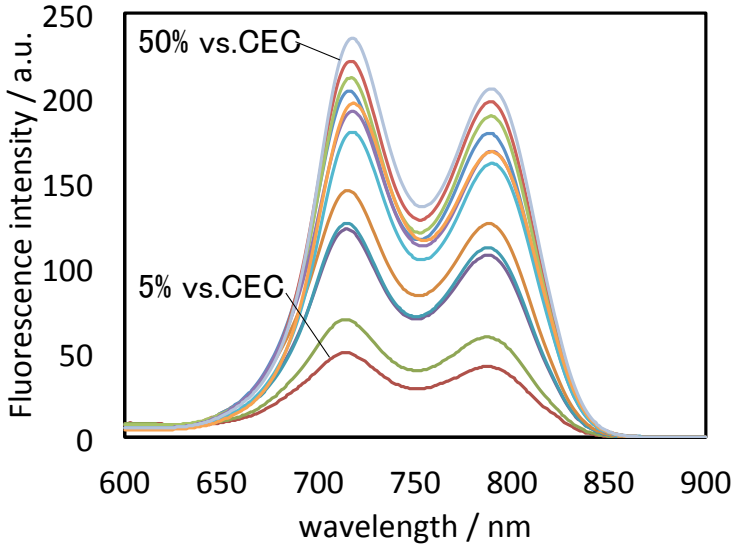

Figure 10. Fluorescence spectra of TMPyP/SSA hybrid film at various loading level excited at 485 nm.

The loading levels are 5− 50% versus CEC of SSA. In this experiment, the concentration of intercalated TMPyP was changed to control the loading level of TMPyP in the SSA fi lm. The fluorescence maximum of porphyrin in the membrane (λmax = 715 nm) shifts to longer wavelength compared to that adsorbed on the exfoliated SSA in water (λmax = ca. 688 nm). This shift is due to the enhancement of the flattening of porphyrin molecule between SSA sheets in the membrane as reported

before.[28–30] The shape of fluorescence spectra of TMPyP/SSA hybrid film was almost same, when the porphyrin loading level was changed from 5% to 50% versus CEC of SSA. This suggests that any new luminescence species, such as J-type aggregates, were not formed in the membrane system. The fl uorescence intensity at 715 and 788 nm are plotted against the absorptivity ($1 - 10^{-Abs}$) of TMPyP/SSA film at various loading level as shown in Figure 11.

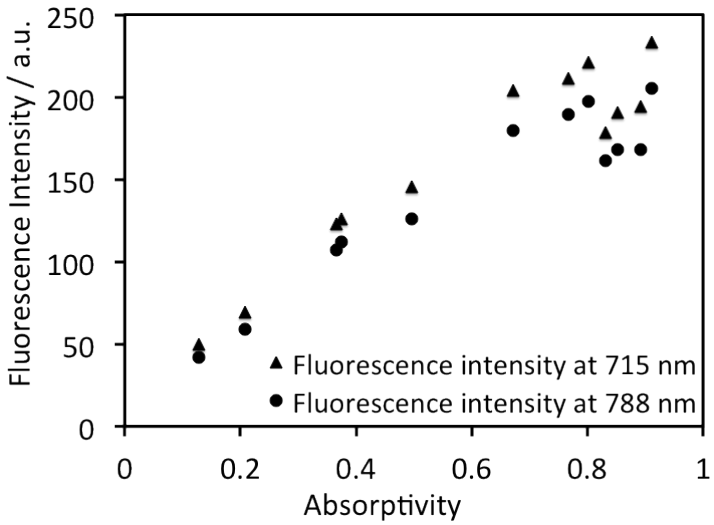

Figure 11. Plot of the fluorescence intensity (vertical axis) against the absorptivity ($1\text{-}10^{-Abs}$) (horizontal axis) at 715 nm (▲) and 788 nm (●).

It shows a nearly linear relationship between the fluorescence intensity and the absorptivity. Thus, it is proved that significant fluorescence quenching was not observed at any density of porphyrin in the membrane system. In the case of fluorescence measurement using typical rectangular optical system, the fluorescence

suffers the effect of scattering and reabsorption. Thus, absolute PL quantum yield measurement apparatus with integrating sphere was used to obtain more reliable data. at various loading levels were ca. 0.02, and the quantum yield did not depend on the loading level of TMPyP. This result also proves that TMPyP intercalated in SSA interlayer space does not aggregate and does not suffer fluorescence quenching. Although ϕ_f of TMPyP in the membrane is lower than that of TMPyP adsorbed on the dispersed SSA surface in water ($\phi_f = 0.048$),[15] the fact that ϕ_f does not depend on the density of porphyrin indicates that the observed ϕ_f in the membrane system is intrinsic. From this result, it is proved that significant fluorescence quenching was not observed at any density of porphyrin in the membrane system. This observation is very important from the viewpoint of photochemistry, since no fluorescence quenching means that the dye keeps the photoactivity even under the high density conditions.

5.4. Conclusion

In this study, the TMPyP/SSA hybrid thin film was developed by a penetration method with adequate solvent conditions. The film was sufficiently stable under air and in water. It is turned out that TMPyP can be intercalated in the clay membrane under the high density condition without an aggregation. The fluorescence quantum yield of TMPyP/SSA hybrid films did not depend on the density of porphyrin, and significant fluorescence quenching was not observed at any density of porphyrin in the membrane system. This indicates that TMPyP intercalated in the SSA fi lm keeps the photoactivity even under the high density conditions. We will examine the photochemical reactions

such as energy transfer reactions aiming an artificial light harvesting system by using porphyrin− clay membrane obtained in the present study.[44−53]

5.5. Reference

1. Takagi, S.; Shimada, T.; Ishida, Y.; Fujimura, T.; Masui, D.; Tachibana, H.; Eguchi, M.; Inoue, H. Size-matching effect on inorganic nanosheets: control of distance, alignment, and orientation of molecular adsorption as a bottom-up methodology for nanomaterials. *Langmuir* **2013,** *29* , 2108-19.

2. Tsukamoto, T.; Shimada, T.; Takagi, S. Correction to "Photochemical Properties of Mono-, Tri-, and Penta-Cationic Antimony(V) Metalloporphyrin Derivatives on a Clay Layer Surface". *J. Phys. Chem. A* **2013,** *117*, 13037-13037.

3. Konno, S.; Fujimura, T.; Otani, Y.; Shimada, T.; Inoue, H.; Takagi, S. Microstructures of the Porphyrin/Viologen Monolayer on the Clay Surface: Segregation or Integration? *The J. Phys. Chem. C* **2014,** *118* , 20504-20510.

4. Umemoto, T.; Ohtani, Y.; Tsukamoto, T.; Shimada, T.; Takagi, S. Pinning effect for photoisomerization of a dicationic azobenzene derivative by anionic sites of the clay surface. *Chem. comm.*. **2014,** *50*, 314-6.

5. Takagi, S.; Aratake, Y.; Konno, S.; Masui, D.; Shimada, T.; Tachibana, H.; Inoue, H. Effects of porphyrin structure on the complex formation behavior with clay. *Microporous and Mesoporous Materials* **2011,** *141*, 38-42.

6 Takagi, S.; Shimada, T.; Eguchi, M.; Yui, T.; Yoshida, H.; Tryk, D. A.; Inoue, H., High-Density Adsorption of Cationic Porphyrins on Clay Layer Surfaces without Aggregation: The Size-Matching Effect. *Langmuir*, **2002**, *18*, 2265-2272.

7 Egawa, T.; Watanabe, H.; Fujimura, T.; Ishida, Y.; Yamato, M.; Masui, D.; Shimada, T.; Tachibana, H.; Yoshida, H.; Inoue, H.; Takagi, S. Novel Methodology To Control the Adsorption Structure of Cationic Porphyrins on the Clay Surface Using the "Size-Matching Rule". *Langmuir*, **2011**, *27*, 10722–10729.

8. Ishida, Y.; Shimada, T.; Takagi, S. Artificial Light-Harvesting Model in a Self-Assembly Composed of Cationic Dyes and Inorganic Nanosheet. *J. Phys.Chem. C* **2013,** *117*, 9154-9163.

9. Tsukamoto, T.; Shimada, T.; Takagi, S. Unique Photochemical Properties ofp-Substituted Cationic Triphenylbenzene Derivatives on a Clay Layer Surface. *J. Phys. Chem. C* **2013,** *117* , 2774-2779.

10. Hagiwara, S.; Ishida, Y.; Masui, D.; Shimada, T.; Takagi, S. Unique photochemical behavior of novel tetracationic pyrene derivative on the clay surface. *Tetrahedron Lett.* **2012,** *53*, 5800-5802.

11. Ishida, Y.; Shimada, T.; Masui, D.; Tachibana, H.; Inoue, H.; Takagi, S. Efficient excited energy transfer reaction in clay/porphyrin complex toward an artificial light-harvesting system. *J. Amer. Chem. Soc.* **2011,** *133*, 14280-6.

12. Ishida, Y.; Kulasekharan, R.; Shimada, T.; Ramamurthy, V.; Takagi, S. Supramolecular-Surface Photochemistry: Supramolecular Assembly Organized on a Clay Surface Facilitates Energy Transfer between an Encapsulated Donor and a Free Acceptor. *J. Phys. Chem. C* **2014,** *118*), 10198-10203.

13. Ishida, Y.; Kulasekharan, R.; Shimada, T.; Takagi, S.; Ramamurthy, V. Efficient singlet-singlet energy transfer in a novel host-guest assembly composed of an organic cavitand, aromatic molecules, and a clay nanosheet. *Langmuir* **2013,** *29*, 1748-53.

14. Ogawa, M.; Kuroda, K., Photofunctions of Intercalation Compounds. *Chem. Rev.* **1995**, *95*, 399-438.

15 Thomas, J. K., Physical Aspects of Radiation-Induced Processes on SiO_2, γ-Al_2O_3, Zeolites, and Clays. *Chem. Rev.* **2005**, *105*, 1683–1734.

16 Takagi, K.; Shichi, T., Clay minerals as photochemical reaction fields. *J. Photochem. Photobiol. C: Photochem. Rev.* **2000**, *1*, 113-130.

17 Suib, Steven L., Zeolitic and layered materials. *Chem. Rev.* **1993**, *93*, 803–826.

18 Okada, T.; Ide, Y.; Ogawa, M. Organic–inorganic hybrids based on ultrathin oxide layers: designed nanostructures for molecular recognition. *Chemistry - an Asian journal* **2012**, *7*, 1980-1992.

19 Eguchi, M.; Watanabe, Y.; Ohtani, Y.; Shimada, T.; Takagi, S. Switching of energy transfer reaction by the control of orientation factor between porphyrin derivatives on the clay surface. *Tetrahedron Letters* **2014,** *55*, 2662-2666.

20 Miyamoto, N.; Kawai, R.; Kuroda, K., Ogawa, M., Adsorption and aggregation of a cationic cyanine dye on layered clay minerals. *Applied Clay Science*, **2000**, *16*, 161–170.

21 Neumann, M. G.; Gessner, F.; Schmitt, C. C.; Sartori, R., Influence of the Layer Charge and Clay Particle Size on the Interactions between the Cationic Dye Methylene Blue and Clays in an Aqueous Suspension. *J. Colloid and Interface Science*, **2002**, *255*, 254–259.

22 Bujdák, J., Effect of the layer charge of clay minerals on optical properties of organic dyes. A review. *Applied Clay Science*, **2006**, *34*, 58–73.

23 Schoonheydt, R. A., Smectite-type clay minerals as nanomaterials. *Clays and Clay Minerals*, **2002**, *50*, 411-420.

24 Bujdák, J.; Iyi, N.; Fujita, T., The aggregation of methylene blue in montmorillonite dispersions. *Clay Minerals*, **2002**, *37*, 121-133.

25 López Arbeloa, F.; Martínez Martínez, V.; Arbeloa, T.; López Arbeloa, I., Photoresponse and anisotropy of rhodamine dye intercalated in ordered clay layered films. *J. Photochem. Photobiol. C: Photochem. Rev.* **2007**, *8*, 85–108.

26 Kaschak, D. M.; Mallouk, T. E., Inter- and Intralayer Energy Transfer in Zirconium Phosphate-Poly(allylamine hydrochloride) Multilayers: An Efficient Photon Antenna and a Spectroscopic Ruler for Self-Assembled Thin Films. *J. Am. Chem. Soc.,* **1996**, *118*, 4222-4223

27 Hoppe, R.; Alberti, G.; Costantino, U.; Dionigi, C.; Schulz-Ekloff, G.; Vivani, R., Intercalation of Dyes in Layered Zirconium Phosphates. 1. Preparation and Spectroscopic Characterization of α-Zirconium Phosphate Crystal Violet Compounds. *Langmuir,* **1997**, *13*, 7252-7257

28 Kaschak, D. M.; Lean, J. T.; Waraksa, C. C.; Saupe, G. B.; Usami, H.; Mallouk, T. E., Photoinduced Energy and Electron Transfer Reactions in Lamellar Polyanion/Polycation Thin Films: Toward an Inorganic "Leaf". *J. Am. Chem. Soc.,* **1999**, *121*, 3435-3445

29 Klika, Z.; Weissmannová, H.; Čapková, P.; Pospíšil, M., The rhodamine B intercalation of montmorillonite. *J. Colloid Interface Sci*., 2004, 275, 243–250

30 Haiyan, W.; Daxiong, H.; Na, L.; Ke-An, L. Study on the intercalation and interlayer state of porphyrins into α-zirconium phosphate. *J. Inclusion Phenomena*, **2005**, *52*, 247-252.

31 Salleres, S., Arbeloa, F.L., Martínez, V., Arbeloa, T., Arbeloa, I.L. Adsorption of fluorescent R6G dye into organophilic C12TMA laponite films. *J. Colloid and Interface Sci.* **2008**, *321*, 212-219.

32 Sasai, R.; Iyi, N.; Fujita, T.; Lopez Arbeloa, F.; Martinez Martinez, V.; Takagi, K.; Itoh, H., Luminescence Properties of Rhodamine 6G Intercalated in Surfactant/Clay Hybrid Thin Solid Films. *Langmuir*, **2004**, *20*, 4715-4719.

33. Takagi, S.; Shimada, T.; Masui, D.; Tachibana, H.; Ishida, Y.; Tryk, D. A.; Inoue, H., Unique Solvatochromism of a Membrane Composed of a Cationic Porphyrin-Clay Complex. *Langmuir*, **2010**, *26*, 4639-4641.

34. Sumitani, M.; Takagi,. S.; Tanamura, Y.; Inoue, H., Oxygen Indicator Composed of an Organic Inorganic Hybrid Compound of Metylene Blue, Reductant, Surfactant and Saponite. *Analytical Sciences* **2004**, *20*, 1153-1157.

35. Suzuki, Y.; Tenma, Y.; Nishioka, Y.; Kamada, K.; Ohta, K.; Kawamata, J., Efficient Two-Photon Absorption Materials Consisting of Cationic Dyes and Clay Minerals. *J. Phys. Chem. C*, **2011**, *115*, 20653-20611.

36. Sasai, R.; Iyi, N.; Kusumoto, H.; Luminous Change of Rhodamine 3B Incorporated into Titanate Nanosheet/Decyltrimethylammonium Hybrids under Humid Atmosphere. *Bull. Chem. Soc. Jpn.,* **2011**, *84*, 562-568

37. Kuykendall, V. G.; Thomas, J. K., Photophysical investigation of the degree of dispersion of aqueous colloidal clay. *Langmuir*, **1990**, *6*, 1350-1356.

38. Chernia, Z.; Gill, D., Flattening of TMPyP Adsorbed on Laponite. Evidence in Observed and Calculated UV-vis Spectra. *Langmuir*, **1999**, *15*, 1625-1633.

39. Ishida, Y.; Masui, D.; Shimada, T.; Tachibana, H.; Inoue, H.; Takagi, S., The Mechanism of the Porphyrin Spectral Shift on Inorganic Nanosheets: The Molecular Flattening Induced by the Strong Host-Guest Interaction Due to the "Size-Matching Rule". *J. Phys. Chem. C*, **2012**, *116*, 7879–7885.

40. Walker, D. S.; Hellinga, H. W.; Saavedra, S. S.; Reichert, W. M., Integrated Optical Waveguide Attenuated Total Reflection Spectrometry and Resonance Raman Spectroscopy of Adsorbed Cytochrome c. *J. Phys. Chem.* **1993**, *97*, 10217-10222.

41. Harrick, N. J., Surface Chemistry from Spectral Analysis of Totally Internally Reflected Radiation. *J. Phys. Chem.* **1960**, *64*, 1110.

42. Harrick, N. J., Electric Field Strengths at Totally Reflecting Interface. *J. Opt. Soc. Am.* **1965**, *55*, 851-857.

43. Fringeli, U. P., The Structure of Lipids and Proteins Studied by Attenuated Total Reflection (ATR) Infrared sSectroscopy. II. Oriented Layers of a Homologous Series: Phosphatidylethanolamine to Phosphatidylcholine. *Z. Naturforsch., C: Biosci.* **1977**, *32*, 20-45.

44. Eguchi, M.; Tachibana, H.; Takagi, S.; Tryk; D. A.; Inoue, H., Dichroic Measurements on Dicationic and Tetracationic Porphyrins on Clay Surfaces with Visible-Light-Attenuated Total Reflectance. *Bull. Chem. Soc. Jpn.,* **2007**, *80*, 1350-1356.

45. Inagaki, S.; Ohtani, O.; Goto, Y.; Okamoto, K.; Ikai, M.; Yamanaka, K.; Tani, T.; Okada, T., Light Harvesting by a Periodic Mesoporous Organosilica Chromophore. *Angew. Chem., Ind. Ed.* **2009**, *48*, 4042–4046.

46. Miyatake, T.; Tamiaki, H.; Holzwarth, A. R.; Schaffner, K., Artificial Light-Harvesting Antennae: Singlet Excitation Energy Transfer from Zinc Chlorin Aggregate to Bacteriochlorin in Homogeneous Hexane Solution. *Photochem. Photobiol.* **1999**, *69*, 448–456.

47. Casey, J. P.; Bachilo, S. M.; Weisman, R. B., Efficient photosensitized energy transfer and near-IR fluorescence from porphyrin – SWNT complexes. *J. Mater. Chem.* **2008**, *18*, 1510–1516.

48. Kaschak, D. M.; Lean, J. T.; Waraksa, C. C.; Saupe, G. B.; Usami, H.; Mallouk, T. E., Photoinduced energy and electron transfer reactions in lamellar polyanion/polycation thin films: Toward an inorganic “leaf”. *J. Am. Chem. Soc.* **1999**, *121*, 3435–3445.

49. Takahashi, R.; Kobuke, Y., Hexameric Macroring of Gable-Porphyrins as a Light-Harvesting Antenna Mimic. *J. Am. Chem. Soc.* **2003**, *125*, 2372–2373.

50. Fujii, K.; Iyi, N.; Hashizume, H.; Shimomura, S.; Ando, T., Preparation of integrated coumarin/cyanine systems within interlayer of phyllosilicate and fluorescence resonance energy transfer. *Chem. Mater.* **2009**, *21*, 1179–1181.

51. Kuroda, T.; Fujii, K.; Sakoda, K., Ultrafast energy transfer in a multichromophoric layered silicate. *J. Phys. Chem. C* **2010**, *114*, 983–989.

52. Miller, M. A.; Lammi, R. K.; Prathapan, S.; Holten, D.; Lindsey, J. S., Synthesis and photophysical Properties of Light-Harvesting Arrays Comprised of a Porphyrin Bearing Multiple Perylene-Monoimide Accessory Pigments. *J. Org. Chem.* **2000**, *65*, 6634–6649.

53. Gilat, S. L.; Adronov, A.; Frechet, Jean, M. J., Light Harvesting and Energy Transfer in Novel Convergently Constructed Dendrimers. *Angew. Chem., Int. Ed.* **1999**, *38*, 1422–1427.

Chapter 6

Chromism of the transparent hybrid thin film composed from tetra cationic porphyrin and clay mineral depending on the relative humidity

6.1. Introduction

Photochemical or photo-physical behaviors of the organic molecules in the various host materials, such as micelle, clathrate, mesoporous materials, zeolites and nano-sheet materials have been investigated in several decades, and the guest organic molecules in the nano-spaces in these host materials shows interesting photo-physical and photochemical behaviors which are different from photochemical or photophysical behaviors in solution.[1-9] Especially, nano-sheet material is one of the interesting host materials because of their unique nano interlayer spaces, and the photophysical and photochemical properties of the guest molecule intercalated in the interlayer spaces of these layered materials have attracted great research interests.[10-16] One of the unique properties of this interlayer space is the control of the interlayer distance by the environment and guest molecules.[10,17-21] For example, the interlayer spaces of clay minerals, which is one of the typical inorganic layered materials, is depend on not only the guest molecules, but also the solvent, temperature and relative humidity.[22-29] It indicated that interlayer distance of the clay minerals can be controlled at nano order by these factors.

The change of the dye molecules geometrics can influence the photophysical behaviors, and the geometric of some dyes can be changed in the nano spaces in host materials.[30-35]

In our previous works, we have investigated the photochemical and photophysical properties of the dye adsorbed/intercalated on/in clay minerals, and Takagi and Kawamata groups reported that the some of the cationic dyes adsorbed on clay minerals surfaces shows the red shift of the absorption maximum, because the extension of the π-conjugated system of choromophore was induced by the co-planarization of chromophore and peripheral substituents.[11,36-38] Considering this investigation and dependency of the interlayer spaces of clay minerals on relative humidity, the absorption band of the intercalated dyes in clay minerals should be depend on the relative humidity, if molecular geometrics were changed by the interlayer spaces of clay nano-sheets which can be controlled by the relative humidity. It would be useful for the sensing devices for the detection of relative humidity, which is important parameter which needs to be measured or monitored in various chemical processes, such as in the food, electronics, and pharmaceutical industries.[39-56] In addition, typical organic molecules chromism was produced by structural change in chromophore involving cleavage of chemical bonds.[57-61] These intra-molecules' structural changes lead to the drastic color changes, but they are a frequent cause of the poor reversibility. On the other hand, chromism induced by soft molecular geometrics change without cleavage of covalent bond will be mild reaction, thus the chromism without cleavage of covalent would be expected to show the good reversibility. This highly reversibility requires for the sensing devices. In this chapter, we investigated that the spectral shift of the intercalated guest molecule in the interlayer space of the clay minerals depending on the relative humidity in air. Transparent hybrid film was prepared by the method developed

in chapter 5.[62] We examined to prepare the transparent hybrid film composed of magnesium tetrakis(1-methyl-4-pyridiniumyl)porphyrin (MgTMPyP) and Smecton SA (SSA) which is one of the typical clay minerals. The dependency of UV-Vis. absorption spectra of this hybrid film on relative humidity was investigated. Obtained hybrid film shows the reversible visible color change depending on the relative humidity.

6.2. Experimental section

Materials

$MgTMPyPCl_4$ was purchased from Mid-century, and purity was checked by 1H-NMR and thin layer chromatography. Smecton SA (SSA), which was used as a synthetic cation exchangeable clay mineral was purchased from Kunimine industry. The stoichiometric formula of SSA is $[(Si_{7.20}Al_{0.80})(Mg_{5.97}Al_{0.03})O_{20}(OH)_4]^{-0.77}(Na_{0.49}Mg_{0.14})^{+0.77}$, the theoretical surface area is 750 m^2 g^{-1}, and the cation exchangeable capacity (CEC) is 1.00 meq g^{-1}.[63,64] The average area per an anionic site is calculated to be 1.25 nm^2, and the average distance between anionic sites on the SSA sheets is estimated to be 1.2 nm on the basis of a hexagonal array. The glass substrate (cover glass, 24 mm × 24 mm, thickness is 0.145±0.025 mm) was purchased from Matsunami Glass IND., LTD. The structural image of MgTMPyP and SSA were shown in Figure 1.

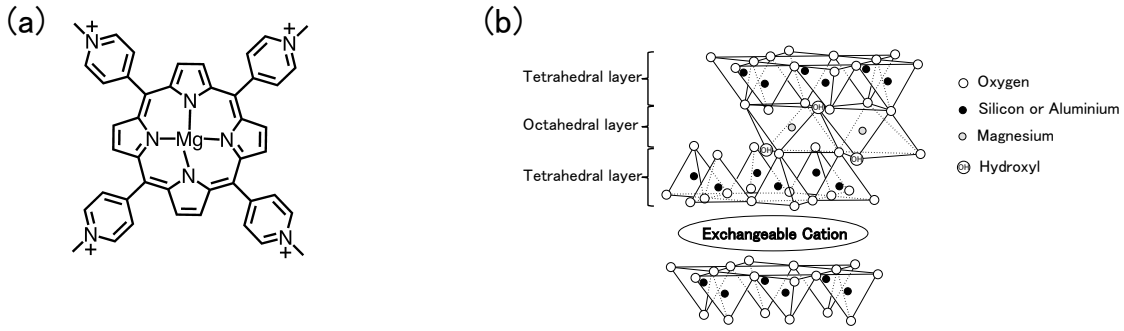

Figure 1. Structural image of tetrakis(1-methyl-4-pyridiniumyl)porphyrin (MgTMPyP(a)), Smecton SA (SSA, (b))

Preparation of SSA Film

The glass substrate was sonicated with water for 30 min and then treated in sulfuric acid (Kanto Chemical, 96%) overnight at room temperature. Then, the glass substrate was washed with enough water. 2 mL of SSA dispersion (100 mg L^{-1} in water:dioxane = 4:1 (v:v)) was filtered through a PTFE membrane filter (pore size = 0.1 μm). Because few SSA was observed in the filtrate, SSA was almost filtered (ca. 99%). The transparent SSA thin film was obtained by transferring the residue upon the glass substrate.[61,65] The thin film was dried up under vacuum overnight.

Preparation of Hybrid Film Composed of SSA and MgTMPyP

The hybrid films composed of SSA and MgTMPyP were prepared according to the literature.[62] The SSA thin films were immersed in water : ethanol = 1 : 2 (v : v) solution containing MgTMPyP for 48-72 h at room temperature with constant stirring.

Measurement of UV-Vis. Absorption Spectra at Each Relative Humidity Condition

Vapor pressure of the aqueous solution can be controlled by the solute, thus relative humidity in the closed container can be controlled by the saturated salt aqueous solution where presence in the container.[66] The image of the experiment system was shown in Figure 2.

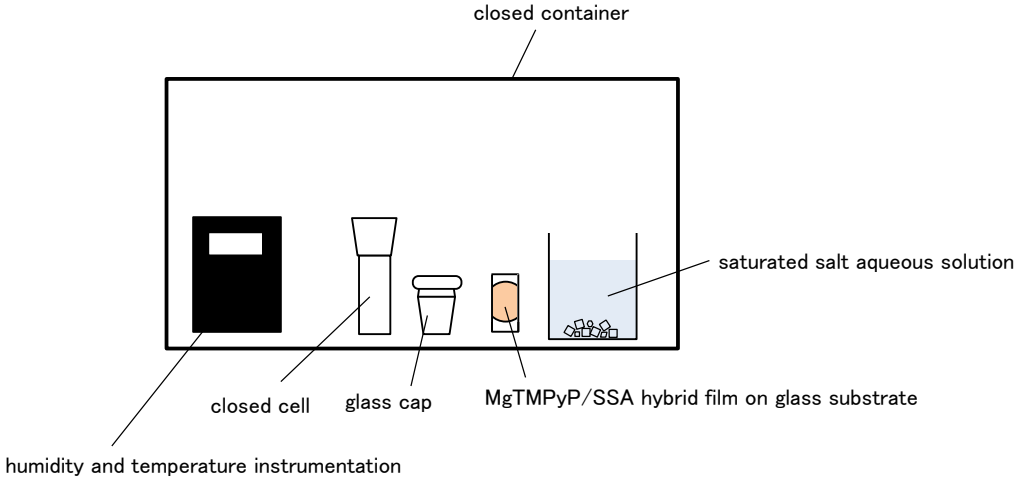

Figure 2. Image of the experiment system

Closed cap cell, glass cap, humidity and temperature instrumentation and hybrid film was treated in closed container in presence of saturated aqueous solution of the salt. The satulated salt aqueous solutions of ZnBr, $CaBr_2$, $MgBr_2$, $Zn(NO_3)_2$, $Ni(NO_3)_2$, NaBr, $Mg(C_2H_3O_2)_2$, $NaClO_3$, KBr, and Na_2HPO_4 were used to control the relative humidities. The relative humidities of the each saturated salt aqueous solutions were reported as 8.1%, 16.2%, 31.5%, 38.5%, 48.6%, 58%, 65%, 75%, 84%, and 95%, respectively. The relative humidity in closed container was monitored by humidity instrumentation. After relative humidity became constant over 1 H, hybrid film was set in the quartz cell, then

the quartz cell was closed with cap. In the case of low relative humidity condition, dried air was flowed in container. After that, the container was closed and stood until RH became constant over 1H. In the case of vacuum condition measurement, the closed cell was vacuated as shown in figure3.

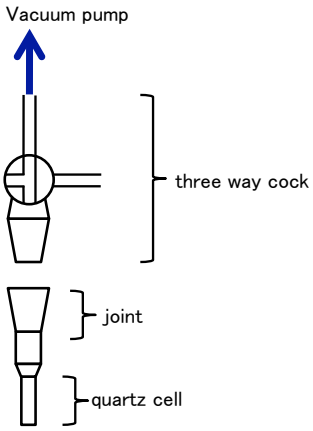

Figure 3. Image of the optical cuvette to measure the absorption spectra under vacuum condition

Analysis

UV-Vis. absorption spectra were obtained on Shimadzu UV-3150. The fluorescence spectra were measured with Jasco FP-6600 spectrofluorometer, and wavelength of excitation light was set at absorption maximum wavelength of the each sample. The glass substrate was set at 45 degree against the direction of excitation light source and the detector of emission as shown in Figure 4.

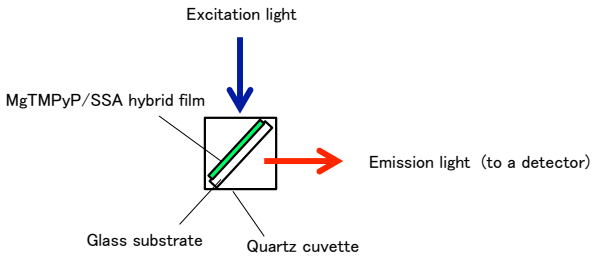

Figure 4. Layout image for fluorescence measurement (Top view)

The X-ray diffraction (XRD) pattern was measured with a RINT TTRIII(Rigaku).

6.3. Result and discussion

Intercalation reaction of MgTMPyP into interlayer space of SSA

The typical absorption spectral change of immersion solution between immersion process is shown in Figure 5.

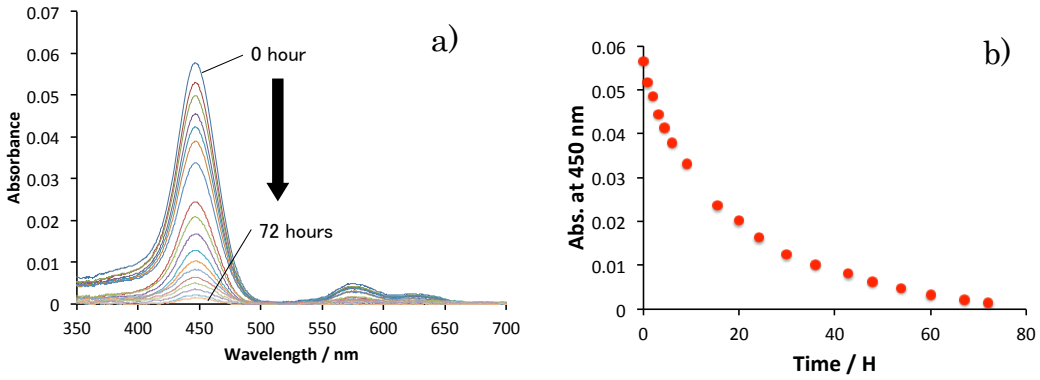

Figure 5. (a) Absorption spectral change of immersion solution (b) absorbance of MgTMPyP in solution at each time

MgTMPyP in solution was decreased in the immersion process, and color of SSA film were changed from colorless to green. It indicated that MgTMPyP adsorbed on SSA film. The MgTMPyP in solution were almost disappeared till 72 hours after, and ca. 94% MgTMPyP was decreased at each loading level. The exactly loading level of the MgTMPyP was determined by following equation,

$$\text{Loading level / \% versus CEC} = \{(C_0\text{-}C)\times V_i\times q_{Mg}\} /(M\times q_{SSA})\times 100 \quad \text{(eq. 1)}$$

where C_0 indicates initial concentration of MgTMPyP in immersion solution(mol L^{-1}), C is finally concentration of MgTMPyP immersed solution(mol L^{-1}), V_i indicates of the volume of immersion solution, q_{Mg} is valence of the MgTMPyP (4 eq / mol), M is the mass of the SSA (g) and q_{SSA} is cation exchange capacity of the SSA(1.00×10^{-3} eq g^{-1}). The mass of SSA (M) could be calculated by following equation 2.

$$M / g = V \times C \quad \text{(eq. 2)}$$

,where V indicates the volume of the filtered SSA dispersion (2 mL) and C is the concentration of filtered SSA dispersion (100 mg L^{-1}), respectively. The photograph of obtained hybrid film was shown in Figure 6.

Figure 6. Photograph of MgTMPyP/SSA hybrid film

As shown in Figure 6, the transparency of the obtained film is enough to measure the transmission spectra. The X-ray diffraction (XRD) patterns were carried out to determine the interlayer distances of SSA film and MgTMPyP/SSA hybrid films. XRD pattern of the SSA film and MgTMPyP/SSA hybrid film at each MgTMPyP loadings were shown in Figure 7.

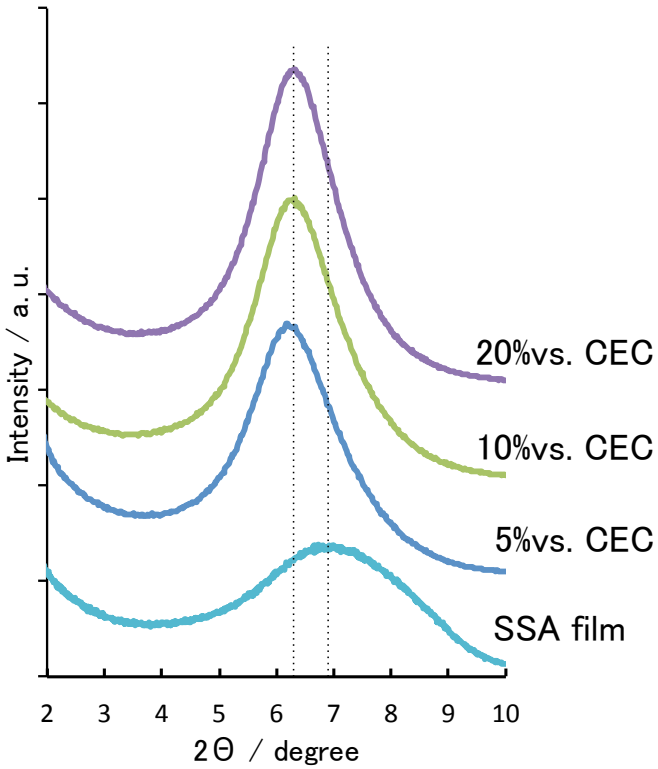

Figure 7. XRD pattern of the SSA film and MgTMPyP/SSA hybrid films at various MgTMPyP loadings.

The diffraction pattern of SSA film was observed at 6.9 degree, and this pattern well corresponds with the pattern of SSA (001). The interlayer distance of SSA nano-sheet in SSA film is calculated as 0.31 nm considering the thickness of the nano-sheet (0.97 nm). The diffraction patterns of the MgTMPyP/SSA hybrid films were shifted to low angle compared to the SSA only film. It indicated that the interlayer space of MgTMPyP/SSA hybrid films were extended because of the intercalation of MgTMPyP to the interlayer space of SSA nano-sheet. The interlayer space of SSA nano-sheet where MgTMPyP were intercalated was estimated as 0.45 nm. Considering the thickness of the porphyrin

ring (ca0.3-0.35 nm), MgTMPyP was not form the face-to-face type dimer (H-aggregate), thus MgTMPyP was intercalated between SSA nanosheets as monolayer. In addition, orientation of MgTMPyP intercalated in the SSA nano-sheets would be almost in parallel to the SSA nano-sheets. The interlayer distance where MgTMPyP was intercalated is longer compared to the interlayer distance of SSA where free-base porphyrin was intercalated (0.37-0.42 nm), in spite of the fact that the thickness of MgTMPyP and free base porphyrin is almost same. As described later, it may suggest that coplanarization of porphyrin ring and meso substituted pyridinium groups of MgTMPyP is weak compared to the free base porphyrin, because of the week adsorptivity of MgTMPyP.

UV-Vis. absorption and Fluorescence spectra of MgTMPyP/SSA hybrid film

The absorption spectra of MgTMPyP solution (without clay minerals), MgTMPyP adsorbed on exfoliated SSA surfaces, MgTMPyP/SSA hybrid film were shown in Figure 8.

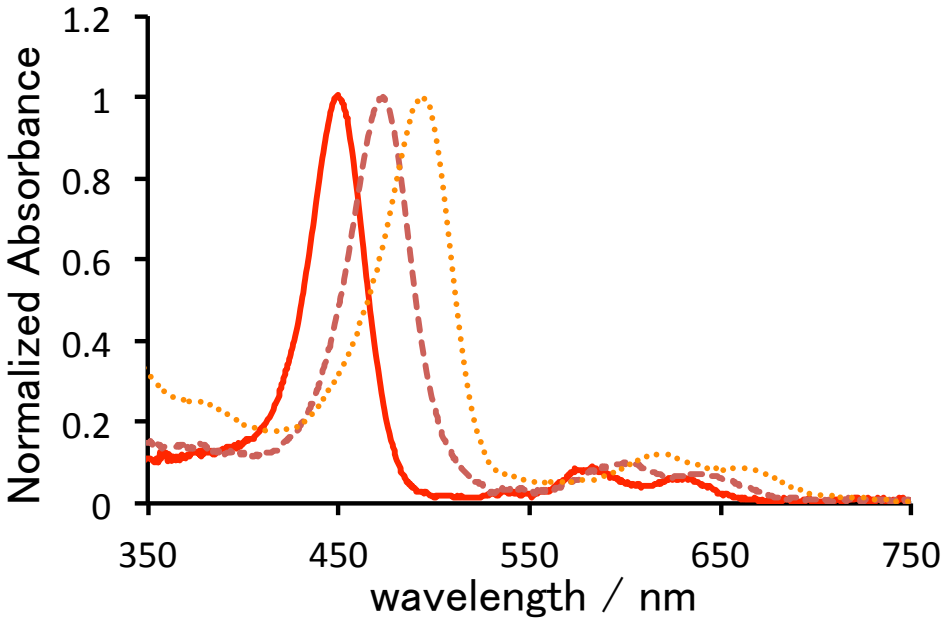

Figure 8. Normalized UV-Vis. absorption spectra of MgTMPyP solution(without SSA, solid line), MgTMPyP on exfoliated SSA surfaces (broken line), MgTMPyP/SSA fybrid film (dotted line)

The maximum absorption wavelength of MgTMPyP adsorbed on SSA surfaces was shifted to longer wavelength compared to the MgTMPyP solution(450 nm → 494 nm). This considerable spectral change would be ascribed to the coplanarization of the peripheral mesosubstituted pyridinium groups and the porphyrin ring on the SSA surfaces.[11,36-38] Also absorption spectra of MgTMPyP/SSA film, which MgTMPyP was intercalated into the interlayer space of SSA nano-sheet, shows further red shift compared to MgTMPyP adsorbed on SSA surfaces. It indicated that coplanarization of MgTMPyP intercalated in SSA nano-sheets was enhanced compared to the MgTMPyP

on SSA surfaces.[67] The absorption spectra of MgTMPyP/SSA hybrid films, which loading level of MgTMPyP was changed from 4.2 to 38.9% versus CEC were shown in Figure 9.

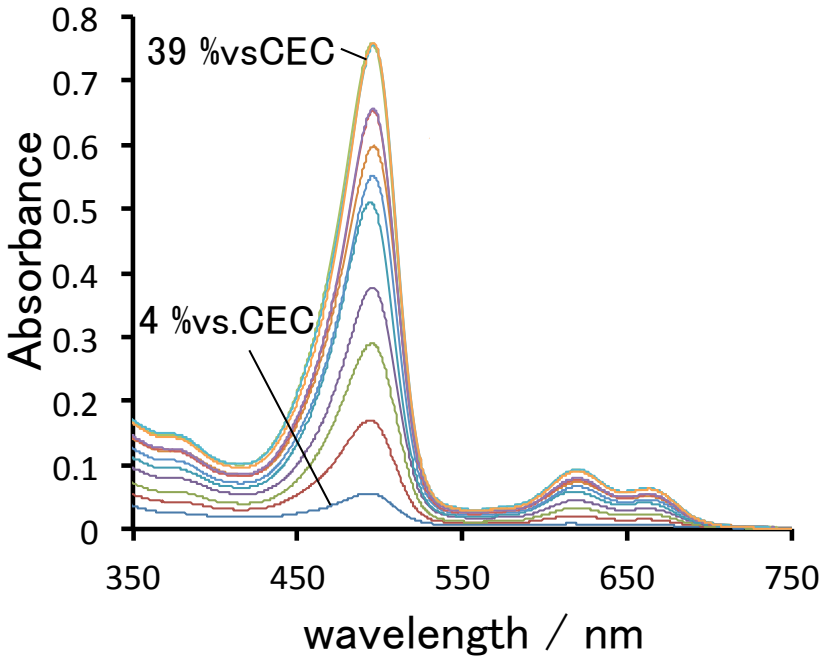

Figure 9. UV-Vis. absorption spectra of MgTMPyP/SSA hybrid films in which loading level of MgTMPyP were set at from 4.2 to 38.9% versus CEC.

The shapes of absorption spectra of each MgTMPyP/SSA hybrid films were not changed till 30% versus CEC of SSA as shown in figure 9. It indicated that MgTMPyP intercalated into SSA nano-sheets was not aggregated in the interlayer space, because complicated absorption spectral change due to the increase of MgTMPyP loadings would be observed if MgTMPyP were aggregated. The absorbance−loading level of MgTMPyP plot was shown in Figure 11.

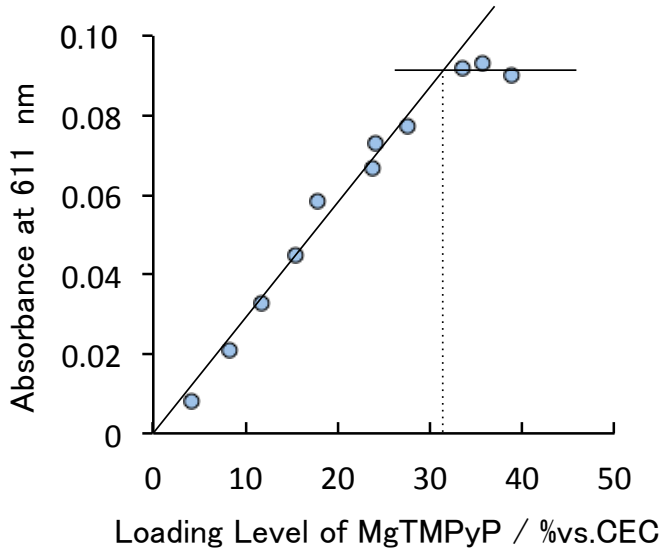

Figure 11. Absorbance−loading level of MgTMPyP plot of MgTMPyP/SSA hybrid film

The linearity of the plot in Figure 11 was kept until the 31% versus CEC, thus these results indicated that MgTMPyP was intercalated into interlayer space of SSA nano-sheet till 31% versus CEC without aggregation. The saturated adsorption amount without aggregation of MgTMPyP into SSA nano-sheet was estimated as 31% versus CEC. This saturated adsorption amount of MgTMPyP is lower than the saturated adsorption amount of the free base porphyrin, that is 5,10,15,20-tetrakis(*N*-methylpyridinium-4-yl)porphyrin into SSA film (35% versus CEC). The saturated adsorption amount of MgTMPyP and free base porphyrin on exfoliated SSA surfaces is 100 and 89% versus CEC, respectively. It suggested that adsorption force of free base porphyrin is stronger compared to MgTMPyP. We reported that electrostatic interaction between cation of the dye and anionic site on the

surfaces affects to the adsorption force of the dyes to the clay surfaces. Although diameter of Mg ion, which insert into porphyrin ring, is not large compared to the thickness the porphyrin, we consider that Mg ion and the axial ligand of Mg ion is avoid the approach of the cationic site to the anionic site on SSA sufaces because of their steric effect. The electrostatic interaction depends on the distance between anion and cation, thus adsorption force of the MgTMPyP is weaker compared to the free base porphyrin which does not have any steric hindrance. In addition, this weak electrostatic interaction between porphyrin molecules and clay surfaces would affect to the coplanarization of pyridinium ring and porphyrin ring. The shift of the maximum absorption wavelength of free base porphyrin due to the adsorption on/intercalation between SSA nano-sheet is larger compared to MgTMPyP, and the interlayer distance, and the interlayer distance of SSA where free base porphyrin was intercalated was shorter than in the case of MgTMPyP. These observations would support the difference of the electrostatic and adsorption strength between free base porphyrin and MgTMPyP. In fact, saturated adsorption amount of MgTMPyP on/in SSA surfaces was lower than the saturated adsorption amount of free base porphyrin. This relsust also suggested that absorption force of the MgTMPyP to SSA surfaces is weaker compared to fee base porphyrin. The Fluorescence spectra of MgTMPyP in solution, adsorbed on SSA surfaces, intercalated between SSA sheets were shown in Figure 12.

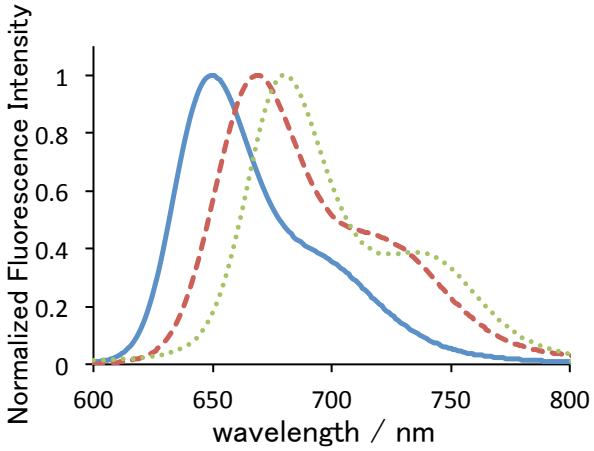

Figure 12. Normalized fluorescence spectra of MgTMPyP solution(without SSA, solid line), MgTMPyP on exfoliated SSA surfaces (broken line), MgTMPyP/SSA fybrid film (dotted line)

The fluorescence spectra of MgTMPyP adsorbed on/intercalated into SSA nano-sheets also showed the red shift which similar to absorption spectral shift. It would also be ascribed to the coplanarization of porphyrin ring and meso substituted pyridinium groups. In addition, fluorescence spectral shapes of MgTMPyP in each matrix are almost same, thus it suggested that new luminescence spices such as excimer and J-dimer (head-to-tail type dimer) was not formed in the interlayer space of SSA sheets.

Chromism of the MgTMPyP/SSA Hybrid Film Depending on Relative Humidity

To examine the reversible color change, which was called chromism, of MgTMPyP/SSA hybrid film depending on the relative humidity, absorption spectra of MgTMPyP/SSA hybrid film under each relative humidity condition were measured. The obtained normalized absorption spectra were shown in Figure 13.

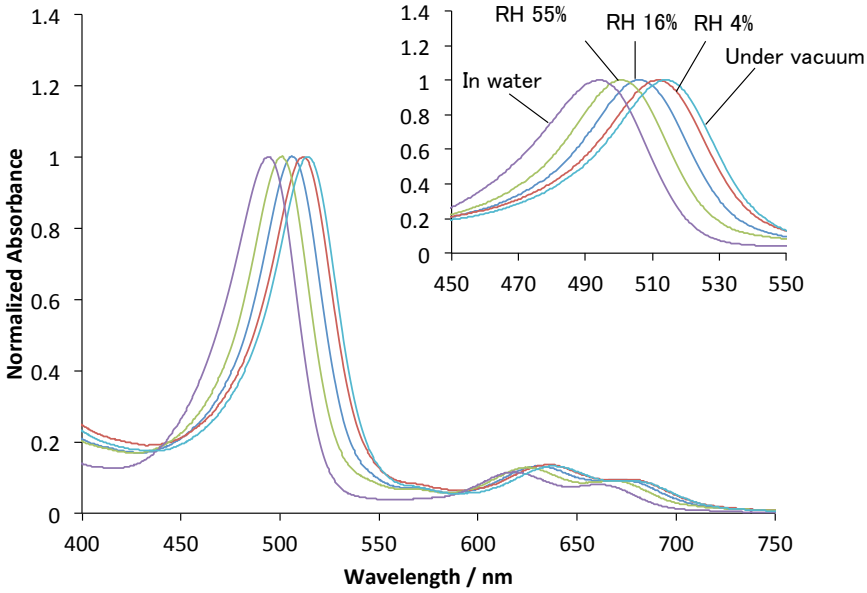

Figure 13. Normalized absorption spectra of MgTMPyP/SSA hybrid film at each relative humidity condition

Inset : ampliation of the Soret band

The maximum absorption wavelength of MgTMPyP/SSA hybrid film was depended on the RH as shown in Figure 13. The maximum absorption wavelength of MgTMPyP/SSA hybrid film was shifted to long wavelength (514 nm) under vacuum condition. Then the λ_{max} showed continuously blue shift with increasing of relative humidity. The relative humidty $-\lambda_{max}$ plot was shown in Figure 14.

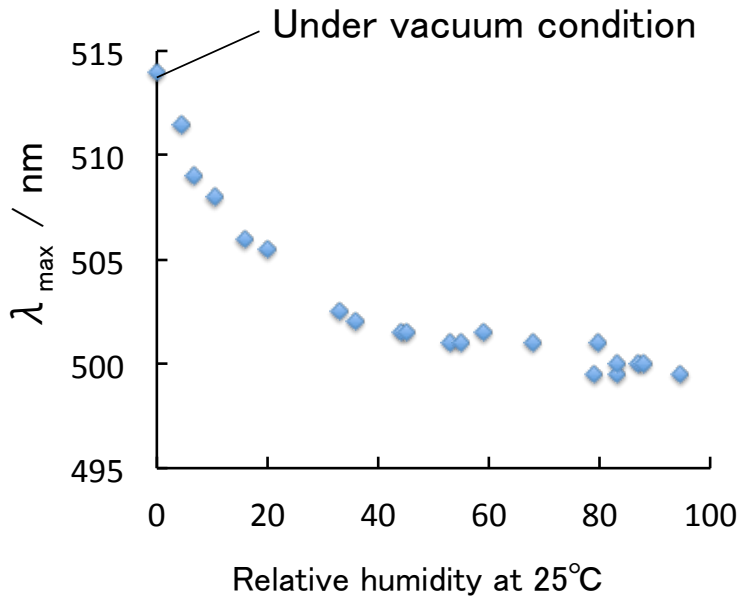

Figure 14.λ_{max} of MgTMPyP/SSA hybrid films under each RH condition.

As shown in Figure 14, the λmax of MgTMPyP was shifted to longer wavelength with increasing of the relative humidty continuously until ca. RH45%, then the λmax of the hybrid film was constant above relative humidity 45%. The photograph of MgTMPyP/SSA hybrid under each RH condition was shown in Figure 15.

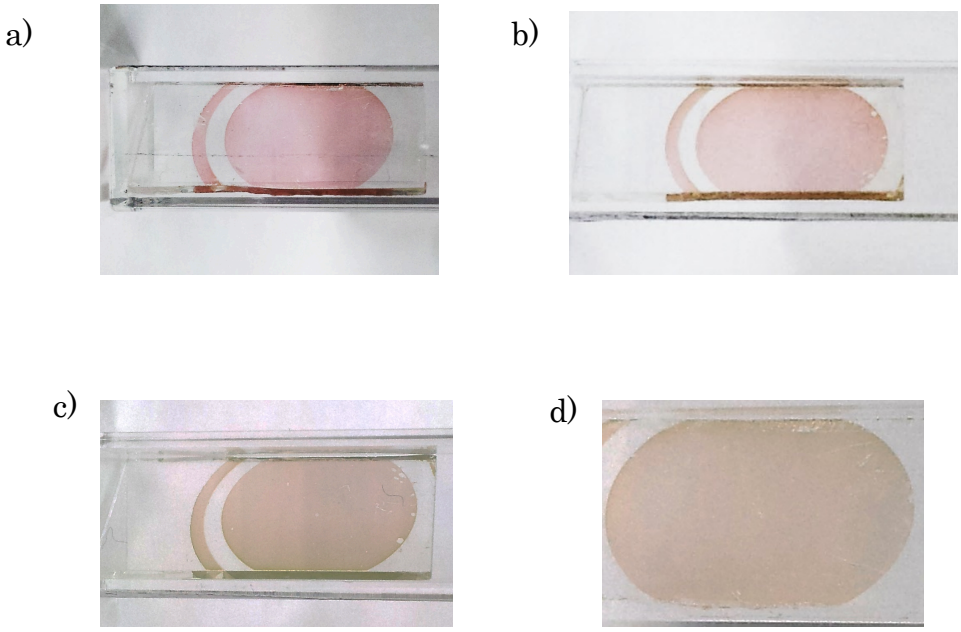

Figure 15. Photograph of MgTMPyP/SSA hybrid film under various RH condition (a) under vacuum condition, (b) relative humidity 4%, (c) relative humidity 26%, (d) in water

The color of MgTMPyP/SSA hybrid film was pink under vacuum condition (shown in Fiure 14-(a)). On the other hand, the color of this film was changed to pale orange under high relative humidity condition as shown in Figure 14-(c). In addition, color of the hybrid film under 26%, which was shown in Figure 14-(b), is different from the color of the film under vacuum and high relative humidity condition. These spectral shift and color change of the hybrid film is reversible. These observations indicated that there is a possibility this MgTMPyP/SSA hybrid film can be utilized as sensor for the relative humidity. Furthermore, this chromism of MgTMPyP/SSA hybrid film clearly observed by the increasing of the absorbance. The photograph of deep colored MgTMPyP/SSA hybrid film (thickness of the film was increased ca. 2 times compared to the

MgTMPyP/SSA hybrid film which was shown in Figure14) was shown in Figure 16.

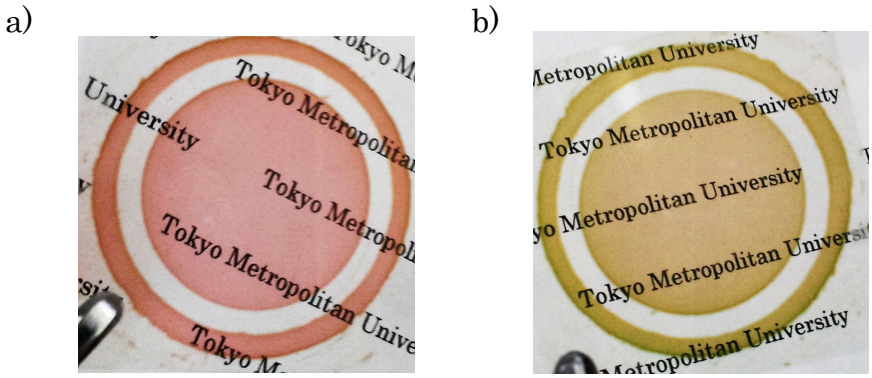

Figure 16. The chromism of the deep colored MgTMPyP/SSA hybrid film (a) under low relative humidity condition (b) under high relative humidity condition

As shown in Figure 16-(a), the color of MgTMPyP/SSA hybrid film was deep pink under low relative humidity condition, then the color of the deep colored hybrid film was changed to lime green under high relative humidity condition. The mechanism of this chromism would be ascribed to the change of coplanarization of the pyridinium group and porphyrin ring of MgTMPyP which was intercalated into the interlayer space of the SSA nano-sheets.[67] Interlayer distance of clay minerals depends on the relative humidity, and the interlayer distance was extended under high relative humidity condition compared to under low relative humidity or vacuum condition, because amount of interlayer water and number of hydrated water of cation, which was counter ion of anion on the clay surfaces, depend on the relative humidity. Considering this

phenomena, interlayer distance of SSA is narrow under low relative humidity or vacuum condition because of the less interlayer water, thus the coplanarization of MgTMPyP is strong, thus absorption spectra was shifted to longer wavelength. On the other hand, interlayer distance of SSA nano-sheet was extended under high relative humidity condition because of the rich interlayer water, thus coplanarization of MgTMPyP would be weak compared to the under low relative humidity condition. Thus, the absorption spectra of MgTMPyP showed the blue shifted compared to under low relative humidity condition. We believe above expected mechanism is the cause of the chromism of the MgTMPyP/SSA hybrid films depending on the relative humidity. The image of these expected mechanism was shown in Figure 17.

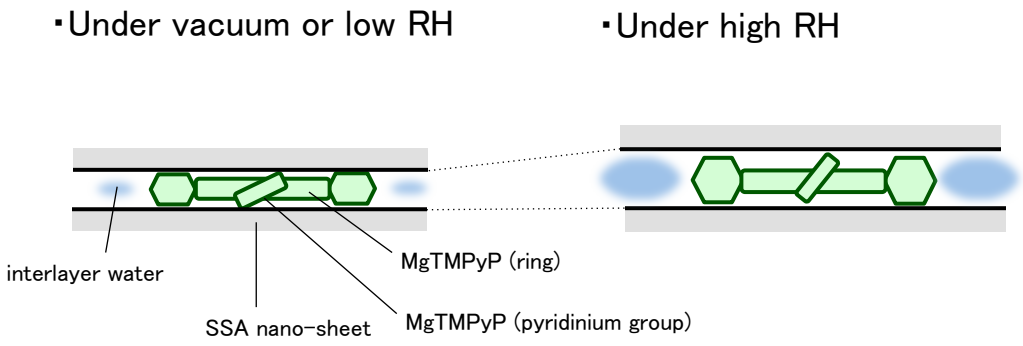

Figure 17. Image of the expected chromism mechanism of MgTMPyP/SSA hybrid film depending on the relative humidity

Vapochromism of the MgTMPyP /SSA Hybrid Film

To examine the chromism by the other vapor pressure of organic solvents, UV-Vis

absorption spectra of MgTMPyP under the saturated vapor of the organic solvent were demonstrated. The absorption spectra were measured in the closed cuvette as shown in Figure 18.

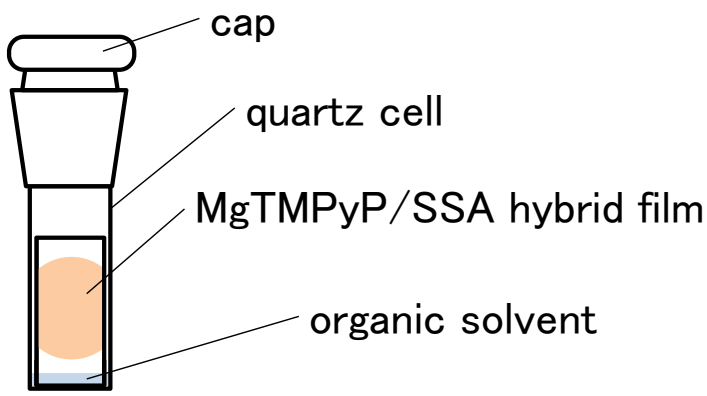

Figure 18. Image of the cuvette to measure the absorption spectra under various organic solvent vapor.

Ethanol, dichloromethane, hexane, acetonitrile, 1,4-dioxane and *N,N*-dimethylformamide was used as solvents. The photograph of the MgTMPyP under each organic solvent vapor was shown in Figure 19.

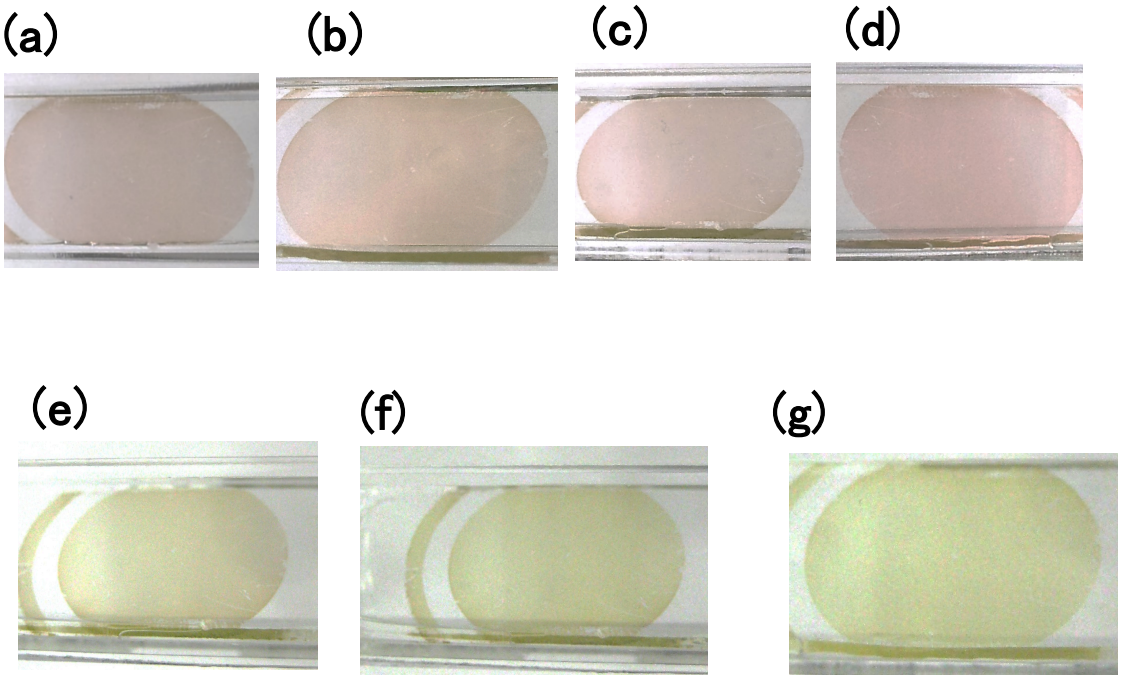

Figure 19. Photograph of MgTMPyP/SSA hybrid film under various organic solvent vapor, (a) water, (b) Ethanol, (c) dichloromethane (d) hexane, (e) acetonitrile, (f) 1,4-dioxane (g) *N,N*-dimethylformamide.

The color of MgTMPyP/SSA hybrid film under ethanol vapor was not changed, also the color of MgTMPyP/SSA hybrid film under vapor of methanol, acetone was not changed (not shown). On the other hand, color of the film was slightly changed under the hydrophobic solvent, such as dichloromethane and hexane. In addition, the color of this film was changed to green under acetonitrile, 1,4-dioxane, N,N-dimethylformamide. To discuss the mechanism of this color change, absorption spectra under these organic solvents vapors were measured. UV-Vis. absorption spectra of MgTMPyP/SSA hybrid film under various organic solvent vapors were shown in Figure 20.

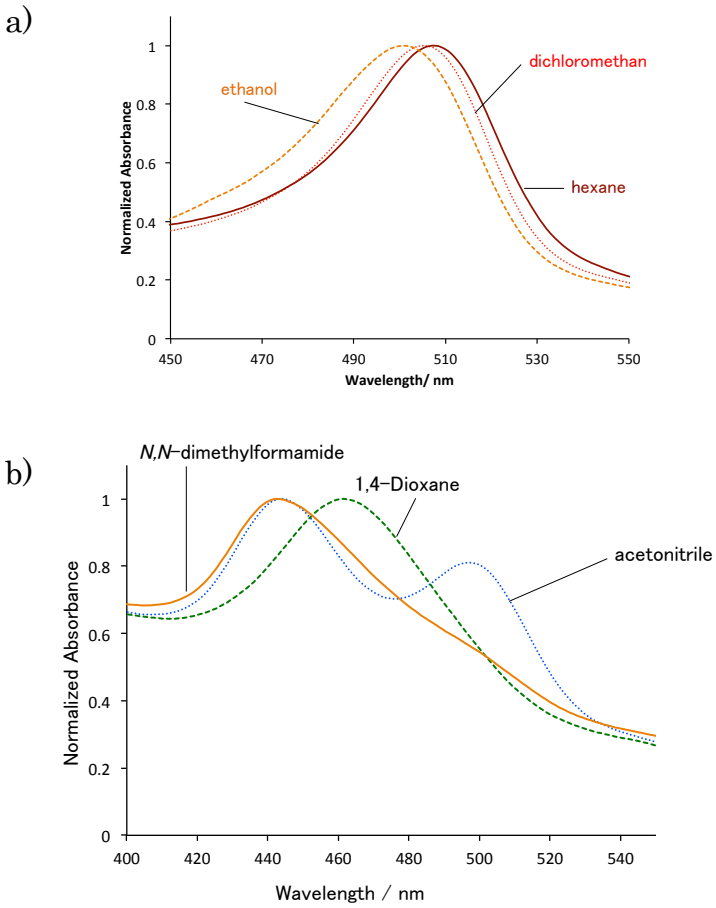

Figure 20. UV-Vis. absorption spectra

(a) under hexane (solid line), dichloromethane(dotted line) and ethanol (broken line) vapor

(b) acetonitrile (dotted line), 1,4-dioxane (broken line), N,N-dimethylformamide (solid line).

The maximum of absorption spectra of MgTMPyP/SSA hybrid under dichrolomethane and hexane vapor was almost same as under low humidity condition. It indicated that the coplanarization of the MgTMPyP was not changed. On the other hand, λ_{max} of MgTMPyP under ethanol vapor was almost unchanged from high relative humidity condition. It may suggest that hydrophobic solvents, such as dichloromethane and

hexane, were not inserted into the interlayer space of SSA nano-sheets. On the other hand, hydrophilic solvents such as alcohol could insert into interlayer space of SSA nano-sheets because surfaces and counter cation of the SSA is hydrophilic. Interestingly, the absorption spectra of MgTMPyP/SSA hybrid film under acetonitrile, 1,4-dioxane and *N,N*-dimethylformamide showed the drastic spectral changes compared to ethanol, dichloromethane and hexane vapor, and λmax of MgTMPyP/SSA hybrid film under *N,N*-dimethylformamide and acetonitrile was 445 nm. We reported that orientation of the porphyrin molecules adsorbed on the exfoliated SSA surfaces have been changed with addition of the organic solvents, and absorption maximum of porphyrin whose orientation was changed was shifted to shorter wavelength because coplanarization of porphyrin molecules was released. The spectral change, which was shown in Figure 19-(b), is similar to the orientation change of the porphyrin molecules on exfoliated clay surfaces. It is supposed that orientation of the MgTMPyP intercalated into the interlayer space of SSA nano-sheet were changed by the organic solvent vapor, and the coplanarization of porphyrin ring and meso substituted pyridinium groups was released, thus absorption maximum of MgTMPyP were shifted to shorter wavelength. However, The absorption spectrum of MgTMPyP under acetonitrile vapor has two absorption maximum at 445 nm and 500 nm. The absorption band at ca. 500 nm, which would be ascribed to MgTMPyP whose orientation was not changed, suggests the presence of MgTMPyP whose orientation was not changed. The orientation change of MgMTPyP or free base porphyrin is very similar to the orientation change behavior of porphyrin molecules adsorbed on exfoliated SSA surfaces.[69-72] This orientation change would be

related to the donor number, acceptor number and hydrogen bond parameter of the organic solvents. However, we supposed that there are not orientation change but also swelling of the interlayer space of SSA nano-sheets to change the absorption spectra of intercalated porphyrin molecules, and these phenomena (orientation change of porphyrin molecules and swelling of SSA) would depend on the different parameter. I cannot reveal what is the most important parameter to change the orientation of porphyrin molecules and what is depended on to change the interlayer distance of the SSA nano-sheets. We supposed that the fundamental controlling factor to change the orientation of porphyrin molecules adsorbed on/intercalated between SSA nano-sheets would revealed by our future works.

6.4. Conclusion

This chapter concerned with the functionality of hybrid transparent thin film composed of magnesium-tetracationic porphyrin and clay minerals, which is one of the inorganic layered materials. This hybrid film showed chromism depending on the relative humidity. The color of this hybrid film was changed form pink to orange with increasing of relative humidity, then absorption maximum due to Soret band of intercalated MgTMPyP was shifted from 514 nm to 501 nm respectively. In the case of bathochromic film, the visual color changes of those films were clearly observed compared to diluted film. This chromism depends on softly structural change of the intercalated MgTMPyP. This hybrid film would be useful as sensing device for relative humidity.

6.5. Reference

1. Calzaferri, G.; Huber, S.; Maas, H.; Minkowski, C. Host-guest antenna materials. *Angew. Chem. Int. Ed.* **2003,** *42*, 3732-58.

2. Fukuoka, A.; Miyata, H.; Kuroda, K. Alignment control of a cyanine dye using a mesoporous silica film with uniaxially aligned mesochannels. *Chem. Comm.* **2003**, 284-285.

3. Sasai, R.; Itoh, T.; Ohmori, W.; Itoh, H.; Kusunoki, M. Preparation and Characterization of Rhodamine 6G/Alkyltrimethylammonium/Laponite Hybrid Solid Materials with Higher Emission Quantum Yield. *J. Phys. Chem. C* **2009,** *113*, 415-421.

4. Nakato, T.; Kuroda, K.; Kato, C. Syntheses of intercalation compounds of layered niobates with methylviologen and their photochemical behavior. *Chem. Mater.* **1992,** *4*, 128-132.

5. Sarkar, M.; Sengupta, P. K. Influence of different micellar environments on the excited-state proton-transfer luminescence of 3-hydroxyflavone. *Chem. Phys. Lett.* **1991,** *179*, 68-72.

6. Turro, N. J.; Barton, J. K.; Tomalia, D. A. Molecular recognition and chemistry in restricted reaction spaces. Photophysics and photoinduced electron transfer on the surfaces of micelles, dendrimers, and DNA. *Acc. Chem. Res.* **1991,** *24*, 332-340.

7. Ihmels, H.; Faulhaber, K.; Vedaldi, D.; Dall'Acqua, F.; Viola, G. Intercalation of organic dye molecules into double-stranded DNA. Part 2: the annelated quinolizinium ion as a structural motif in DNA intercalators. *Photochem. Photobiol.* **2005,** *81*, 1107-15.

8. Monti, S.; Flamigni, L.; Martelli, A.; Bortolus, P. Photochemistry of benzophenone-cyclodextrin inclusion complexes. *J. Phys. Chem.* **1988,** *92*, 4447-4451.

9. Samanta, S. R.; Parthasarathy, A.; Ramamurthy, V. Supramolecular control during triplet sensitized geometric isomerization of stilbenes encapsulated in a water soluble organic capsule. *Photochem. & photobiolog. Sci. : Official journal of the European Photochemistry Association and the European Soc. for Photobiol.* **2012,** *11*, 1652-60.

10. Nabetani, Y.; Takamura, H.; Hayasaka, Y.; Sasamoto, S.; Tanamura, Y.; Shimada, T.; Masui, D.; Takagi, S.; Tachibana, H.; Tong, Z.; Inoue, H. An artificial muscle model unit based on inorganic nanosheet sliding by photochemical reaction. *Nanoscale* **2013,** *5*, 3182-3193.

11. Suzuki, Y.; Tenma, Y.; Nishioka, Y.; Kamada, K.; Ohta, K.; Kawamata, J. Efficient Two-Photon Absorption Materials Consisting of Cationic Dyes and Clay Minerals. *J. Phys. Chem. C* **2011,** *115*, 20653-20661.

12. Sasai, R.; Iyi, N.; Fujita, T.; Arbeloa, F. L.; Martínez; Takagi, K.; Itoh, H. Luminescence Properties of Rhodamine 6G Intercalated in Surfactant/Clay Hybrid Thin Solid Films. *Langmuir* **2004,** *20*, 4715-4719.

13. Santiago, M. B.; Declet-Flores, C.; Diaz, A.; Velez, M. M.; Bosques, M. Z.; Sanakis, Y.; Colon, J. L. Layered inorganic materials as redox agents: ferrocenium-intercalated zirconium phosphate. *Langmuir* **2007,** *23*, 7810-7.

14. Kaschak, D. M.; Lean, J. T.; Waraksa, C. C.; Saupe, G. B.; Usami, H.; Mallouk, T. E. Photoinduced Energy and Electron Transfer Reactions in Lamellar

Polyanion/Polycation Thin Films: Toward an Inorganic "Leaf". *J. Am. Chem. Soc.* **1999,** *121*, 3435-3445.

15. Usami, H.; Nakamura, T.; Makino, T.; Fujimatsu, H.; Shinji Ogasawara, a. Sensitized photoisomerization of cis-stilbazoliumions intercalated in saponite clay layers. *J. Chem. Soc., Faraday Trans.* **1998,** *94*, 83-87.

16. Martinez Martinez, V.; Lopez Arbeloa, F.; Banuelos Prieto, J.; Lopez Arbeloa, I. Characterization of rhodamine 6G aggregates intercalated in solid thin films of laponite clay. 2 Fluorescence spectroscopy. *J Phys. Chem. B* **2005,** *109*, 7443-50.

17. Sasaki, T.; Watanabe, M. Osmotic Swelling to Exfoliation. Exceptionally High Degrees of Hydration of a Layered Titanate. *J. Am. Chem. Soc.* **1998,** *120*, 4682-4689.

18. Li, L.; Ma, R.; Ebina, Y.; Iyi, N.; Sasaki, T. Positively Charged Nanosheets Derived via Total Delamination of Layered Double Hydroxides. *Chem. Mater.* **2005,** *17*, 4386-4391.

19. Liu, Z.; Ma, R.; Osada, M.; Iyi, N.; Ebina, Y.; Takada, K.; Sasaki, T. Synthesis, anion exchange, and delamination of Co-Al layered double hydroxide: assembly of the exfoliated nanosheet/polyanion composite films and magneto-optical studies. *J. Am. Chem. Soc.* **2006,** *128*, 4872-4880.

20. Wang, T.; Henderson, C. N.; Draskovic, T. I.; Mallouk, T. E. Synthesis, Exfoliation, and Electronic/Protonic Conductivity of the Dion–Jacobson Phase Layer Perovskite $HLa_2TiTa_2O_{10}$. *Chem. Mater.* **2014,** *26*, 898-906.

21. Chiou, C. T.; Rutherford, D. W. Effects of exchanged cation and layer charge

on the sorption of water and EGME vapors on montmorillonite clays. *Clay. Clay Miner.* **1997,** *45*, 867-880.

22. Farmer, V. C.; Russell, J. D. Interlayer complexes in layer silicates. The structure of water in lamellar ionic solutions. *T. Faraday Soc.* **1971,** *67*, 2737-2749.

23. Ravina, I.; Low, P. F. Change of b-Dimension with Swelling of Montmorillonite. *Clay. Clay Miner.* **1977,** *25*, 201-204.

24. Odom, J. W.; Low, P. F. Relation between Swelling, Surface Area and b Dimension of Na-Montmorillonites. *Clay. Clay Miner.* **1978,** *26*, 345-351.

25. Hawkins, R. H. Interfacial Water Structure in Montmorillonite from Neutron Diffraction Experiments. *Clay. Clay Miner.* **1980,** *28*, 19-28.

26. Fukushima, Y. X-Ray Diffraction Study of Aqueous Montmorillonite Emulsions. *Clay. Clay Miner.* **1984,** *32*, 320-326.

27. Olejnik, S. The Intercalation of Polar Organic Compounds into Kaolinite. *Clay Miner.* **1970,** *8*, 421-434.

28. Brindley, G. W. Clay- Organic Studies X. Complexes Of Primary Amines With Montmorillonite And Vermiculite. *Clay Miner.* **1965,** *6*, 91-96.

29. Ruiz-Hitzky, E.; Casal, B.; Aranda, P.; Galvan, J. Inorganic-organic nanocomposite materials based on macrocyclic compounds. *Rev. Inorg. Chem.* **2001,** *21*, 125-159.

30. Yang, S.-C.; Graupner, W.; Guha, S.; Puschnig, P.; Martin, C.; Chandrasekhar, H.; Chandrasekhar, M.; Leising, G.; Ambrosch-Draxl, C.; Scherf, U. Geometry-Dependent Electronic Properties of Highly Fluorescent Conjugated

Molecules. *Phys. Rev. Lett.* **2000,** *85*, 2388-2391.

31. Becker, H. D.; Andersson, K. On the relationship between molecular geometry and excited-state properties of 9-anthrylalkenes. *J. Org. Chem.* **1983,** *48*, 4542-4549.

32. Hall, L. H.; Orchard, B. J.; Tripathy, S. K. The structure and properties of flavins: Molecular orbital study based on totally optimized geometries. I. Molecular geometry investigations. *Int. J. Quantum Chem.* **1987,** *31*, 195-216.

33. Ishchenko, A. A. Structure and spectral-luminescent properties of polymethine dyes. *Russ. Chem. Rev.* **1991,** *60*, 865-884.

34. Sato, O. Optically switchable molecular solids: photoinduced spin-crossover, photochromism, and photoinduced magnetization. *Acc. Chem. Res.* **2003,** *36*, 692-700.

35. Grenthe, I.; Paoletti, P.; Sandstroem, M.; Glikberg, S. Thermochromism in copper(II) complexes. Structures of the red and blue-violet forms of bis(N,N-diethylethylenediamine)copper(II) perchlorate and the nonthermochromic violet bis(N-ethylethylenediamine)copper(II) perchlorate. *Inorg. Chem.* **1979,** *18*, 2687-2692.

36. Ishida, Y.; Masui, D.; Shimada, T.; Tachibana, H.; Inoue, H.; Takagi, S. The Mechanism of the Porphyrin Spectral Shift on Inorganic Nanosheets: The Molecular Flattening Induced by the Strong Host–Guest Interaction due to the “Size-Matching Rule”. *J. Phys. Chem. C* **2012,** *116*, 7879-7885.

37. Kuykendall, V. G.; Thomas, J. K. Photophysical investigation of the degree of dispersion of aqueous colloidal clay. *Langmuir* **1990,** *6*, 1350-1356.

38. Chernia, Z.; Gill, D. Flattening of TMPyP Adsorbed on Laponite. Evidence in Observed and Calculated UV−vis Spectra. *Langmuir* **1999,** *15*, 1625-1633.

39. Ballantine, D. S.; Wohltjen, H. Optical waveguide humidity detector. *Anal. Chem.* **1986,** *58*, 2883-2885.

40. Boltinghouse, F.; Abel, K. Development of an optical relative humidity sensor. Cobalt chloride optical absorbency sensor study. *Anal. Chem.* **1989,** *61*, 1863-1866.

41. Sadaoka, Y.; Sakai, Y.; Murata, Y.-u. Optical humidity and ammonia gas sensors using Reichardt's dye-polymer composites. *Talanta* **1992,** *39*, 1675-1679.

42. Otsuki, S.; Adachi, K. Characterization of Nafion solutions and films and observation of the casting process using basic dyes as optical probes. *J. Appl. Polym. Sci.* **1995,** *56*, 697-705.

43. Ando, M.; Kobayashi, T.; Haruta, M. Humidity-sensitive optical absorption of Co_3O_4 film. *Sensors Actuators B: Chem.* **1996,** *32*, 157-160.

44. Barkauskas, J. Investigation of conductometric humidity sensors. *Talanta* **1997,** *44*, 1107-1112.

45. Feng, C.-D.; Sun, S.-L.; Wang, H.; Segre, C. U.; Stetter, J. R. Humidity sensing properties of Nation and sol-gel derived SiO_2/Nafion composite thin films. *Sensors Actuators B: Chem.* **1997,** *40*, 217-222.

46. John, S. A.; Ramaraj, R. Regulation of dye assembly within wet and dry nafion films. *J. Appl. Polym. Sci.* **1997,** *65*, 777-787.

47. Meanna Pérez, J. M.; Freyre, C. A poly(ethyleneterephthalate)-based humidity sensor. *Sensors Actuators B: Chem.* **1997,** *42*, 27-30.

48. Qu, W.; Meyer, J.-U. A novel thick-film ceramic humidity sensor. *Sensors Actuators B: Chem.* **1997,** *40*, 175-182.

49. Brook, T. E.; Narayanaswamy, R. Polymeric films in optical gas sensors1Invited paper at Europt(r)ode IV Conference.1. *Sensors Actuators B: Chem.* **1998,** *51*, 77-83.

50. Raimundo Jr, I. M.; Narayanaswamy, R. Evaluation of Nafion–Crystal Violet films for the construction of an optical relative humidity sensor. *Analyst* **1999,** *124*, 1623-1627.

51. Patil, P. S. Gas-chromism in ultrasonic spray pyrolyzed tungsten oxide thin films. *B. Mater. Sci.* **2000,** *23*, 309-312.

52. Somani, P. R.; Viswanath, A. K.; Aiyer, R. C.; Radhakrishnan, S. Charge transfer complex-forming dyes incorporated in solid polymer electrolyte for optical humidity sensing. *Sensors Actuators B: Chem.* **2001,** *80*, 141-148.

53. Mastuzaki, H.; Kishida, H.; Okamoto, H.; Takizawa, K.; Matsunaga, S.; Takaishi, S.; Miyasaka, H.; Sugiura, K.; Yamashita, M. Vapochromic behavior accompanied by phase transition between charge-polarization and charge-density-wave states in a quasi-one-dimensional iodine-bridged dinuclear platinum compound. *Angew. Chem.* **2005,** *44*, 3240-3243.

54. Reichardt, C. Pyridinium-N-phenolate betaine dyes as empirical indicators of solvent polarity: Some new findings. *Pure and Appl. Chem.* **2008,** *80,* 1415–1432.

55. Shinbo, K.; Otuki, S.; Kanbayashi, Y.; Ohdaira, Y.; Baba, A.; Kato, K.; Kaneko, F.; Miyadera, N. A hybrid humidity sensor using optical waveguides on a

quartz crystal microbalance. *Thin Solid Films* **2009,** *518*, 629-633.

56. Kato, R.; Kide, K.; Hattori, T.; Wakahara, A.; Yamaguchi, M. Detection of Moisture in Oil Using Evanescent Absorption from Sapphire Optical Waveguide Coated with Co-Doped Silica Film. *Anal. Lett.* **2011,** *44*, 577-584.

57. Maeda, K.; Hayashi, T. Photochromic Color Change of the Dimer of Triphenylimidazolyl at Low Temperatures. *Bull. Chem. Soc. Jpn.* **1969,** *42*, 3509-3514.

58. Maeda, K.; Hayashi, T. The Mechanism of Photochromism, Thermochromism and Piezochromism of Dimers of Triarylimidazolyl. *Bull. Chem. Soc. Jpn.* **1970,** *43*, 429-438.

59. Shida, T.; Maeda, K.; Hayashi, T. Optical and ESR Studies on Triphenylimidazolyl Radicals Produced by Photolysis and Radiolysis at Low Temperature. *Bull. Chem. Soc. Jpn.* **1970,** *43*, 652-657.

60. Lukyanov, B. S.; Lukyanova, M. B. Spiropyrans: Synthesis, Properties, and Application. (Review). *Chem. Heterocyc. Compd.* **2005,** *41*, 281-311.

61. Laarhoven W. H. *Photochromism: Molecules and Systems,* Durr, H.; Bouas-Laurent , H. , Eds.; Elsevier, Amsterdam, **1990.** Chapter 7.

62. Fujimura, T.; Shimada, T.; Hamatani, S.; Onodera, S.; Sasai, R.; Inoue, H.; Takagi, S. High density intercalation of porphyrin into transparent clay membrane without aggregation. *Langmuir* **2013,** *29*, 5060-5065.

63. Egawa, T.; Watanabe, H.; Fujimura, T.; Ishida, Y.; Yamato, M.; Masui, D.; Shimada, T.; Tachibana, H.; Yoshida, H.; Inoue, H.; Takagi, S. Novel methodology to control the adsorption structure of cationic porphyrins on the clay surface using the

"size-matching rule". *Langmuir* **2011,** *27*, 10722-10729.

64. Takagi, S.; Tryk, D. A.; Inoue, H. Photochemical energy transfer of cationic porphyrin complexes on clay surface. *J. Phys. Chem. B* **2002,** *106*, 5455-5460.

65. Kawamata, J.; Suzuki, Y.; Tenma, Y. Fabrication of clay mineral–dye composites as nonlinear optical materials. *Philos. Mag.* **2010,** *90*, 2519-2527.

66. Arai, C.; Wakabayashi, Y.; Mizuno, A.; Komatsu, I.; Sano, Y. *Kagaku kogaku ronbunsyu,* The Society of Chemical Engineers **1983**, *9*, 241-244, and reference there in.

67. Eguchi, M.; Tachibana, H.; Takagi, S.; Inoue, H. Microscopic structures of adsorbed cationic porphyrins on clay surfaces: molecular alignment in artificial light-harvesting systems. *Res. Chem. Intermediat.* **2007,** *33*, 191-200.

68. Takagi, S.; Shimada, T.; Eguchi, M.; Yui, T.; Yoshida, H.; Tryk, D. A.; Inoue, H. High-density adsorption of cationic porphyrins on clay layer surfaces without aggregation: The size-matching effect. *Langmuir* **2002,** *18*, 2265-2272.

69. Eguchi, M.; Tachibana, H.; Takagi, S.; Tryk, D. A.; Inoue, H. Dichroic Measurements on Dicationic and Tetracationic Porphyrins on Clay Surfaces with Visible-Light-Attenuated Total Reflectance. *Bull. Chem. Soc. Jpn.* **2007,** *80*, 1350-1356.

70. Eguchi, M.; Takagi, S.; Inoue, H. The Orientation Control of Dicationic Porphyrins on Clay Surfaces by Solvent Polarity. *Chem. Lett.* **2006,** *35*, 14-15.

71. Takagi, S.; Eguchi, M.; Tryk, D.; Inoue, H. Porphyrin photochemistry in inorganic/organic hybrid materials: Clays, layered semiconductors, nanotubes, and mesoporous materials. *J. Photochem. Photobiol. C* **2006,** *7*, 104-126.

72. Takagi, S.; Shimada, T.; Masui, D.; Tachibana, H.; Ishida, Y.; Tryk, D. A.; Inoue, H. Unique solvatochromism of a membrane composed of a cationic porphyrin-clay complex. *Langmuir* **2010,** *26*, 4639-4641.

Chapter 7

Energy Transfer and Subsequent Electron Transfer between Assembled Dyes on the Clay Surfaces

7.1. Introduction

Natural photosynthesis in plants has been one of the most interesting topics in science because of not only their functionality, which is a conversion of photo-energy to chemical energy, but also their mechanism to realize the efficient light harvesting, charge separation and chemical reactions.[1-4] In an initial process of natural photosynthesis, energy of the sunlight is collected and is transferred to reaction center by light harvesting system with energy transfer reaction.[5-12] Then subsequent electron transfer reaction proceeds in the reaction center by accepting excited energy from light harvesting system. These flow controlled photochemical reaction is supposed to be realized by optimized photochemical properties of dyes and an appropriate spatial arrangement of dyes.[4,6,7] Both energy and electron transfer reaction have attracted great interest and have been investigated theoretically and experimentally.[13-28] In covalently linked system, the conjugation of energy transfer reaction and electron transfer reaction has been examined as a model system mimicking natural photosynthesis.[29-34] On the other hand, there are few reports on their conjugation especially in supramolecular systems. In recent years, it is revealed that the light-harvesting system is composed of well-organized hundreds of chlorophyll molecules.[6,7] To realize such practical light harvesting systems, supramolecular systems seem to be essential. Inspired by this idea,

a construction of arranged assembly of functional dyes has been investigated to achieve artificial light-harvesting system in supramolecular assemblies of organic molecules. In recent years, we have examined artificial light harvesting system using inorganic nanosheet as host materials.[35-39] By using our original methodology that can suppress aggregation behavior of organic dyes on the inorganic surface, we have reported efficient supramolecular light harvesting systems. In this chapter, we have examined the conjugation of such light harvesting type energy transfer and subsequent electron transfer reaction in supramolecular system composed of inorganic nanosheet with chemical reaction flow control. To realize such system, three components are necessary at least, that is energy donor (EnD) and energy acceptor (EnA) and electron acceptor (eA) as shown in Figure 1. If three components are mixed, a reaction flow control should be necessary to suppress the unfavorable side reactions such as electron transfer from EnD to EnA and/or eA.

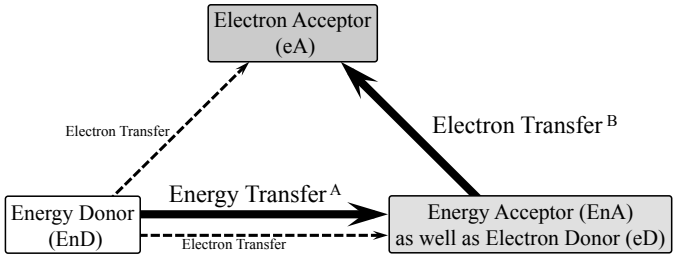

Figure 1. Reaction flow in three components system.

In this chapter, we tried to combine capsulation technique and molecular arrangement technique on the inorganic surface. Since electron transfer requires a

molecular collision or a close approach between molecules, a capsulation of EnD should suppress its electron transfer reactions. On the other hand, energy transfer reaction is still possible for such capsulated system, in the case of Förster type energy transfer.[17,28]

Takagi's group developed a molecular arrangement technique as follows. We have used clay minerals, which is one of the typical inorganic nano-sheet materials, as a novel host material to construct assembly of guest functional dyes. Saponite whose structure was shown in Figure 1-(a) is a group of clay materials characterized by (1) nanostructured flat sheets (thickness is 0.97 nm), (2) negatively charged surfaces, (3) optical transparency in the visible region in the exfoliated state, when the particle size is small (ca. <200 nm). We reported that multivalent cationic dyes adsorb on the clay surfaces without aggregation, and formation of these novel un-aggregated dye assemblies on the clay surfaces is attributed to size matching of the distance between cationic site of the dyes and anionic site on the clay surfaces. We called this unique technique as Size matching effect or inter-charge distance matching effect. Furthermore, we demonstrated energy transfer reaction between two kinds of co-adsorbed dyes on the clay surfaces to construct artificial light harvesting system.

Ramamurthy's group has demonstrated the value of an organic cavitand with eight ammonium groups (Octa-Amine which shown in Figure 2-(b), abbreviated as OAm_2^{16+} represents protonated capsular assembly having 16 positive charges) in controlling the excited-state behavior of molecules and also has shown that a guest-encapsulated OAm_2^{16+} capsule could adsorb on inorganic layered materials' surfaces, such as clay and α-Zr(IV) phosphate.[40-43] Recently, they reported efficiently energy transfer reaction

between cationic porphyrin (used as EnA) and capsulated neutral dyes (used as EnD) in OAm_2^{16+}. In this report, we tried connecting this energy transfer reaction to subsequent electron transfer reaction for constructing the reaction flow controlled three components system as shown in Figure 1 (bold line). The capsulation of EnD by cavitand OAm_2^{16+} would suppress the electron transfer reaction between capsulated EnD and enclosed cationic guest molecules (EnD and/or eA) by suppressing the collision or close approach between EnD and other molecules. 2-acetylanthracene (abbreviated as AA, shown in Figure 2-(c)), tetrakis(1-methylpyridinium-4-yl)porphyrinatozinc(abbreviated as $ZnTMPyP^{4+}$, shown in Figure 2-(d)) and 1,1'-bis (2,4-dinitrophenyl) -4,4'-bipyridinium dichloride (Abbreviated as $DNPV^{2+}$, shown in Figure 2-(e)) were used as EnD, EnA (as well as eD) and eA, respectively. Among these, AA was capsulated in OAm_2^{16+} in the present system. These guest molecules were assembled on the clay surface without aggregation, and energy transfer reaction and subsequent electron transfer reaction was demonstrated in this dyes-clay assembly system. We believe this novel three components system assembled on the clay surface will open the new window toward a realization of bio-mimicking artificial photosynthetic system.

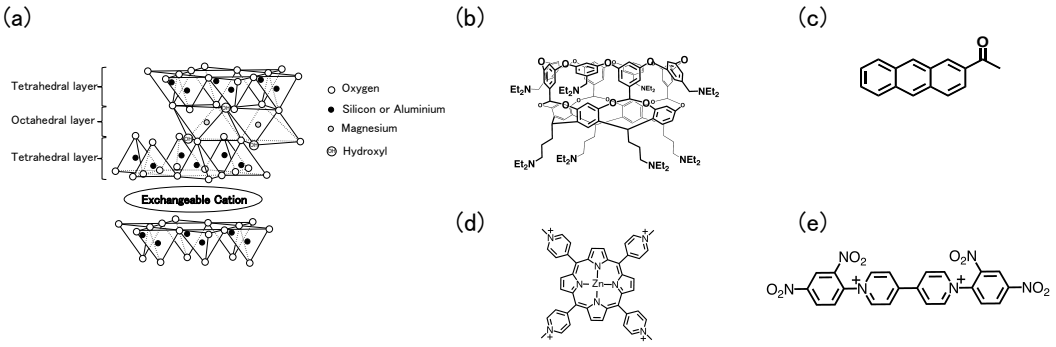

Figure 2. Structure of (a) Saponite, (b) Octa-Amine (OAm), (c) 2-acetylanthracene (AA), (d) tetrakis(1-methylpyridinium-4-yl)porphyrinatozinc ($ZnTMPyP^{4+}$), (e) 1,1'-bis(2,4-dinitrophenyl)-4,4'-bipyridinium dichloride ($DNPV^{2+}$).

7.2. Experimental section

Materials

The synthetic saponite clay mineral used in this experiment was purchased from Kunimine Industries. The organic cavitand with amine functionality Octa-Amine (OAm) was synthesized according to the reported procedure.[40] The guest molecules AA, $ZnTMPyP^{4+}$, and $DNPV^{2+}$ were purchased from Aldrich, Frontier scientific and Tokyo Chemical Industry, respectively. The purities of them were checked by ^{1}H-NMR and used as received. Water was deionized with an ORGANO BB-5A system (PF filter × 2 + G-10 column).

Analysis

Absorption spectra were measured with a Shimadzu UV-3150 spectrophotometer.

Fluorescence spectra were measured with an Edinburgh FS920CDT fluorometer equipped with a xenon lamp. For absorption and fluorescence measurements, a quartz cell was used. TG/DTA measurements were carried out with a Shimadzu DTG-60H analyzer to determine the water content of materials. The time-resolved fluorescence measurement was conducted under photoncounting conditions (Hamamatsu Photonics, C4334 streak scope, connected with CHROMEX 250IS polychrometer) with an EKSPLA PG-432 optical parametric generator (430 nm, 25 ps fwhm, 20 μJ, 1 kHz) pumped by the third harmonic radiation of Nd^{3+} :YAG laser, EKSPLA PL2210JE (355 nm, 25 ps fwhm, 300 **μ** J, 1 kHz). The laser flux was reduced with neutral density filters to avoid multiphoton absorption processes and nonlinear effects. The time-resolved fluorescence spectra were not corrected; thus, the obtained spectral shape was not the same as that of the steady state fluorescence spectroscopy even under the same condition.

Sample preparation

Solution of OAm_2^{16+} and AA included in OAm_2^{16+} under acidic condition (pH = 1.0) were obtained by following the previously reported procedure. [40,42] Inclusion of AA within OAm_2^{16+} and the ratio of the host to guest complex were checked by ^{1}H-NMR measurements and NMR titration experiments in water under acidic conditions (pH = 1.0). This capsulated AA in OAm_2^{16+} is abbreviated as AA@OAm_2^{16+}. Obtained stock solution of AA@OAm_2^{16+} was diluted by HCl aqueous solution, and the pH of that diluted stock solution was kept at 1.0. Guest molecules∩clay complex were obtained by

following procedure. (The symbol of ∩ represents the adsorption of guests on the clay nano-sheets.) HCl aqueous solution and stock solutions of each guest molecules were added into cuvette. Concentration of HCl aqueous solution was changed to keep the pH of obtained complex dispersion at 1.0. Then clay dispersion was added under stirring. All of the guest molecules were anchored on clay surfaces with electrostatic interaction between positively charges in the guest molecules and negatively charges on the clay surfaces.

According to our previous results, $AA@OAm_2^{16+}$ was adsorbed on the clay surface without aggregation up to 400% versus cation exchange capacity (CEC) of the clay.[42] It indicated that $AA@OAm_2^{16+}$ was adsorbed on the clay surfaces by 4 of 16 cationic sites of them. Actually, $AA@OAm_2^{16+}$ with 16 positive charges acts like a tetra-cationic porphyrin, indicating the only 4 cationic charges on the bottom of the $AA@OAm_2^{16+}$ anchors to the clay surface. In this paper, [the number of $AA@OAm_2^{16+}$] × 4 was used to express the loading levels on the clay surface (% vs CEC of the clay) in the case of $AA@OAm_2^{16+}$. On the other hand, $ZnTMPyP^{4+}$ and $DNPV^{2+}$ adsorbed on the clay surfaces by all of their cationic sites.[44,45] Thus ［the number of the $ZnTMPyP^{4+}$］× 4 and ［the number of $DNPV^{2+}$］× 2 was used to express the loading levels on the clay surface, respectively. The loading levels of $AA@OAm_2^{16+}$ and $ZnTMPyP^{4+}$ were set at 10% versus CEC of the clay, thus ratio of $AA@OAm_2^{16+}$ and $ZnTMPyP^{4+}$ corresponds to 1 to 1. The loading level of $DNPV^{2+}$ was changed to 5-80% versus CEC of the clay.

Calculation procedure for the energy transfer efficiency and the quenching efficiency

We reported that the energy transfer efficiency (η_{ET}) and the quenching efficiency (φ_q) can be quantitatively estimated by the analysis of the steady-state fluorescence spectra. The total fluorescence of (AA@OAm_2^{16}+&$ZnTMPyP^{4+}$)∩clay complex ($F_{ET}(\nu)$) can be expressed by equation 1.[36]

$$F_{ET}(\nu) = \left(1 - \eta_{ET} - \phi_q\right) \times F_D^{390}(\nu) + \left(1 + \frac{1 - 10^{-A_D}}{1 - 10^{-A_A}} \eta_{ET}\right) \times F_A^{390}(\nu) \quad \text{(eq. 1)}$$

where $F_{ET}(\nu)$ is the fluorescence spectrum of (AA@OAm_2^{16}+&$ZnTMPyP^{4+}$)∩clay complex, $F_D^{390}(\nu)$ and $F_A^{390}(\nu)$ are fluorescence spectra of AA@OAm_2^{16+}∩clay complex and $ZnTMPyP^{4+}$∩clay complex, respectively, η_{ET} is energy transfer efficiency defined in equation 2, φ_q is the quenching efficiency defined in equation 3, A_D and A_A is are the absorbance of AA@OAm_2^{16}∩clay complex and $ZnTMPyP^{4+}$∩clay complex at 390 nm, respectively.

$$\eta_{ET} = \frac{k_{ET}}{k_{ET} + k_d^D + k_f^D + k_q} \text{ (eq. 2)}$$

$$\eta_{ET} = \frac{k_q}{k_{ET} + k_d^D + k_f^D + k_q} \quad \text{(eq. 3)}$$

where k_d^D is the sum of non-radiative deactivation rate constant and intersystem crossing rate constant of AA@OAm_2^{16+}, k_f^D is the radiative deactivation rate constant of AA@OAm_2^{16+}, k_q is the quenching rate constant, and k_{ET} is energy transfer rate constant, respectively. On the basis of equation 1, the fluorescence spectrum, $F_{ET}(\nu)$ was

simulated with the use of the respective reference fluorescence spectra, $F_D^{390}(\nu)$ and $F_A^{390}(\nu)$. Thus, parameters η_{ET} and φ_q can be obtained from the spectral simulation. However, when $ZnTMPyP^{4+}$ was selectively excited by 610 nm wavelength light in ($ZnTMPyP^{4+}$&AA@OAm_2^{16+})∩clay system, fluorescence intensity for $ZnTMPyP^{4+}$ was increased compared to $ZnTMPyP^{4+}$∩clay due to suppression of self quenching reaction as shown in Figure 5. Considering this result, $F_D^{390}(\nu)$, which is reference fluorescence spetrum of $ZnTMPyP^{4+}$ ∩clay obtained by irradiation of the 390 nm wavelength light, also enhanced in presence of AA@OAm_2^{16+}. Compensating rate (n) for this fluorescence increase could be estimated from fluorescence intensity of $ZnTMPyP^{4+}$ on the clay surface by irradiation of the 610 nm wavelength light in absence and presence of AA@OAm_2^{16+}.

$$n = \frac{I^{610}}{I_0^{610}} \quad \text{(eq. 4)}$$

where $I^{610}{}_0$ and I^{610} is fluorescence intensity of $ZnTMPyP^{4+}$ on the clay surface by irradiation of the 610 nm wavelength light in absence and presence of AA@OAm_2^{16+}. Equation 5 was used to determine energy transfer and energy loss efficiency to compensate the fluorescence enhancement of $ZnTMPyP^{4+}$.

$$F_{ET}(\nu) = \left(1 - \eta_{ET} - \phi_q\right) \times F_D^{390}(\nu) + \left(1 + \frac{1 - 10^{-A_D}}{1 - 10^{-A_A}} \eta_{ET}\right) \times n F_A^{390}(\nu) \quad \text{(eq. 5)}$$

Calculation of Gibbs free energy change(ΔG_{el}) for the two electron transfer reaction

Changes of Gibbs free energy (ΔG_{el}) for the two electron transfer reaction (between capsulated AA in OAm_2^{16+} and $DNPV^{2+}$, between $ZnTMPyP^{4+}$ and $DNPV^{2+}$) could be calculated with following equation proposed by Rehm and Weller (eq. 6).[22,23]

$$\Delta G_{el}\ (kcal\ mol^{-1}) = 23.06\left[E^0(D^+/D) - E^0(A/A^-)\right] - w_p - \Delta G_{00}\ \text{(eq. 6)}$$

where $E^0(D^+/D)$ is oxidation potential of electron donor, $E^0(A/A^-)$ is reduction potential of $DNPV^{2+}$(+0.02 V vs. SHE,), and ΔG_{00} is excitation energy, respectively. The oxidation potentials of AA and ZnTMPyP are reported as +1.66 V (vs. SHE in MeCN) and +1.18 V (vs. SHE, in water), respectively. The each ΔG_{00} of $AA@OAm_2^{16+}$ and $ZnTMPyP^{4+}$ are calculated as 2.94 eV and 1.91 eV from fluorescence and absorption spectra, respectively. The ΔG_{el} for both of electron transfer reaction between AA and $DNPV^{2+}$, and between $ZnTMPyP^{4+}$ and $DNPV^{2+}$ were calculated as -127.9 and -84.1 kJ mol^{-1}, respectively. Although redox potentials of the molecules adsorbed on clay or included in cavitand would different from them in solution, these ΔG_{el} are sufficiently exergonic for occurrence for electron transfer reaction.

Calculation procedure for the energy transfer, electron transfer and energy loss efficiency in three components system.

Electron transfer efficiency between $ZnTMPyP^{4+}$ and $DNPV^{4+}$ could be determined by following equation 9.

$$\phi_{eT} = 1 - m \quad \text{(eq. 7)}$$

$$m = \frac{I^{610'}}{I^{610}} \text{ (eq. 8)}$$

where I^{610} and $I^{610'}$ is fluorescence intensity of $(AA@OAm_2^{16+}\&ZnTMPyP^{4+})\cap clay$ and $(AA@OAm_2^{16+}\&ZnTMPyP^{4+}\&DNPV^{2+})\cap clay$ by irradiation of the 610 nm wavelength light, respectively. Likewise, the reference fluorescence spectrum for $ZnTMPyP^{4+}$ ($F(\nu)_A^{390}$) must be also quenched in presence of $DNPV^{2+}$, thus energy transfer and energy loss efficiency could be calculated by equation 11.

$$F_{ET}(\nu) = \left(1 - \eta_{ET} - \phi_q\right) \times F_D^{390}(\nu) + \left(1 + \frac{1 - 10^{-A_D}}{1 - 10^{-A_A}} \eta_{ET}\right) \times nmF_A^{390}(\nu) \quad \text{(eq. 9)}$$

7.3. Results and discussion

Absorption spectra of $AA@OAm_2^{16+}\cap clay$, $ZnTMPyP^{4+}\cap clay$, $DNPV^{2+}\cap clay$

Absorption spectra of $AA@OAm_2^{16+}\cap clay$, $ZnTMPyP^{4+}\cap clay$, $DNPV^{2+}\cap clay$ were shown in Figure 3.

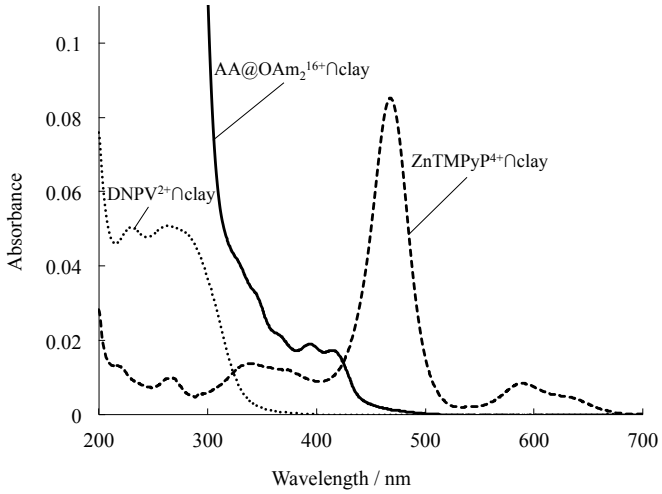

Figure 3. Absorption spectra of $AA@OAm_2^{16+}$∩clay (solid line), $ZnTMPyP^{4+}$∩clay (broken line), $DNPV^{2+}$∩clay (dotted line).

Concentration of the $AA@OAm_2^{16+}$, $ZnTMPyP^{4+}$, $DNPV^{2+}$ and clay were set at 1.0×10^{-5} M (corresponding to 50% versus CEC of the clay), 1.0×10^{-6} M (corresponding to 5% versus CEC of the clay), 1.7×10^{-5} M (corresponding to 40% versus CEC of the clay) and 8.4×10^{-2} g L^{-1}, respectively.

We reported that $AA@OAm_2^{16+}$, $ZnTMPyP^{4+}$ and $DNPV^{2+}$ molecules adsorbed on the clay surface up to 100, 100, 80% versus CEC without aggregation, respectively. It is important to note that both of $ZnTMPyP^{4+}$ and $AA@OAm_2^{16+}$ can be excited by wavelength of the light within the range of 390 to 420 nm, and adsorbed $ZnTMPyP^{4+}$ on the clay surface is selectively excited by wavelength range of over 460 nm. Thus, energy transfer reaction could be demonstrated by excitation light within the range of 390 to 420nm, and fluorescence quenching behavior of $ZnTMPyP^{4+}$, which was not affected by energy transfer reaction, could be estimated by the fluorescence spectra

obtained by excitation light wavelength of 460 nm or more. This switching of stimulus and selective excitation is utilized to estimate the energy transfer and electron transfer efficiencies in three components system as described later. $DNPV^{2+}$∩clay did not have absorption band in a wavelength over 380 nm as shown in Figure 3, thus $DNPV^{2+}$ did not avoid the light absorption of $AA@OAm_2^{16+}$ and $ZnTMPyP^{4+}$ in this wavelength range, and photochemical reaction, such as electron transfer, of excited $DNPV^{2+}$ can be excluded.

Energy transfer reactionin in ($AA@OAm_2^{16+}$(EnD)−$ZnTMPyP^{4+}$ (EnA))∩clay system

The energy transfer reaction between $AA@OAm_2^{16+}$ and $ZnTMPyP^{4+}$, that is A part in Figure 1, was demonstrated.We previously reported the energy transfer reaction between $AA@OAm_2^{16+}$ and $ZnMPyP^{4+}$ at high dye loadings (loading level of the $AA@OAm_2^{16+}$ and $ZnTMPyP^{4+}$ were set at 50% versus CEC of the clay, respectively) However, to construct the assembled structure composed of three kinds of guest molecules on the clay surfaces, vacant anionic sites on which $DNPV^{2+}$ will adsorb is necessary. Thus the loading levels of $AA@OAm_2^{16+}$ and $ZnTMPyP^{4+}$ were set at 10% versus (CEC) of the clay, respectively. Fluorescence spectra of $AA@OAm_2^{16+}$∩clay, $ZnTMPyP^{4+}$∩clay and co-adsorbed sample for energy transfer {($AA@OAm_2^{16+}$−$ZnTMPyP^{4+}$)∩clay} were shown in Figure 4. Excitation wavelength was set at 390 nm to measure these spectra.

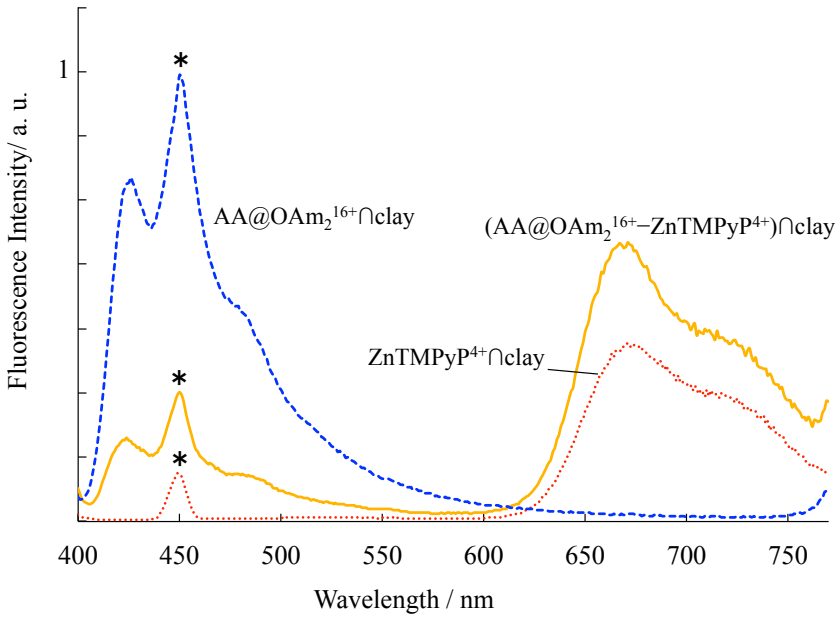

Figure 4. Fluorescence spectra of $AA@OAm_2^{16+}$∩clay(blue broken line), $ZnTMPyP^{4+}$∩clay (red dotted line) and $(AA@OAm_2^{16+}–ZnTMPyP^{4+})$∩clay (solid yellow line). The symbol (＊) is Raman scatter light.

Concentration of the $AA@OAm_2^{16+}$, $ZnTMPyP^{4+}$, and clay were set at 2.5×10^{-7} M (corresponding to 10% versus CEC of the clay), 2.5×10^{-7} M (corresponding to 10% versus CEC of the clay) and 1.0×10^{-2} g L^{-1}, respectively.

In the energy transfer sample $\{(AA@OAm_2^{16+}–ZnTMPyP^{4+})$∩clay$\}$,the fluorescence intensity of the EnD ($AA@OAm_2^{16+}$) decreased and intensity of the EnA ($ZnTMPyP^{4+}$) increased compared to those of each monomer∩clay. It indicated an occurrence of energy transfer reaction between $AA@OAm_2^{16+}$ and $ZnTMPyP^{4+}$. Interestingly, when $ZnTMPyP^{4+}$ was selectively excited by an irradiation of 610 nm wavelength light, the fluorescence intensity of $(AA@OAm_2^{16+}–ZnTMPyP^{4+})$∩clay was also increased

compared to that of $ZnTMPyP^{4+}$∩clay as shown in Figure 5.

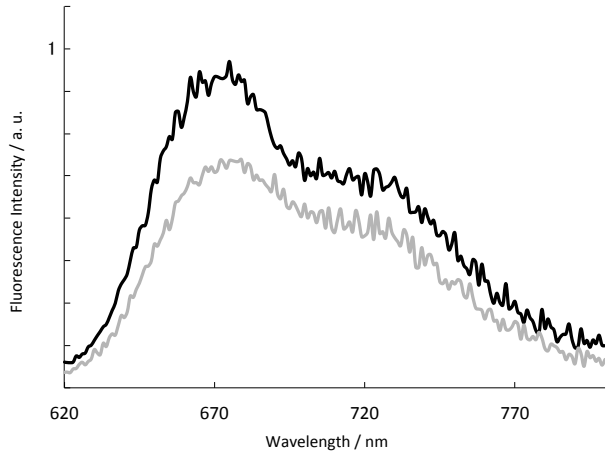

Figure 5. Fluorescence spectra of $ZnTMPyP^{4+}$∩clay (gray line) and ($AA@OAm_2^{16+}$&$ZnTMPyP^{4+}$)∩clay (black line). Excitation wavelength was set at 610 nm.

We reported that fluorescence intensity of $ZnTMPyP^{4+}$ was slightly quenched by self fluorescence quenching reaction on the clay surfaces. We considered this increase of fluorescence would be ascribed to suppression of this self quenching reaction. It is supposed that $ZnTMPyP^{4+}$ and $AA@OAm_2^{16+}$ uniformly adsorbed on the clay surface, then collision of $ZnTMPyP^{4+}$-to-$ZnTMPyP^{4+}$ may be suppressed by $AA@OAm_2^{16+}$ adsorbed between $ZnTMPyP^{4+}$ molecules. To confirm the occurrence of energy transfer reaction, time resolved fluorescence measurements of ($AA@OAm_2^{16+}$–$ZnTMPyP^{4+}$)∩clay were carried out. Excitation wavelengths were set at 468 nm and 410 nm light, respectively, and wavelength range of detection was set at 690-780 nm to detect the fluorescence for $ZnTMPyP^{4+}$. As described above,

$ZnTMPyP^{4+}$ and $AA@OAm_2^{16+}$ is simultaneously excited by 410 nm light, thus energy transfer reaction will occur by irradiation of 410 nm wavelength light. On the other hand, adsorbed $ZnTMPyP^{4+}$ on the clay surface can be selectively excited by 468 nm wavelength light, thus energy transfer reaction will not occur by irradiation of 468 nm wavelength light. The normalized fluorescence decays by the irradiation of 410 and 468 nm wavelength lights were shown in Figure 6. The decay curve obtained by 468 nm excitation light showed single exponential decay, and fluorescence lifetime was determined to be 0.79 ns. On the other hand, when excitation wavelength was set at 410 nm, an obvious rise component was observed. This rise component strongly indicated the occurrence of energy transfer reaction between $AA@OAm_2^{16+}$ and $ZnTMPyP^{4+}$ on the clay surfaces. This decay curve (excited by 410 nm light) can be analyzed as a double-exponential decay with rise (<0.10 ns) and decay (0.79 ns) components.

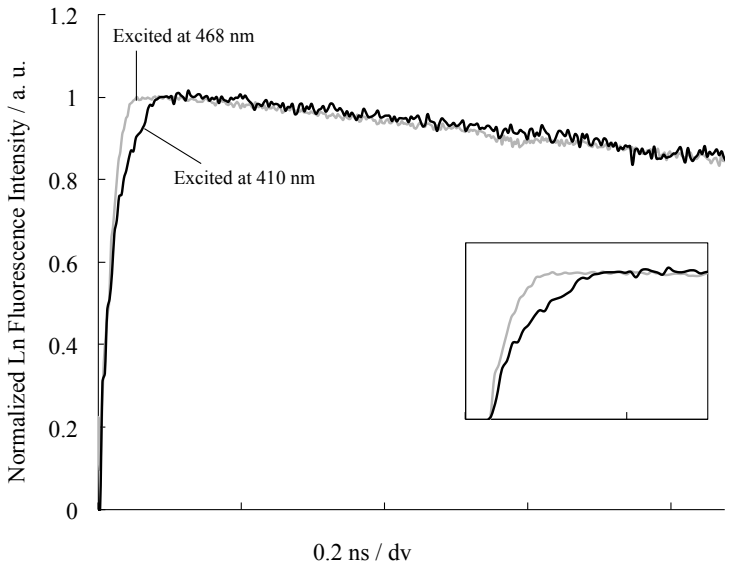

Figure 6. Normalized time resolved fluorescence decays of

($AA@OAm_2^{16+}$–$ZnTMPyP^{4+}$)∩clay by irradiation of the 410 nm wavelength light(black line) and 468 nm wavelength light(gray line).

Inset: the enlarged figure around the peak top in Figure 6.

Concentration of the $AA@OAm_2^{16+}$, $ZnTMPyP^{4+}$, and clay were set at 5.0×10^{-6} M (corresponding to 10% versus CEC of the clay), 5.0×10^{-6} M (corresponding to 10% versus CEC of the clay) and 0.2 g L^{-1}, respectively.

Energy transfer efficiency was determined by the analysis of the fluorescence spectra according to the method outlined in the Experimental section. The energy transfer efficiency (η_{ET}) and the quenching efficiency(φ_q), which were defined as equation 1 and 2, were determined to be 67% and 5%, respectively.

$$\eta_{ET} = \frac{k_{ET}}{k_{ET} + k_d^D + k_f^D + k_q} \quad \text{(eq. 1)}$$

$$\phi_q = \frac{k_q}{k_{ET} + k_d^D + k_f^D + k_q} \quad \text{(eq. 2)}$$

The energy transfer reaction proceeded in spite of low dye loadings. It indicated that these guests adsorbed on clay would make island structure as shown in Figure 7, considering the distance dependence of fluorescence resonance energy transfer reaction.

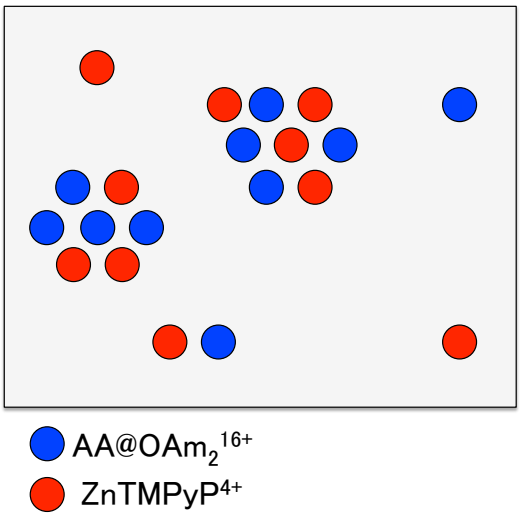

Figure 7. Models of the adsorption distribution of ($AA@OAm_2^{16+}$&$ZnTMPyP^{4+}$)∩clay

Electron transfer reaction between ($AA@OAm_2^{16+}$(EnD)−$DNPV^{2+}$(eA)) ∩clay system and ($ZnTMPyP^{4+}$(EnA as well as eD)−$DNPV^{2+}$)∩clay system

The objective electron transfer reaction between $ZnTMPyP^{4+}$ and $DNPV^{2+}$ (B part in Figure 1) and side electron transfer reaction between $AA@OAm_2^{16+}$ and $DNPV^{2+}$ was examined. Changes of Gibbs free energy (ΔG_{el}) for the two electron transfer reaction described above was calculated with an equation proposed by Rehm and Weller, and details of calculations were outlined in Experimental section. The calculated ΔG_{el} of both reaction are sufficiently exergonic, thus both electron transfer reaction will proceed.

The steady-state fluorescence was measured for $AA@OAm_2^{16+}$∩clay and $ZnTMPyP^{4+}$∩clay sample with and without $DNPV^{2+}$. The absorption amount of $DNPV^{2+}$ was set at 80% versus CEC of the clay. Fluorescence intensity of ($AA@OAm_2^{16+}$)∩clay was not affected by the addition of $DNPV^{2+}$ as can be seen in

Figure 8-(a). On the other hand, The fluorescence spectra of $ZnTMPyP^{4+}$∩clay was drastically decreased by the addition of $DNPV^{2+}$ as can be seen in Figure 8-(b). These results indicate that a capsulation of molecule suppresses its electron transfer reaction quite effectively. It is important to note that absorption spectra of $ZnTMPyP^{4+}$∩clay and ($ZnTMPyP^{4+}$−$DNPV^{2+}$)∩clay were almost same, and this indicates that $ZnTMPyP^{4+}$ did not interact with $DNPV^{2+}$ on the clay surfaces, such as aggregation.

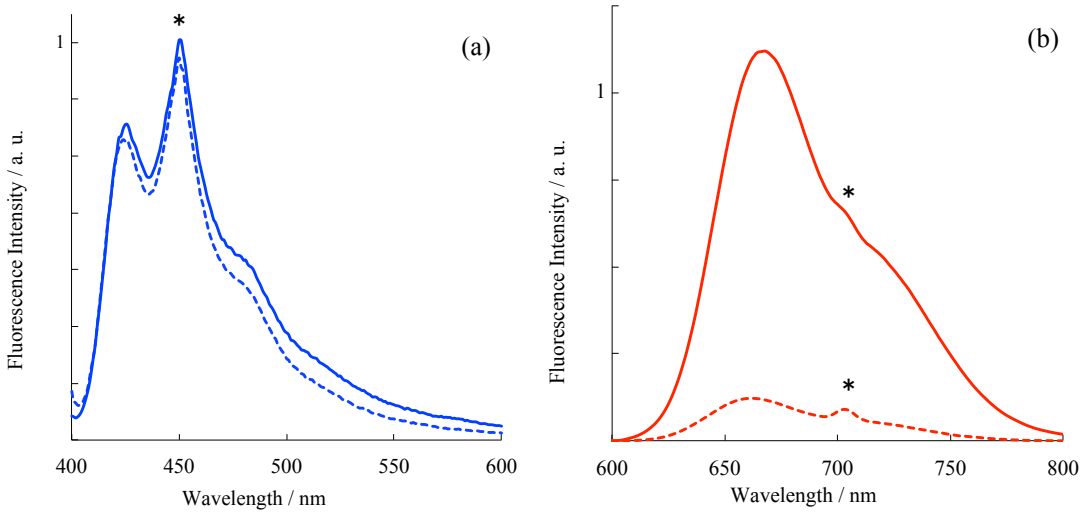

Figure 8. (a) Fluorescence spectra of $AA@OAm_2^{16+}$∩clay (broken line) and ($AA@OAm_2^{16+}$−$DNPV^{2+}$)∩clay (solid line), (b) Fluorescence spectra of ($ZnTMPyP^{4+}$−$DNPV^{2+}$)∩clay (broken line) and $ZnTMPyP^{4+}$∩clay(solid line). Concentration of the $AA@OAm_2^{16+}$, $ZnTMPyP^{4+}$, $DNPV^{2+}$ and clay were set at 2.5×10^{-7} M (corresponding to 10% versus CEC of the clay), 2.5×10^{-7} M (corresponding to 10% versus CEC of the clay), 4.0×10^{-6} M (cprresponding to the 80% versus CEC of the clay) and 1.0×10^{-2} g L^{-1}, respectively. The symbol (＊) is Raman scatter light.

Electron transfer rate constant could be estimated by Stern-Volmer equation. However, this plot showed upward curvature as shown in Figure 9.

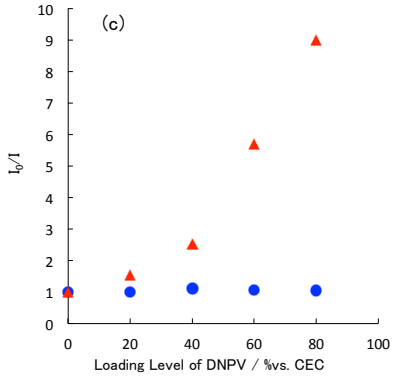

Figure 9. I_0/I plot of ($ZnTMPyP^{4+}$–$DNPV^{2+}$)∩clay (round) and ($AA@OAm_2^{16+}$–$DNPV^{2+}$)∩clay systems(triangle). Horizontal axis is the loading level of $DNPV^{2+}$. Concentration of $DNPV^{2+}$ was changed from 0 to 4.0×10^{-6} M (corresponding to 0 and 80% versus CEC of the clay, respectively)

Electron transfer rate constant could be estimated by following Stern-Volmer equation.[28]

$$\frac{I_0}{I} = 1 + K_{SV}[Q] \text{ (eq.10)}$$

where I_0 and I is fluorescence intensities in absence and presence of quencher, ［Q］ is concentration of the quencher, respectively. And Ksv is the Stern-Volmer constant from which one can estimate the rate constant of quenching reaction.

$$K_{SV} = \tau_0 k_{eT} \text{ (eq.11)}$$

where τ_0 is the life-time of the fluorophore and k_{eT} is electron transfer rate constant, respectively. The Stern-Volmer plots in both systems were shown in Figure 9. The slope of Stern-Volmer like plot for $(AA@OAm_2^{16+}-DNPV^{2+})\cap$clay system is almost zero. It indicated the electron transfer rate constant is very low. On the other hand, the value of I_0/I in $(ZnTMPyP^{4+}-DNPV^{2+})\cap$clay system was increased with increase of $DNPV^{2+}$ concentration. However, this plot showed upward curvature, thus k_{eT} could not be estimated from the slope of this Stern-Volmer plot. We believe reason of this upward curvature is un-uniform absorption distribution of $ZnTMPyP^{4+}$ and $DNPV^{2+}$. Thus k_{eT} could not be estimated from the slope of this Stern-Volmer plot. To confirm that fluorescence quenching is dynamic process and to estimate the electron transfer rate constant between excited $ZnTMPyP^{4+}$ and $DNPV^{2+}$, time-resolved fluorescence measurements were carried out. The time-resolved fluorescence decays of $ZnTMPyP^{4}\cap$clay and $(ZnTMPyP^{4+}-DNPV^{2+})\cap$clay were shown in Figure 10.

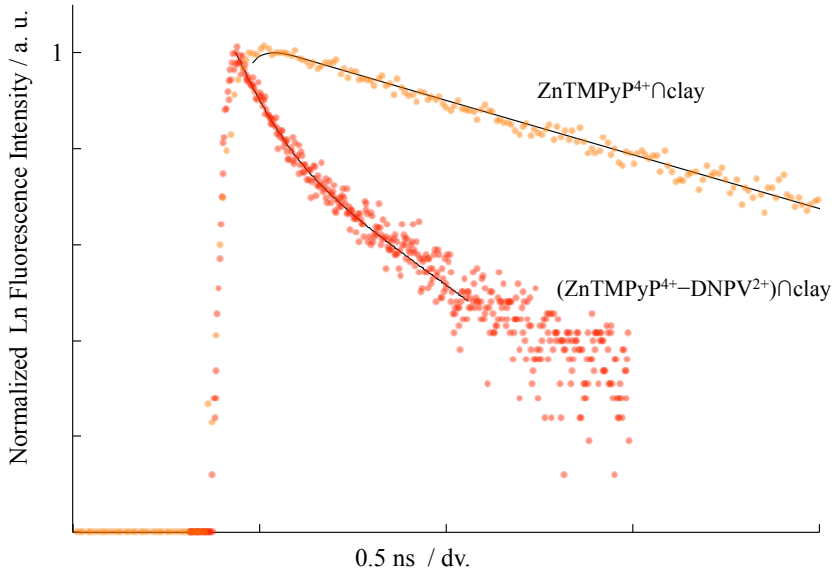

Figure 10. Time resolved fluorescence decay curves of $ZnTMPyP^{4+}$∩clay(orange dot) and ($ZnTMPyP^{4+}$–$DNPV^{2+}$)∩clay(red dot). The black solid lines were fitting curves for those decay profiles. Concentration of the $ZnTMPyP^{4+}$, $DNPV^{2+}$ and clay were set at 5.0×10^{-6} M (corresponding to 10% versus CEC of the clay), 8.0×10^{-5} M (corresponding to 80% versus CEC of the clay) and 0.2 g L^{-1}, respectively.

The electron transfer rate constant was calculated by following equation.

$$k_{eT} = \frac{1}{\tau_i} - \frac{1}{\tau_0} \qquad \text{(eq. 12)}$$

where τ_0 is lifetime of the $ZnTMPyP^{4+}$∩clay and τ_i is each lifetime of the ($ZnTMPyP^{4+}$–$DNPV^{2+}$)∩clay. The electron transfer rate constants were calculated as 8.6×10^{8} s^{-1} and 2.0×10^{9} s^{-1}, respectively. The absorption amount of $DNPV^{2+}$ was set at 80% versus CEC of the clay. The decay curve for $ZnTMPyP^{4+}$∩clay could be analyzed as a single exponential decay, and the lifetime was determined as 0.74 ns.

On the other hand, that of ($ZnTMPyP^{4+}$−$DNPV^{2+}$)∩clay could be analyzed by a double exponential analysis, and the lifetime were determined to be 0.08 ns (77%) and 0.33 ns (23%). This indicates that all $ZnTMPyP^{4+}$ was quenched by $DNPV^{2+}$ and there are two kinds of porphyrins in different situations on the clay surface. We considered that the adsorption distribution of $ZnTMPyP^{4+}$ and $DNPV^{2+}$ is not uniform as shown in Figure 11-(a).

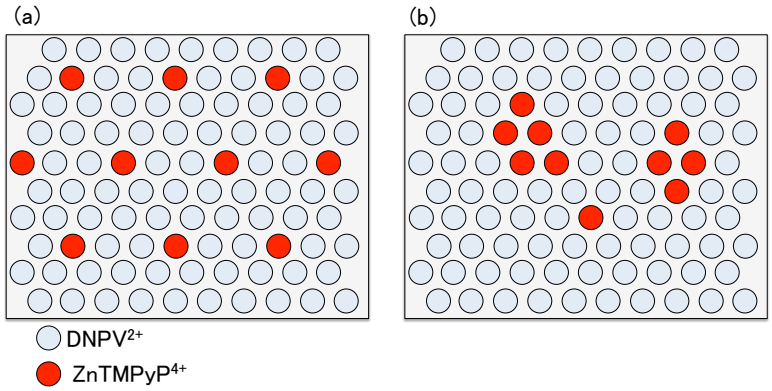

Figure 11. Models of the adsorption distribution of ($ZnTMPyP^{4+}$&$DNPV^{2+}$)∩clay
(a)uniform distribution (b)un-uniform distribution

Because if absorption distribution of $ZnTMPyP^{4+}$ and $DNPV^{2+}$ is uniform as shown in Figure 10-(b), the decay curve of ($ZnTMPyP^{4+}$−$DNPV^{2+}$)∩clay would be able to be analyzed as single exponential.

Energy Transfer Reaction and Subsequent Electron Transfer Reaction in {AA@OAm_2^{16+}(EnD)−$ZnTMPyP^{4+}$(EnA as well as eD)−$DNPV^{2+}$(eA))∩Clay System

The fluorescence spectra of AA@OAm_2^{16+}∩clay, (AA@OAm_2^{16+}−$ZnTMPyP^{4+}$)∩clay(energy transfer system) and (AA@OAm_2^{16+}−$ZnTMPyP^{4+}$−$DNPV^{2+}$)∩clay (energy and subsequent electron transfer system) at each $DNPV^{2+}$ loadings were shown in Figure 12. Excitation wavelength was set at 390 nm to obtain these fluorescence spectra. Fluorescence intensity of AA@OAm_2^{16+} was still quenched in (AA@OAm_2^{16+}−$ZnTMPyP^{4+}$−$DNPV^{2+}$)∩clay compared to AA@OAm_2^{16+}∩clay at every loading levels of $DNPV^{2+}$. It indicated an occurrence of energy transfer reaction between AA@OAm_2^{16+} and $ZnTMPyP^{4+}$ in spite of the presence of $DNPV^{2+}$, because fluorescence of AA@OAm_2^{16+} was not quenched by $DNPV^{2+}$. Fluorescence intensity of $ZnTMPyP^{4+}$ decreased with increase of $DNPV^{2+}$ loadings. It indicated an occurrence of electron transfer reaction between $ZnTMPyP^{4+}$ and $DNPV^{2+}$, thus these results indicated the occurrence of energy transfer reaction and subsequent electron transfer reaction in (AA@OAm_2^{16+}−$ZnTMPyP^{4+}$−$DNPV^{2+}$)∩clay system.

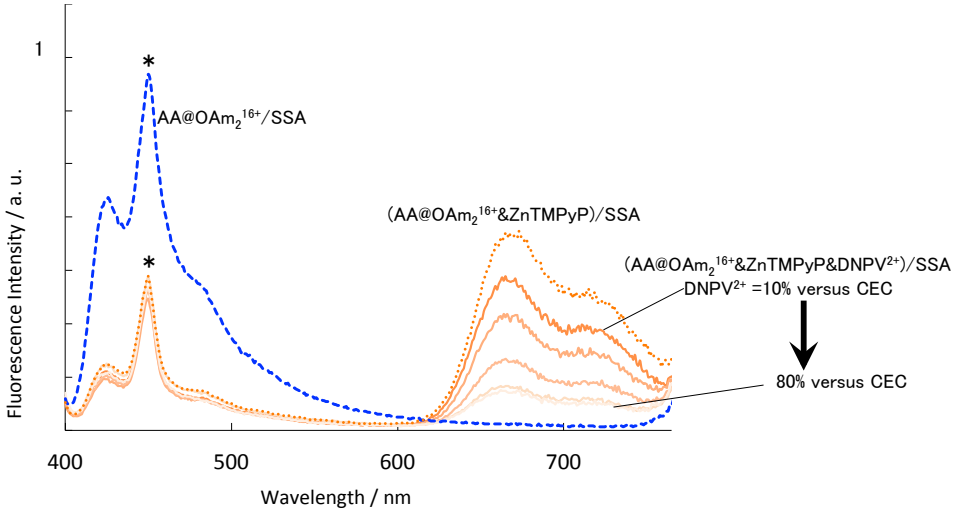

Figure 12. Steady-state fluorescence spectra of $AA@OAm_2^{16+}$∩clay(broken line), $(AA@OAm_2^{16+}–ZnTMPyP^{4+})$∩clay(dotted line) and $(AA@OAm_2^{16+}–ZnTMPyP^{4+}–DNPV^{2+})$∩clay at each loading levels of $DNPV^{2+}$(solid lines)

Excitation wavelength was set at 390 nm.

Concentration of the $AA@OAm_2^{16+}$, $ZnTMPyP^{4+}$ and clay were set at 2.5×10^{-7} M (corresponding to 10% versus CEC of the clay), 2.5×10^{-7} M (corresponding to 10% versus CEC of the clay), and 1.0×10^{-2} g L^{-1}, respectively.

Concentration of $DNPV^{2+}$ was changed from 0 to 4.0×10^{-6} M (corresponding to 0 and 80% versus CEC of the clay, respectively)

The symbol (＊) is Raman scatter light

Time resolved fluorescence decay of $(AA@OAm_2^{16+}–ZnTMPyP^{4+}–DNPV^{2+})$∩clay were carried out to elucidate occurrence of the energy transfer and subsequent electron

transfer reaction. Normalized time resolved fluorescence decays by the irradiation of the excitation light of 468 nm and 410 nm wavelength were shown in Figure 13. The fluorescence decay, where $ZnTMPyP^{4+}$ was selectively excited, could be analyzed as double exponential curve in a similar way to the electron transfer system $\{(ZnTMPyP^{4+}-DNPV^{2+})\cap$ clay$\}$ system, and the life-time were determined as 0.04 ns (79%) and 0.30 ns (21%). These values were almost same as the lifetime for $ZnTMPyP^{4+}$ in $(ZnTMPyP^{4+}\cap DNPV^{2+})\cap$clay system. On the other hand, when excitation wavelength was set at 410 nm, obvious delay was observed. This delay indicates the presence of rise component, and this rise component strongly indicated the occurrence of energy transfer reaction. Then, the decay component is clearly fast compared to the decay in the absence of $DNPV^{2+}$. This fast decay indicated the occurrence of subsequent electron transfer next to the energy transfer reaction. This fluorescence decay could not be analyzed as double exponential, but could be analyzed tri-exponential curve composed from one rise component (<0.10 ns) and two decay components (0.05 ns and 0.33 ns).

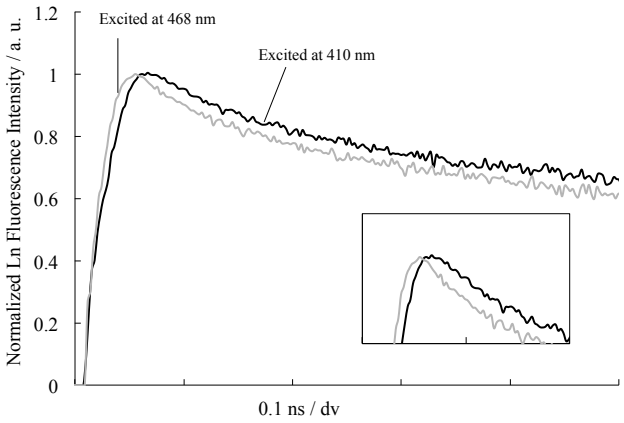

Figure 13. Normalized time resolved fluorescence decay of $(AA@OAm_2^{16+}–ZnTMPyP^{4+}–DNPV^{2+})\cap$clay by irradiation of the 468 nm wavelength laser pulse(gray line) and by irradiation of the 410 nm wavelength laser pulse(black line).

Inset: the enlarged figure around the peak top in Figure 13.

Concentration of the $AA@OAm_2^{16+}$, $ZnTMPyP^{4+}$, $DNPV^{2+}$ and clay were set at 5.0×10^{-6} M (corresponding to 10% versus CEC of the clay), 5.0×10^{-6} M (corresponding to 10% versus CEC of the clay), 8.0×10^{-5} M (corresponding to 80% versus CEC of the clay) and 0.2 g L^{-1}, respectively.

The efficiencies of energy transfer reaction, energy loss and electron transfer at each $DNPV^{2+}$ loadings could be determined by the analysis of the fluorescence spectra according to the method outlined in the Experimental section. These efficiencies were summarized in Table 1.

Table 1. Efficiencies of energy transfer, electron transfer and energy loss

Loading level of $DNPV^{2+}$ / % versus CEC of the clay	0	5	10	20	30	40	50	60	70	80
Energy transfer efficiency	0.67	0.68	0.72	0.72	0.73	0.72	0.73	0.73	0.72	0.70
Electron transfer efficiency	0	0.1	0.25	0.43	0.58	0.66	0.7	0.79	0.8	0.81
Energy loss efficiency	0.05	0.05	0.04	0.07	0.03	0.07	0.04	0.01	0.04	0.08

The energy transfer efficiency between $AA@OAm_2^{16+}$ and $ZnTMPyP^{4+}$ was little changed despite of the presence of $DNPV^{2+}$, and average energy transfer efficiency is 71%. The electron transfer efficiency between $ZnTMPyP^{4+}$ and $DNPV^{2+}$ were increased with increase of the amount of $DNPV^{2+}$, the maximum electron transfer efficiency was 81% when loading level of $DNPV^{2+}$ is 80% versus CEC of the clay. Furthermore, average of energy loss, such as electron transfer reaction between $AA@OAm^{2+}$ and $DNPV^{2+}$, was smaller than 5%. These results indicates that selective energy transfer reaction and subsequent electron transfer reaction proceeded in $(AA@OAm_2^{16+}–ZnTMPyP^{4+}–DNPV^{2+})\cap$clay system. Finally, we discussed the adsorption distribution of $AA@OAm_2^{16+}$, $ZnTMPyP^{4+}$ and $DNPV^{2+}$ on the clay surface. The conceivable adsorption structures of them were shown in Figure 14. Energy transfer reaction depends on inter molecular distance, thus efficiently energy transfer reaction should not occurred in the cases of structure (a) or (b). In the case of (c), energy transfer will proceed, but efficiency of the energy transfer will be very low. Thus structure (a),

(b) and (c) will be denied, and the conceivable adsorption structure is Figure-(d), or (e). However, if the big island were formed as shown in structure-(d), the quenching of the ZnTMPyP will be not efficient because $ZnTMPyP^{4+}$ surrounded by $AA@OAm_2^{16+}$ or $ZnTMPyP^{4+}$ would not be quenched sufficiently. We concluded that $AA@OAm_2^{16+}$ and $ZnTMPyP^{4+}$ were formed small islands, and those are surrounded by $DNPV^{2+}$ such as structure-(e).

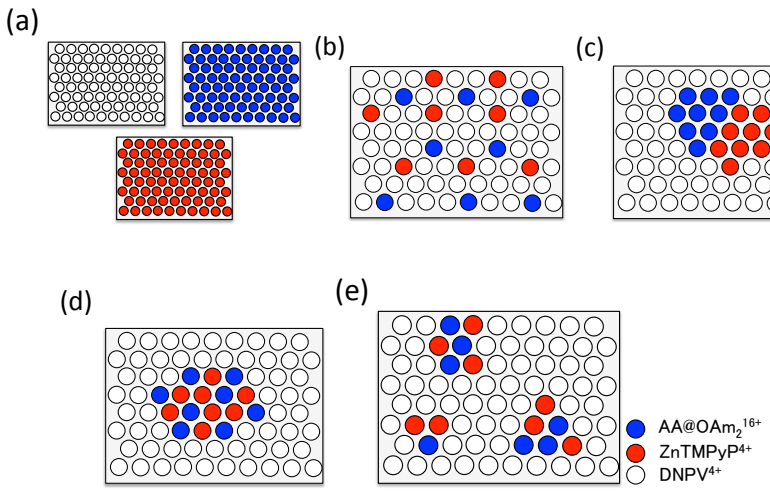

Figure 14. Conceivable adsorption structures of $(AA@Oam_2^{16+}–ZnTMPyP^{4+}–DNPV^{2+})\cap$clay (a) Inter-sheet segregation, (b)Uniform, (c)Segregation, (d) Formation of the large island composed of $AA@Oam_2^{16+}$ and $ZnTMPyP^{4+}$, (e) Formation of small islands composed of $AA@Oam_2^{16+}$ and $ZnTMPyP^{4+}$.

7.4. Conclusion

We proposed novel strategy to demonstrated the energy transfer reaction and subsequent electron transfer reaction between three kind of the dyes assembled on the clay surfaces. The energy donor was capsulated in cationic cavitand to control the photochemical reaction flow by suppressing the side electron transfer between EnD and eA. The average energy transfer efficiency in this sequential reaction system is 71%, and maximum efficiency of subsequent electron transfer reaction is 81%. Furthermore, side electron transfer reaction between energy donor and electron acceptor was suppressed, and average of energy loss was under 5%. We believe that this novel three components system assembled on the clay surface will allow us to make progress toward realization of biomimicking system for an artificial photosynthetic system.

7.5. Reference

1. Voet, D.; Voet, J. G. Biochemistry, Wiley, New York, 1995.

2. Barber, J.; Andersson, B. Revealing the blueprint of photosynthesis. *Nature* **1994,** *370* , 31-34.

3. Inoue, H.; Funyu, S.; Shimada, Y.; Takagi, S. Artificial photosynthesis via two-electron conversion: Photochemical oxygenation sensitized by ruthenium porphyrins with water as both electron and oxygen atom donor. *Pure Appl. Chem.* **2005,** *77*, 1019–1033 .

4. Hu, X.; Schulten, K. How Nature Harvests Sunlight. *Phys. Today* **1997,** *50*, 28.

5. McDermott, G.; Prince, S. M.; Freer, A. A.; Hawthornthwaite-Lawless, A. M.; Papiz, M. Z.; Cogdell, R. J.; Isaacs, N. W. Crystal structure of an integral membrane light-harvesting complex from

photosynthetic bacteria. *Nature* **1995,** *374*, 517-521.

6. Hu, X.; Ritz, T.; Damjanović, A.; Schulten, K. Pigment Organization and Transfer of Electronic Excitation in the Photosynthetic Unit of Purple Bacteria. *J. Phys. Chem. B* **1997,** *101*, 3854-3871.

7. Glazer, A. N. Comparative biochemistry of photosynthetic light-harvesting systems. *Annu. Rev. Biochem.* **1983,** *52*, 125-157.

8. Stowell, M. H. Light-Induced Structural Changes in Photosynthetic Reaction Center: Implications for Mechanism of Electron-Proton Transfer. *Science* **1997,** *276*, 812-816.

9. Kuglstatter, A.; Ermler, U.; Michel, H.; Baciou, L.; Fritzsch, G. X-ray Structure Analyses of Photosynthetic Reaction Center Variants fromRhodobacter sphaeroides: Structural Changes Induced by Point Mutations at Position L209 Modulate Electron and Proton Transfer†. *Biochem.* **2001,** *40*, 4253-4260.

10. Leslie Dutton, P.; Leigh, J. S.; Seibert, M. Primary processes in photosynthesis: In situ ESR studies on the light induced oxidized and triplet state of reaction center bacteriochlorophyll. *Biochem. Biophys. Res. Comm.* **1972,** *46*, 406-413.

11. Deisenhofer, J.; Epp, O.; Miki, K.; Huber, R.; Michel, H. Structure of the protein subunits in the photosynthetic reaction centre of Rhodopseudomonas viridis at 3Å resolution. *Nature* **1985,** *318*, 618-624.

12. Michel, H.; Deisenhofer, J. Relevance of the photosynthetic reaction center from purple bacteria to the structure of photosystem II. *Biochem.* **1988,** *27*, 1-7.

13. Kasha, M. Introductory Remarks to the Exciton Symposium: Radiation Research Society Meeting, Colorado Springs, May 22, 1962. *Rad. Res.* **1962,** *20*, 53-54.

14. Förster, T. 10th Spiers Memorial Lecture. Transfer mechanisms of electronic excitation. *Discuss. Faraday Soc.* **1959,** *27*, 7.

15. Förster, T. Zwischenmolekulare Energiewanderung und Fluoreszenz. *Annalen der Physik* **1948,** *437*, 55-75.

16. Dexter, D. L. A Theory of Sensitized Luminescence in Solids. *J. Chem. Phys.* **1953,** *21*, 836.

17. Turro, N. J. Modern Molecular Photochemistry; University Science Books, Mill Valley, CA 1991.

18. Barbara, P. F.; Meyer, T. J.; Ratner, M. A. Contemporary Issues in Electron Transfer Research. *J. Phys. Chem.* **1996,** *100*, 13148-13168.

19. Marcus, R. A.; Sutin, N. Electron transfers in chemistry and biology. *Biochimica et Biophysica Acta (BBA) – Rev. Bioenergetics* **1985,** *811*, 265-322.

20. Fleming, G. R.; Wolynes, P. G. Chemical Dynamics in Solution. *Phys. Today* **1990,** *43*, 36.

21. Albinsson, B.; Martensson, J. Long-range electron and excitation energy transfer in donor–bridge–acceptor systems. *J. Photochem. Photobiol. C: Photochem. Rev.* **2008,** *9*, 138-155.

22. Rehm, D. W., Albert. Kinetik und Mechanismus der Elektronübertragung bei der Fluoreszenzlöschung in Acetonitril (pages 834–839). *Berichte der Bunsengesellschaft für physikalische Chemie* **1969,** *73*, 834-839.

23. Rehm, D.; Weller, A. Kinetics of Fluorescence Quenching by Electron and H-Atom Transfer. *Isr. J. Chem.* **1970,** *8*, 259-271.

24. Libby, W. F. Theory of Electron Exchange Reactions in Aqueous Solution. *J. Phys. Chem.* **1952,** *56*, 863-868.

25. Barbara, P. F.; Walker, G. C.; Smith, T. P. Vibrational modes and the dynamic solvent effect in electron and proton transfer. *Science* **1992,** *256*, 975-981.

26. Marcus, R. A. Chemical and Electrochemical Electron-Transfer Theory. *Annu. Rev. Phys. Chem.* **1964,** *15*, 155-196.

27. Closs, G. L.; Miller, J. R. Intramolecular long-distance electron transfer in organic molecules. *Science* **1988,** *240*, 440-447.

28. Kavarnos, G. J. Fundamental of photoinduced electron transfer; VCH Publishers, 1993

29. Gust, D.; Moore, T. A.; Moore, A. L. Molecular mimicry of photosynthetic energy and electron transfer. *Acc. Chem. Res.* **1993,** *26*, 198-205.

30. Ward, M. D. Photo-induced electron and energy transfer in non-covalently bonded supramolecular assemblies. *Chem. Soc. Rev.* **1997,** *26*, 365-375.

31. Liu, J. Y.; El-Khouly, M. E.; Fukuzumi, S.; Ng, D. K. Mimicking photosynthetic antenna-reaction-center complexes with a (boron dipyrromethene)3-porphyrin-C60 pentad. *Chemistry* **2011,** *17*, 1605-1613.

32. Fukuzumi, S.; Saito, K.; Ohkubo, K.; Khoury, T.; Kashiwagi, Y.; Absalom, M. A.; Gadde, S.; D'Souza, F.; Araki, Y.; Ito, O.; Crossley, M. J. Multiple photosynthetic reaction centres composed of supramolecular assemblies of zinc porphyrin dendrimers with a fullerene acceptor. *Chem. Comm.* **2011,** *47*, 7980-2.

33. D'Souza, F.; Smith, P. M.; Zandler, M. E.; McCarty, A. L.; Itou, M.; Araki, Y.; Ito, O. Energy transfer followed by electron transfer in a supramolecular triad composed of boron dipyrrin, zinc porphyrin, and fullerene: a model for the photosynthetic antenna-reaction center complex. *J. Am. Chem. Soc.* **2004,** *126*, 7898-7907.

34. Kaschak, D. M.; Lean, J. T.; Waraksa, C. C.; Saupe, G. B.; Usami, H.; Mallouk, T. E. Photoinduced Energy and Electron Transfer Reactions in Lamellar Polyanion/Polycation Thin Films: Toward an Inorganic "Leaf". *J Am. Chem. Soc.* **1999,** *121*, 3435-3445.

35. Takagi, S.; Shimada, T.; Ishida, Y.; Fujimura, T.; Masui, D.; Tachibana, H.; Eguchi, M.; Inoue, H. Size-matching effect on inorganic nanosheets: control of distance, alignment, and orientation of molecular adsorption as a bottom-up methodology for nanomaterials. *Langmuir* **2013,** *29*, 2108-19.

36. Ishida, Y.; Shimada, T.; Masui, D.; Tachibana, H.; Inoue, H.; Takagi, S. Efficient excited energy transfer reaction in clay/porphyrin complex toward an artificial light-harvesting system. *J. Am. Chem. Soc.* **2011,** *133*, 14280-14286.

37. Takagi, S.; Shimada, T.; Eguchi, M.; Yui, T.; Yoshida, H.; Tryk, D. A.; Inoue, H. High-density adsorption of cationic porphyrins on clay layer surfaces without aggregation: The size-matching effect. *Langmuir* **2002,** *18*, 2265-2272.

38. Egawa, T.; Watanabe, H.; Fujimura, T.; Ishida, Y.; Yamato, M.; Masui, D.; Shimada, T.; Tachibana, H.; Yoshida, H.; Inoue, H.; Takagi, S. Novel methodology to control the adsorption structure of cationic porphyrins on the clay surface using the "size-matching rule". *Langmuir* **2011,** *27*, 10722-10729.

39. Takagi, S.; Aratake, Y.; Konno, S.; Masui, D.; Shimada, T.; Tachibana, H.; Inoue, H. Effects of porphyrin structure on the complex formation behavior with clay. *Microporous Mesoporous Mater.* **2011,** *141*, 38-42.

40. Kulasekharan, R.; Ramamurthy, V. New water-soluble organic capsules are effective in controlling excited-state processes of guest molecules. *Org. Lett.* **2011,** *13*, 5092-5.

41. Ishida, Y.; Kulasekharan, R.; Shimada, T.; Takagi, S.; Ramamurthy, V. Efficient singlet-singlet energy transfer in a novel host-guest assembly composed of an

organic cavitand, aromatic molecules, and a clay nanosheet. *Langmuir* **2013,** *29*, 1748-1753.

42. Ishida, Y.; Kulasekharan, R.; Shimada, T.; Ramamurthy, V.; Takagi, S. Supramolecular-Surface Photochemistry: Supramolecular Assembly Organized on a Clay Surface Facilitates Energy Transfer between an Encapsulated Donor and a Free Acceptor. *J. Phys. Chem. C* **2014,** *118*, 10198-10203.

43. Ramasamy, E.; Deshapriya, I. K.; Kulasekharan, R.; Kumar, C. V.; Ramamurthy, V. Photophysical studies of an encapsulated neutral guest intercalated into the 2-dimensional space of alpha-Zr(IV) phosphate. *Photochemical & photobiological sciences : Official Journal of the European Photochemistry Association and the European Society for Photobiology* **2014,** *13*, 301-309.

44. Konno, S.; Fujimura, T.; Otani, Y.; Shimada, T.; Inoue, H.; Takagi, S. Microstructures of the Porphyrin/Viologen Monolayer on the Clay Surface: Segregation or Integration? *J. Phys. Chem. C* **2014,** *118*, 20504-20510.

45. Ishida, Y.; Shimada, T.; Tachibana, H.; Inoue, H.; Takagi, S. Regulation of the collisional self-quenching of fluorescence in clay/porphyrin complex by strong host-guest interaction. *J. Phys. Chem. A* **2012,** *116*, 12065-12072.

Summary

Author examined the construction of the novel nano-structure materials composed of the inorganic layered materials, and the functionalities of the materials were examined in this thesis. The summaries of each part was follows.

(i) Construction of the gold nano particles assembly on the clay surfaces

In this section, author demonstrated the construction of assembly of gold nano particles which have unique behaviors as inorganic nano particles on clay surfaces. We succeeded to generate uniformly dispersed small gold NPs without aggregation on the clay surface by the use of stopped flow mixer in mixing process, although gold NPs prepared by the typical mixing method using magnetic stirrer were aggregated. The uniform formation of the particle was confirmed by the analysis of TEM images. It should be noted that any protecting reagent was not used in the present system. In addition, smaller gold nano particles were deposited on montmorillonite surfaces modified with porphyrin molecules. The size of generated gold nano cluster was small and uniform without aggregation. The average size of gold nano particles on the modified MNT surfaces was 1.3 nm, and standard deviation of that was 0.4 nm. However it is impossible to construct the assembly of gold nano particles on montmorillonite surfaces with high density without aggregation. To achieve the objective gold NPs assembly, novel strategy, in which porphyrin assembly structure without aggregation on the clay surface was utilized as a template for generating gold

clusters, was examined. The uniformly gold clusters were deposited on the montmorillonite surfaces without aggregation, and average diameter of the gold cluster was 1.5 nm. In addition, the average inter-particle distance of the nearby gold NPs (center to center) was 2.3 nm. This inter-particle distance indicates that gold clusters generation would reflect the non-aggregated assembled structure of porphyrin molecules on the clay surface. We believe that this Photosensitized Template Reduction (PTR) method would be useful as a new method to deposit metal NPs on the supporting materials.

(ii) Construction of a accumulated structure of porphyrin/clay complex and the photo-functionality of the porphyrin molecules

The alternately accumulated structure composed of porphyrin monolayer and clay layer was constructed by the intercalation reaction, and transparent TMPyP/SSA hybrid thin film was obtained. The structure of the film was determined by XRD, polarized Vis-ATR spectroscopy. The fluorescence quantum yield of TMPyP/SSA hybrid films did not depend on the density of porphyrin, and significant fluorescence quenching was not observed at any density of porphyrin in the three dimensional system. The chromism depending on the relative humidity of this structure was investigated to demonstrate the photo-functionality of this film. The color of hybrid film composed of MgTMPyP and saponite clay was changed form pink to orange with increasing of relative humidity, then absorption maximum due to Soret band of intercalated

MgTMPyP was shifted from 514 nm to 501 nm respectively. In the case of deep colored film, the visual color changes of those films were clearly observed compared to diluted film. This chromism would depend on softly structural change of the intercalated MgTMPyP.

(iii) Construction of the three component dyes' assembly on clay surfaces and the photochemical reaction flow control utilizing the molecular container

We proposed novel strategy to demonstrated the energy transfer reaction and subsequent electron transfer reaction between three kind of the dyes assembled on the clay surfaces. The energy donor was capsulated in cationic cavitand to control the photochemical reaction flow by suppressing the side electron transfer between Energy donor and electron acceptor. The average energy transfer efficiency in this sequential reaction system is 71%, and maximum efficiency of subsequent electron transfer reaction is 81%. Furthermore, side electron transfer reaction between energy donor and electron acceptor was suppressed, and average of energy loss was under 5%. We believe that this novel three components system assembled on the clay surface will allow us to make progress toward realization of biomimicking system for an artificial photosynthetic system.

Author believes that the possibility of the structural control with clay mineral would be expanded threw the works summarized in this thesis.

Acknowledgemnt

The author would like to express his sincerest appreciation to Professor Shinsuke Takagi, Department of Applied Chemistry, Graduate Course of Urban Environmental Sciences, Tokyo Metropolitan University, for his kind guidance, helpful suggestions, and hearty encouragement through this work.

The author would like to express his sincerest gratitude Professor Haruo Inoue, Tokyo Metropolitan University, for his helpful advices and suggestions.

The author would like to thank Professor Masatake Haruta, Professor Tetsuya Shishido for their helpful comments and suggestions.

The author would like to thank Professor Vaidhyanathan Ramamurthy, University of Miami, for his invaluable advices and suggestions.

The author would like to thank Dr. Tetsuya Shimada, Tokyo Metropolitan University, for his advices and supports, especially for laser flash photolysis experiments.

The author would like to thank Professor Ryo Sasai, Shimane University, for his advices and supports, especially for Absolute PL quantum yields measurement.

The author would like to thank the members of the research group under the direction of Professor Shinsuke Takagi at Tokyo Metropolitan University, and Professor V. Ramamurthy at university of Miami, for their continuing collaborations and hearty supports during the course of this study.

The author would like to thank Dr. yohei Ishida for their helpful comments and suggestions.

Finally, the author is particularly grateful to his parents, Mr. Kazuhisa Fujimura and Mrs. Masayo Fujimura for their understanding and perpetual support.

February 24th, 2015

Takuya FUJIMURA